energies

MDPI

Review

Passive Small Direct Alcohol Fuel Cells for Low-Power Portable Applications: Assessment Based on Innovative Increments since 2018

Maria H. de Sá [1,2,*], Alexandra M. F. R. Pinto [2,3,*] and Vânia B. Oliveira [2,3,*]

[1] CIQUP—Chemistry Research Centre of the University of Porto, Department of Chemistry and Biochemistry, Faculty of Sciences, University of Porto, Rua do Campo Alegre, 4169-007 Porto, Portugal
[2] CEFT—Transport Phenomena Research Centre, Faculty of Engineering, University of Porto, Rua Dr. Roberto Frias, 4200-465 Porto, Portugal
[3] ALiCE—Associate Laboratory in Chemical Engineering, Faculty of Engineering, University of Porto, Rua Dr. Roberto Frias, 4200-465 Porto, Portugal
* Correspondence: mhsa@fe.up.pt (M.H.d.S.); apinto@fe.up.pt (A.M.F.R.P.); vaniaso@fe.up.pt (V.B.O.)

Abstract: Passive small direct alcohol fuel cells (PS-DAFCs) are compact, standalone devices capable of electrochemically converting the chemical energy in the fuel/alcohol into electricity, with low pollutant emissions and high energy density. Thus, PS-DAFCs are extremely attractive as sustainable/green off-grid low-power sources (milliwatts to watts), considered as alternatives to batteries for small/portable electric and electronic devices. PS-DAFCs benefit from long life operation and low cost, assuring an efficient and stable supply of inherent non-polluting electricity. This review aims to assess innovations on PS-DAFC technology, as well as discuss the challenges and R&D needs covered on practical examples reported in the scientific literature, since 2018. Hence, this compilation intends to be a guidance tool to researchers, in order to help PS-DAFCs overcome the barriers to a broad market introduction and consequently become prime renewable energy converters and autonomous micropower generators. Only by translating research discoveries into the scale-up and commercialization process of the technology can the best balance between the economic and technical issues such as efficiency, reliability, and durability be achieved. In turn, this will certainly play a crucial role in determining how PS-DAFCs can meet pressing sustainable energy needs.

Keywords: low-power; microgenerators; passive small direct alcohol fuel cells (PS-DAFCs); portable applications; recent R&D innovations; review analysis; sustainability

Citation: de Sá, M.H.; Pinto, A.M.F.R.; Oliveira, V.B. Passive Small Direct Alcohol Fuel Cells for Low-Power Portable Applications: Assessment Based on Innovative Increments since 2018. *Energies* **2022**, *15*, 3787. https://doi.org/10.3390/en15103787

Academic Editor: Vladimir Gurau

Received: 6 April 2022
Accepted: 19 May 2022
Published: 21 May 2022

1. Introduction

The urgent need for energy storage alternatives toward a fully sustainable decarbonized energy paradigm change is becoming increasingly clear [1–5]. Moreover, the energy requirements of innumerable portable electronic devices, as well as electrical appliances, presenting high power input due to increasing functionalities or small energetic but long consumption periods (even in remote places or off-grid), are rapidly increasing. These are aspects which have reactivated the interest in fuel cells of all types [6–11]. A comparison of fuel cells to alternate electrochemical technologies, such as capacitors and batteries, can be achieved by using the so called "Ragone plot", representing their power densities or specific power ($W \cdot kg^{-1}$) versus energy densities or specific energy ($W \cdot h \cdot kg^{-1}$). This representation puts in evidence that fuel cells can be considered high-energy devices, whereas supercapacitors and capacitors exhibit high power, while batteries have intermediate power and energy characteristics [12]. Note that supercapacitors, batteries, and fuel cells all consist of two electrodes in contact with an electrolyte solution. However, while electrochemical capacitors (or supercapacitors) store the energy within the electrochemical double layer at the electrode/electrolyte interface and not via redox reactions, the use of

the terms anode and cathode may not be appropriate. In fuel cells, similar to batteries, the electrical energy is generated by conversion of chemical energy via redox reactions at the two electrodes (cathode and anode) in contact with an electrolyte. However, in contrast to batteries, fuel cells are open systems that do not require recharging and are able to operate as long as fuel continues to be provided, thus making them an attractive alternative to batteries. Direct alcohol fuel cells (DAFCs) cause increased interest as environmentally friendly and efficient energy conversion devices, since they generate electric power directly from the electrooxidation of liquid fuels (alcohols), with water and carbon dioxide (CO_2) as the main products, along with heat. Thus, when derived from sustainable and renewable sources, these fuels can be considered an alternative to the standard sources of energy, such as fossil fuels, helping to achieve most pressing climate challenges, including carbon neutrality. Moreover, in comparison to traditional hydrogen-fed polymer electrolyte membrane fuel cells (PEMFCs), alcohols have a higher volumetric energy density, in addition to being easier to handle and store [13–19]. Thus, DAFCs are considered as alternative and green power sources. Among the different possible alcohols, methanol (CH_3OH or MeOH) is the simplest and the most used one. It is easily produced (from fossil fuels or biomass), stored, and handled, in addition to having a high energy density in comparison with hydrogen. Therefore, commercialization of direct methanol fuel cells (DMFCs) has encouraged R&D in companies and institutions to create better, simpler, and more economical prototypes, leading to some niche markets [11,14–16]. For other alcohols (ethanol, ethylene glycol, propanol, etc.) being used as fuel, the C–C bond cleavage is an extra factor to consider. Moreover, their oxidation to CO_2 involves more intermediates and pathways than that of methanol. Hence, more active catalysts are required, particularly at lower temperatures. Consequently, their commercial deployment has been hampered by the relatively complex and sluggish alcohol oxidation reaction (AOR) in acidic medium and the high cost of platinum (Pt)-based electrocatalysts traditionally used [16,18–21]. However, one should point out that direct ethanol fuel cells (DEFCs) are gaining attraction, as this fuel, compared to methanol, offers higher energy density and a low price, in addition to being less corrosive and nontoxic. Ethanol (C_2H_5OH or EtOH) can be obtained in large amounts through fermentation of agricultural renewable crops and waste, such as corn and sugarcane [22–27]. Some examples of DAFC portable commercial products based on different alcohol fuels are presented in Table 1.

Table 1. DAFC portable commercial applications. Reproduced from [18] with permission from Elsevier.

Field	Fuel	Products	Manufacturer	Characteristics
Laptop	Methanol	CD-ROM-sized fuel cell pack	Antig Technology	Electric power of 45 W for 8 h of normal laptop use
	Methanol	A laptop docking station	Samsung	Maximum output of 20 W
	Methanol	Battery charger	Panasonic	Provided between 10 W and 20 W of power with 200 mL of methanol
	Methanol	Fuel cell notebook PCs	Antig Technology & Toshiba	Produced power of 10 W and voltage of 7.2 V
Military/industrial	Methanol	Off-grid power generators	SFC Energy	Power output of 500 W
	Methanol	Army field power pack	SFC Energy	Power output of 250 W for the larger unit at 12 or 24 V and 100 W at 28 V for the smaller one
	Methanol	Portable generators, chargers, and batteries	SFC Energy	Capacity of 50 W

Table 1. *Cont.*

Field	Fuel	Products	Manufacturer	Characteristics
Medical	Methanol	Hearing aid	Danish Technological Institute (DTI)/WIDEX®	Supply 2.5 mW continuously for 24 h at a voltage above 350 mV with less than 200 µL of methanol
Telecommunication	Methanol	Battery charger	Antig Technology	Power output 3 W and voltage of 5.5 V
	Methanol	Dynario™ (Battery charger)	Toshiba	Power output of 2 W with a single injection of 14 mL of concentrated methanol solution
	Methanol	Mobile and remote power source	Neah Power System	Power density level exceeding 80 mW/cm^2
Others	Ethanol	Power pack	NDC Power	Power output of 3–250 W and operational time 3700 h
	Methanol	Bio-energy discovery kit	Horizon Fuel Cell Technology	Generated power of 10 mW
	Methanol	Mobile audio player	Toshiba and Hitachi	Capacity of 100 mW for 35 h player usage with single 3.5 mL or 300 mW for 60 h with single 10 mL of concentrated methanol solution

The technology fundamentals of a DAFC device can be roughly divided into its core components: the membrane electrode assembly (MEA) and the general system/cell structuring and packaging (e.g., the current collectors (CCs) and the end plates). Figure 1 presents an exploded-view schematic of the DAFC main components.

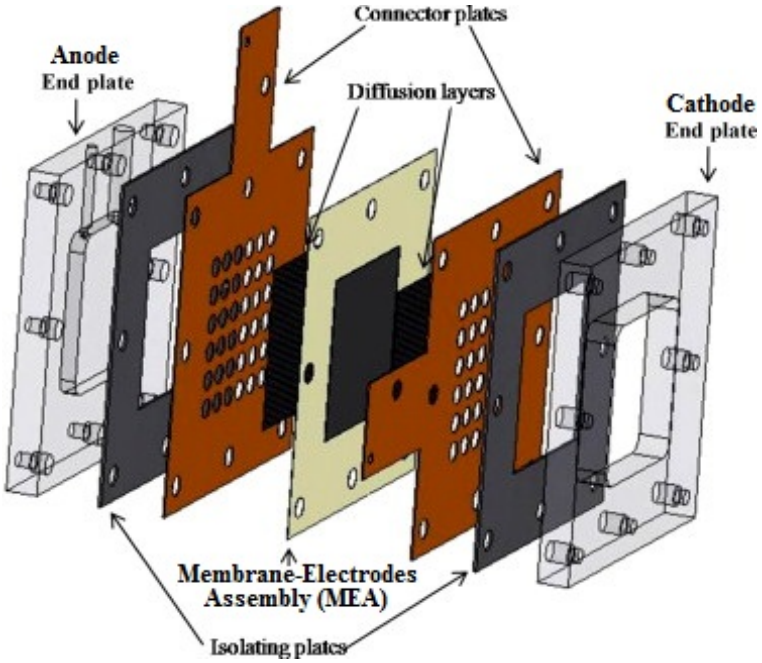

Figure 1. DAFC main components: exploded-view schematic.

In order to better understand the examples presented, it is important to detail the traditional structure of a DAFC, accompanied by the most used acronyms. The MEA is constituted by a polymer electrolyte membrane or proton exchange membrane (PEM) sandwiched between the electrodes, in which catalyst layers promote the oxidation and reduction reactions to generate electricity at the anode and cathode, respectively. Hence, sequential parts of an MEA can be identified as the anode diffusion layer (ADL), anode

catalyst layer (ACL), PEM, cathode catalyst layer (CCL), and cathode diffusion layer (CDL). Both electrodes are supported on macroporous carbon paper or cloth called the "diffusion layer", often named the "gas diffusion layer" (GDL) and sometimes smoothed out by a thin microporous layer (MPL), made of carbon black (CB) and polytetrafluoroethylene (PTFE). The GDLs provide the transport channels for the reactants (fuel and oxidant) and reaction products. The PEM most commonly used in DAFCs is Nafion®, a perfluorinated sulfonic acid ion-exchange membrane, developed by DuPont (Wilmington, DE, USA). This polymer/proton conductive membrane, in addition to being the electrolyte, serves as the barrier between the two electrodes and a barrier to fuel crossover/permeation, as further detailed later. The electrons released in the AOR at the anode are not conducted by the membrane, but by the anode CC and returned to the cathode by the cathode CC, via an external electric circuit. On the cathode side, the oxygen reduction reaction (ORR) occurs in air, promoted by the CCL, to form water. In this manner, the redox pair (AOR and ORR) provides the path to directly, in an efficient and clean way, convert the fuel's chemical energy into electrical energy, and these power generator devices can be used in the different applications (as presented in Table 1) [16,18–20,28,29].

The performance of these devices can be characterized by their open-circuit voltage (OCV) or voltage at which no load is applied, peak/maximum power density (PD) obtained from polarization (current–voltage) curves, and operating temperature (T) [7,30]. Despite the clear advantages in terms of kinetics when operating at higher temperatures, this requirement is not suitable for the PEM structural stability. Hence, these devices are considered to belong to the "low-temperature" category (typically bellow 95 °C) [7,16]. Their low operation temperature allows an uncomplicated start-up, in addition to being a quick and easy response to changes in load and/or operating conditions, even at room temperature. In practical applications, a series of connected single cells, named a "fuel cell stack" (or simply "stack"), are used instead of a single cell. Partitioning the adjoining cells stacked on one another and serving as the transmitter/connector of an electric current to the outside, like the CCs of the single cell, there are conductive separators called bipolar plates (BPs). Thus, the CCs or BPs are also key components in these devices, since they account for about 80% of the total weight of the cell and are essential to ensure the uniform compression of the MEA and a minimum contact resistance. They connect electrically and supply reactants/remove reaction products through different flow field/channel designs, to/from both electrodes. Depending on how the fuel and oxidant are supplied, DAFCs can be categorized into two major operation modes: active or passive (Figure 2) [16].

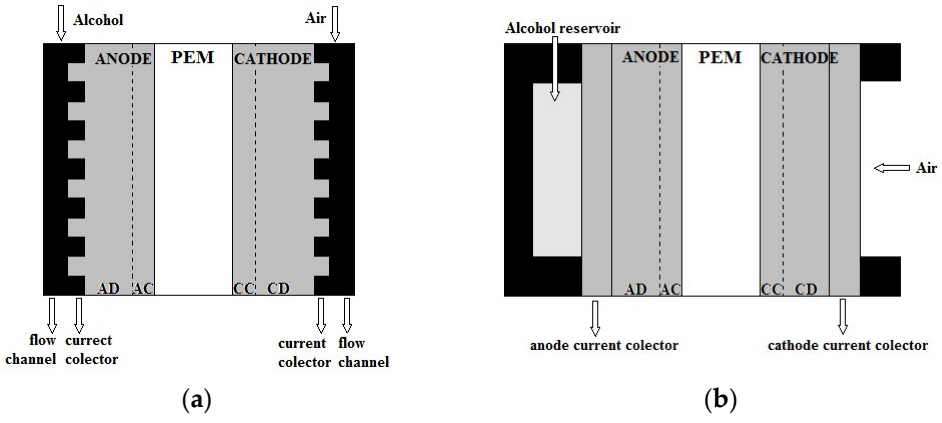

Figure 2. General main operating modes of DAFCs: (**a**) active and (**b**) passive. Reproduced from [16] with permission from 2018 Elsevier.

For small/portable power applications there is a strong need to minimize the size of the components [31]. Therefore, passive DAFCs seem more suitable with an attractive cost-to-power ratio compared to active DAFCs. The passive feeding system does not require auxiliary supplying devices; thus, a fuel pump along with an air blower is not present. The

flow of reactants and products is based on diffusion, as well as natural convection. Hence, the fuel is provided to the ADL and ACL from a reservoir/tank build in the anode end plate, whereas the oxygen to the CDL and CCL comes from the surrounding air through the open cathode end plate (often called "air-breathing" mode). In this way, no additional power consumption is needed, and the parasitic power phenomenon due to the external components is minimized. Thus, a significant system volume reduction is achieved [16]. Moreover, with the rapid development of micromachining technologies, miniature (milli- or micrometer scale) passive DAFCs (PS-DAFCs) represent a promising application as micro-energy power sources aimed at a niche market. These can be used as substitute for batteries in small portable devices, such as mobile phones (0.1–3 W) or laptops (5–50 W) and digital cameras (5–20 W), as well as other cordless systems (3–50 W), including next-generation portable consumer electronics, such as wearable electronics and medical devices, very sensitive to the weight and volume of micropower sources [32–34]. Nevertheless, with the decrease in size, an evident effect on internal gas–liquid two-phase transport appears. The absence of an external flowing force to remove CO_2 bubbles and water droplets leads to their internal accumulation, as they are constantly produced by the anode and cathode reactions. Thus, this hinders further reactions by blockage of mass transfer and the electrode surface. Moreover, PS-DAFCs can also suffer from fuel crossover from anode to cathode, since the Nafion® membrane is not completely impermeable to alcohol molecules. This is particularly significant when the cell is operated with high concentrations of small alcohols, so-called "methanol crossover" (MCO). This process can decrease the cell performance, due to cathode poisoning and fuel wasting during device operation. In turn, low alcohol concentrations could lead to an inadequate fuel supply, reducing the cell performance and rendering the power output of the passive DAFC unacceptable for real applications. However, this raises another important issue affecting the performance and integrity of these devices, i.e., the water management during operation. The water flux through the Nafion® membrane is due to the coupled effect of diffusion and electroosmotic drag. In a proper balanced operation, the water present on the cathode side (caused by accumulation from both water diffusion through the membrane and water generated in the cathode side) should be removed to prevent severe flooding of the electrode and increased resistance of oxygen transfer. On the anode side, water should be provided to compensate for the water crossover through the membrane. All these factors are substantially critical for PS-DAFCs, compared with their active counterparts, mostly caused by the use of a low concentration fuel and a decline in the cathode catalytic activity.

In summary, one can point out as the major setback of PS-DAFC commercialization the lack of low-cost materials (electrocatalysts, electrodes, and electrolyte/membrane) providing stable and satisfactory performance [15,16,18]. Up to now, the most effective catalysts in PS-DAFCs have been precious metal group (PMG)-based nanoparticles (NPs) including Pt, Ru, Pd, and Au, supported on high-surface-area carbon. Pt-based alloys such as PtRu show high tolerance to the poisoning effect of intermediary CO, providing stability and improved kinetics toward the AOR, particularly for methanol. Even so, the high loadings of PMG NPs required for reasonable power output of PS-DAFCs raise the costs and impact of the technology. This aspect, together with the catalyst durability (improving the performance of the catalysts and its supports), is driving recent research in the field [18,35–41]. For fuel cells in general, two material-based strategies have been tackled. One is to decrease PGM (platinum group metal) usage by increasing its activity (so-called "low-PGM catalysts") [42–47], while the other one is to develop alternative PGM-free catalysts to completely replace PGM with Earth-abundant materials [48–56]. Thanks to the significant efforts in recent years on alternative catalysts for active DMFC systems in acidic medium, PGM-free catalysts, such as Fe–N–C catalysts (commercially available from Pajarito Powder manufacturing company), have demonstrated an improved ORR activity and methanol-tolerant behavior, when used as a cathode electrode, with reasonable power outputs [57–61]. Overall, these results demonstrated the promising prospect for

high-performance and inexpensive DAFCs using PGM-free or low-PGM-based catalysts for ORR and AOR, with tuned selectivity and tolerance to a range of fuels and chemicals [62].

Even so, for this kind of catalyst, the acidic environment of conventional PEM-DAFCs still imposes stability challenges, mainly due to Fe dissolution and carbon corrosion under operational conditions, involving mechanisms such as dissolution, agglomeration, and/or detachment of the carbon support from the catalytic NPs [63]. The use of solid anion-exchange membranes (AEMs) as an alternative electrolyte has led to increasing interest in alkaline DAFCs (AEM-DAFCs), since non-precious metal catalysts can be employed to overcome problems associated with PEM-DAFCs [64–66]. AEMs usually contain a main polymer backbone covalently bound to cationic functionalities (such as simple quaternary ammonium groups or other more complex and stable groups) that confer anion selectivity. The most common anion species transported in AEMFCs is represented by hydroxyl ions (OH^-) produced by ORR at the cathode, and the MEAs can be fabricated using commercial AEMs such as Tokuyama A201 (Tokuyama Corporation, Tokyo, Japan) and Fumasep® FAA-3 (FUMATECH BWT GmbH, Bietigheim-Bissingen, Germany). However, despite a flurry of recent research activity and the improved performance of AEMFCs, their durability is still lower than that of PEMFCs [67–75]. Thus, further advances in AEM-DAFCs are also conditional on improving the performance of electrocatalysts along with AEM stability and durability, required to achieve highly effective devices [73–81]. As a final remark, the devices (PEM-DAFC or AEM-DAFC) generally require oxygen as the electron acceptor (oxidant), typically from the ambient air in the passive mode. Nonetheless, their application in air-free environments such as outer space and underwater requires an additional oxygen tank in the system, lowering the energy density of the whole fuel cell system. An alternative approach, which has received increasing attention, is to use the hydrogen peroxide (H_2O_2) reduction reaction (HPRR) instead of ORR, primarily because this is a simpler and easier (two-electron transfer) process, leading to a low activation loss and the possibility of using non-Pt catalysts. In addition to improving the cell performance, since the theoretical voltage of the fuel cell is substantially increased, water flooding problems are avoided due to its intrinsically liquid nature. All these aspects were addressed in the pioneering research published by Yan et al. [82], who demonstrated the concept for an acid DMFC (run in active mode with their synthesized Prussian Blue (PB)/carbon nanotubes (CNTs) catalyst for the HPRR, considered inexpensive), as well as in a previous paper [83] on an alkaline DEFC, also in active mode with non-Pt catalysts. More recent examples regarding PS-DAFCs are presented in Section 3; however, for those particularly interested in fuel cell-based power systems for unmanned aerial vehicles (UAVs), some advances and challenges can be found in [84].

In summary, previous research has laid the foundation for the fundamental knowledge regarding how the structural design and operating conditions influence the performance of the different types of DAFCs. However, significant market penetration of these devices has not yet been achieved. The fuel cell industry must face the challenge of how to overcome techno-economic barriers toward competing technologies, in order to achieve end-user acceptance and a competitive advantage for commercialization. These aspects in turn are interdependent on the reliability and durability of the devices (low durability leads to fuel cell repair, an increase in maintenance costs, and a decrease in reliability) [85,86]. Moreover, in order to evaluate the feasibility of concrete DMFC applications, a recent cost analysis study of DMFC stacks for mass production pointed out that the introduction of innovative approaches can result in further cost savings [87]. Hence, research is in progress to overcome all these difficulties and achieve optimized (stable and durable) cost-effective fuel cells. In this review, we summarize the recent progress and highlight R&D innovations in PS-DAFC technology over recent years, which will certainly play a crucial role in determining how PS-DAFCs can meet the energy needs of small portable power applications.

2. DMFCs: Single Cells (Acidic or Alkaline) and Stacks

Particular emphasis is given to DAFCs that use methanol as fuel (DMFC), because DMFCs have been the most studied DAFC. This and other aspects regarding DMFC device technology were discussed and critically analyzed in the recent book by Dutta released in 2020 [88]. In this publication, it is possible to find full chapters devoted to passive DMFCs and DMFCs for portable applications, focused on the transition from lab to commercial scale, among other critical technological aspects of DMFCs. We highlight also the holistic picture of the key component design of DMFCs provided by Xia et al. [19], as this paper gathered the strategies addressing the DMFC technology and presented the most recent advances in material and structural designs, with an emphasis on the catalyst, membrane, electrode architecture, and flow fields considering multiscale applications. Another comprehensive and critical review focusing on the recent findings for different materials related to anode catalysts (comprising PGM or PGM-free MOR electrocatalysts) was presented by Yuda et al. [89]. This paper reviewed the effects of manipulating the catalyst, structure of the support materials, electrolyte conditions (pH dependence), and synthesis method. Additionally, the challenges in developing commercial micro-DMFCs were also discussed. In fact, benefiting from a high energy density and low operating temperature, DMFCs have been rated as the most likely portable energy device to replace traditional lithium batteries. Their theoretical energy density is 15 times greater than that of a lithium-ion battery, and their replenishment is easily and quickly achieved, by replacing or refilling the fuel cartridge within seconds [90]. Thus, micro-DMFCs have been extensively used in academia and industry, owing to their ability to provide power in different engineering applications [91]. Herein, we provide a compact review of practical examples and recent developments of PS-DMFCs (passive small direct methanol fuel cells) (as single cells or stacks), as well as the challenges reported in the field, from 2018 onward.

2.1. Acidic DMFCs

In view of the possible use of PS-DMFCs as a replacement for batteries, we start by presenting a novel button-type PS-DMFC reported by Zhu et al. [92]. This design combines the layout of the traditional block-type DMFC and that of the conventional button-type battery (Figure 3). In this way, the researchers were able to eliminate bolts in the packaging structure, which was considered a major drawback for the miniaturization process, since bolts cover a large area, thus reducing the specific energy (energy per unit weight), as well as power density (power per unit area), of the device. Thus, the novel button-type PS-DMFC allowed improving the effective area ratio of the cell, which was 1.77 cm^2.

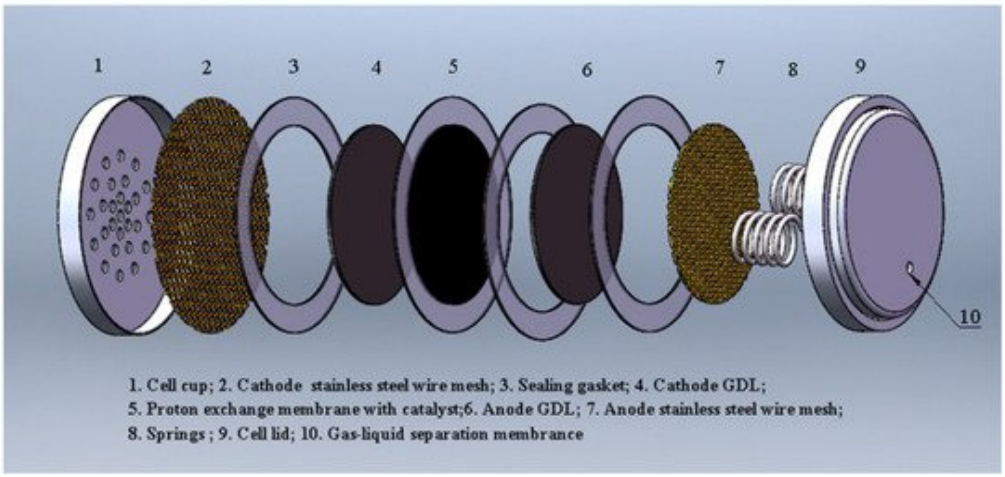

Figure 3. Schematic of a novel button-type PS-DMFC. Reproduced from [92].

Furthermore, in order to guarantee GDLs with an optimal porosity, following their previous studies [93] and after testing several different configurations, the researchers

used carbon paper (CP) and three-dimensional graphene (3DG) as the cathode and anode GDL, respectively. Additionally, to ensure good internal electric contact, a titanium-plated stainless-steel (SS) wire mesh was positioned between the GDL and the end plate on both electrodes, with SS springs as CCs. The end plates of the button-type PS-DMFC were the lid and cup of standard lithium battery as assembled in a packaging machine for lithium-ion button batteries. After packaging, the best performance reached a volumetric power of 11.85 $mW \cdot cm^{-3}$ (or maximum power density of 4.78 $mW \cdot cm^{-2}$), when using 1 M methanol solution in ambient conditions.

A self-constructed traditional single small DMFC (MEA with an active area of 4.0 cm^2) was used to investigate the influence of the different modes of operation on the DMFC performance [94]. In the active mode, the authors varied the methanol concentration (2 to 8 M) and the flow rate (1 to 4 $mL \cdot min^{-1}$), while air or high-purity oxygen was supplied in both modes. The results showed that incrementing the methanol concentration and flow rate, until certain values, improved the DMFC performance. Moreover, for all the parameters tested, the active mode feed with oxygen yielded the highest power density (10.41 $mW \cdot cm^{-2}$), followed by the active mode with air (8.39 $mW \cdot cm^{-2}$) and the passive DMFC system (5.93 $mW \cdot cm^{-2}$). However, one should keep in mind that, in real applications, an active system has higher requirements in terms of cost and space, which can be detrimental or even impossible for small and portable applications. As aforementioned, a passive system relies only on natural forces to work; however, this leads to mass transport limitations adding to the already sluggish electrode kinetics. Due to all of these issues, the cell performance in passive mode can be negatively impacted. Regarding the water management issue, previous studies have shown that one method to circumvent this problem is to facilitate water withdrawal and oxygen transfer using suitable flow field patterns or similar structures. Hence, Yuan et al. [95] proposed the use of a simple self-made expanded metal mesh as the cathode flow field in a DMFC, made without any pretreatment or additional component. Although the metal was not explicitly identified by the authors, they made reference to their previous published studies regarding the effects of the SS expanded mesh used as a flow field in a passive DMFC [96]. Stability tests were performed in a transparent prototype PS-DMFC (end plates made of polymethylmethacrylate (PMMA) with an MEA active area of 3×3 cm^2, at a constant discharging current density of 40 $mA \cdot cm^{-2}$ (condition of higher performance) for 120 min. In this way, the researchers compared the ability of water removal with expanded metal meshes and traditional perforated flow fields, including the circular hole array (CH) and parallel fence (PF) patterns, with open ratios of 38.5% and 65.3%, respectively. During their experiments, a similar expanded mesh was used as the anode flow field, along with a methanol concentration of 8 M. The results showed a similar decrease in cell voltage in the first 8 min, justified by the fact that the GDL (carbon paper) was gradually blocked by water bubbles, which grew into larger slugs before detachment to the flow channels. However, when the expanded mesh was used, the water accumulation occurred only at the bottom and covered very few openings. Consequently, the cell voltage was relative stable and decreased by about 23 mV (11.3%) within 120 min. On the other hand, in the case of the PF pattern within the same time, the cell voltage decreased by around 55 mV (32.6%), whereas, for the CH pattern, the voltage decreased to zero within 72 min. Thus, this study verified that water flooding/accumulation could be attenuated with the use of the expanded mesh as the flow field, which is of great importance for improving PS-DMFC performance. An alternative approach to enhance water management and fuel efficiency was also reported by the same research group, taking advantage of both the super-hydrophilic and the super-hydrophobic properties of flow field patterns [97]. Thus, the flow field layer was manufactured "in-house" from copper fiber sintered felt (CFSF) with tunable wettability, through a solution-immersion method previously reported [98]. This porous material exhibits good stability and conductivity; moreover, due to its three-dimensional network structure and interconnected pores resulting from the fiber sintering process, it can be used to optimize the mass transport on the cathode side of PS-DMFCs. The results obtained

showed that the super-hydrophilic flow field was better at low methanol concentrations (the optimal methanol concentration was 2 M, and the optimal porosity was 60%), having excellent water removal ability but poor ability to control MCO. At higher concentrations, the super-hydrophobic cathode flow field enhanced the cell performance, by promoting the water backflow and preventing MCO. The best performance (with a maximum PD of 18.4 $mW \cdot cm^{-2}$) was achieved with a 4 M methanol concentration and a flow field porosity of 60%. Moreover, even at a higher methanol concentration (6 M), this cathode flow field performed reasonably, since it was able to control the MCO. In order to reduce the MCO effect and promote the cell performance, the same research group reported the application of another "in-house" prepared porous material in the PS-DMFC, i.e., carbon nanofiber webs (CNWs), which were located between the MEA and the anode CC. These fibers were prepared from polyacrylonitrile (PAN) via electrospinning and heat treatment [99]. It was expected that, due to their porous structure, the CNWs acted as a methanol barrier by increasing mass transfer resistance. Moreover, the hydrophilicity of CNWs could also promote water transport and inhibit methanol transfer. The researchers also investigated the effect of PAN concentration and carbonization temperature on the material properties, particularly its microstructure, and they verified that a higher concentration led to a larger nanofiber diameter and lower porosity, whereas a higher temperature for carbonization helped to enhance the conductivity of the final material. Hence, they demonstrated that the use of CNWs served as a methanol barrier, reducing the MCO and increasing the cell performance, especially at lower methanol concentrations. Therefore, the researchers observed an increase in PD up to 53.54% when the CNWs were employed, in contrast with the conventional PS-DMFC fed with a 2 M methanol solution. However, at higher methanol concentrations, the positive effect of the CNWs declined. This effect was explained by an increase in difficulty of CO_2 removal, caused by the CNW barrier effect.

Regarding the CO_2 removal issue, a novel structure allowing its release to the surroundings directly from the ADL of PS-DMFCs, through a super-hydrophobic lateral venting design, was proposed by Li et al. [100]. In this design (Figure 4), the interior surface of the anode end plate, with six lateral venting micro channels (0.2 mm depth × 0.2 mm width), was coated with a super-hydrophobic fluoropolymer [101]. Using this novel cell configuration, the researchers also implemented a conventional anode end plate (without lateral venting channels) to be used as a reference. Moreover, for both designs, to evaluate the effect of the lateral venting design on gas removal, the researchers also fabricated models were the inlet/outlet holes and other seams were carefully sealed (totally enclosed). In addition, as the SS anode CC was replaced by a porous carbon plate to avoid MCO during high-concentration operation, they named it "cell-CP".

By testing the three types of PS-DMFCs (totally enclosed, opened, and high-concentration cells), with and without lateral venting, the researchers demonstrated that the novel structure could considerably prevent the formation of a CO_2 barrier. Additionally, they showed that, with the lateral venting configuration, the performance of the totally enclosed PS-DMFC was slightly lower than that of the opened one. The authors justified these findings by the fact that, when the pressure was high, the MCO reduced the output voltage dramatically. Thus, even for higher methanol concentrations (14 M) a more stable output voltage was achieved on discharging tests, performed with the cell-CP, when compared with the totally enclosed PS-DMFC. The same research group reported a study regarding a new cathode water backflow structure to prevent the issue of water accumulation/flooding [102]. In a conventional cathode, a high loading of PTFE on the MPL is normally used to remove water. This, however, hinders oxygen transport and increases ohmic resistance. Therefore, the researchers designed a novel CDL by doping graphene oxide (GO) using a stainless-steel fiber felt (SSFF) as the base material. The resulting composite material was then reduced at high temperatures and subject to hydrophobic treatment on the exterior of the cathode, by brushing 5% and 10% PTFE solutions. This composite was used as both the cathode CC and the cathode support layer for the catalyst. Hence, due to its hydrophobic properties, the water backflow effect at the cathode was achieved, preventing the obstruction of the air

inlet channels by water droplets and enhancing the oxygen transfer efficiency. In addition, the reduced GO (rGO) facilitated charge transport without increasing the electrode contact resistance. As a reference, a conventional cell with carbon paper as the CDL was also assembled and used. Comparing the performance of the fuel cells (both with an active area of 1.2 × 1.2 cm^2), the researchers verified that the best results were obtained using the 10% PTFE-treated film (see Table 2). To investigate the long-term operation stability, the new cell was discharged under a constant current density of 80 $mA \cdot cm^{-2}$ at 25 °C for 160 min, which was 33.3% longer than the conventional one due to an accumulation of water droplets on the cathode surface of the conventional cell. This topic was further explored in another publication [103], which reported the use of three-dimensional graphene frameworks (3D GFs) on the cathode MPL of DMFCs, due to the unique microstructure and hydrophobic characteristics of the 3D GF. This novel cathode MPL design not only held smaller, more uniform pores compared to its traditional counterpart, but was also free of mud cracks. This greatly increased the capillary pressure for water backflow in the CCL, which led to improved oxygen transfer and reduced MCO. To illustrate how the performance of a typical PS-DMFC (1 cm^2 active area) varied with the cathode MPL structure, the researchers used different CB, 3D GF, and PTFE mass ratios during the fabrication process.

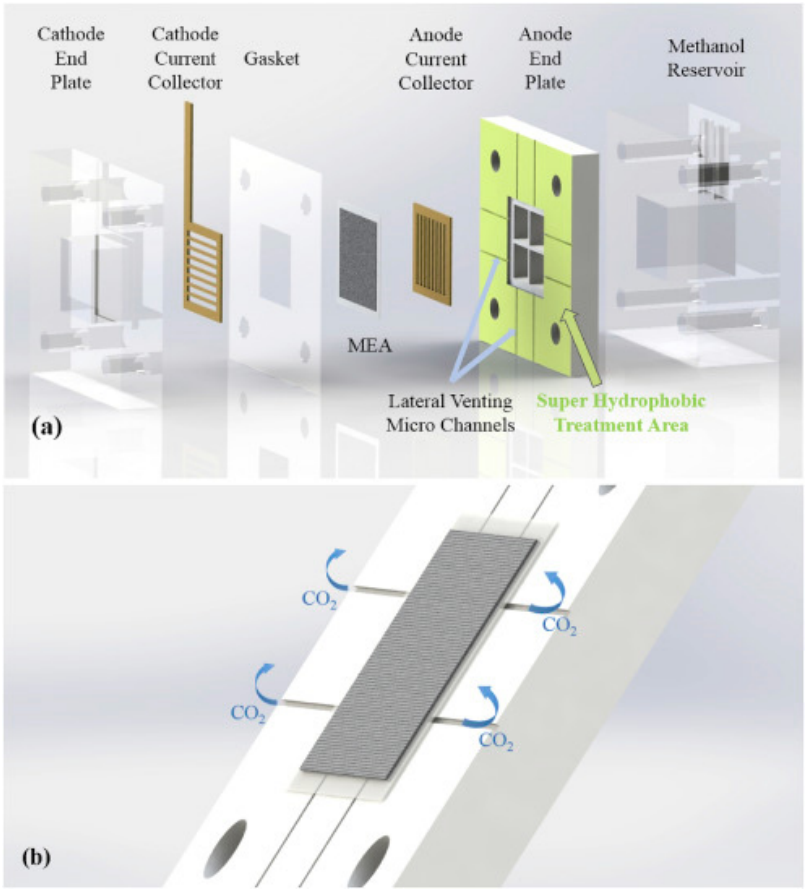

Figure 4. (**a**) Schematic configuration of PS-DMFCs with a super-hydrophobic lateral venting design of micro channels, and (**b**) detailed view of the six lateral venting micro channels. Reproduced from [100] with permission from Elsevier 2018.

Further studies regarding the cathode side were also pursued by Deng et al. [104], who reported the design and fabrication of a novel cathodic trilaminar catalytic layered MEA structure (1.15 × 1.15 cm^2 active area), made of three porous layers, with the central/middle layer presenting lower porosity than the inner and outer ones. This new configuration created a water pressure gradient, which enhanced the water backflow and the oxygen transport, by reducing MCO and cathode flooding. These findings were

confirmed by simulation results from a three-dimensional static study, carried out in a two-phase thermal model for a PS-DMFC supported by the finite element method, employing COMSOL Multiphysics® software. The researchers prepared three different cathodes with the same catalyst loading but different structure/porosity, using a pore-former (PFr) component—NH_4HCO_3. In the absence (conventional formulation) or presence of the PFr agent, the cathode was named "No PFr" or "Full PFr", respectively. The trilaminar catalytic layered cathode structure was achieved using a mix of both, called the "Partial PFr" cathode. These different cathodes were assembled in MEAs tested in a PS-DMFC, where the cathode CC had hole openings (open ratio of 37%), while the anode CC had parallel channels (open ratio of 50%), as shown in Figure 5. The performance evaluation of the cells with different cathodes, operating with 2 and 4 M methanol solutions at 25 °C, showed that the Partial PFr cathode achieved the best results, in contrast to No PFr, while the Full PFr cathode performed intermediately for both concentrations. However, for the higher methanol concentration, the PD decreased in all cases, which the researchers assumed to be due to the methanol permeability critical effect. However, for the PS-DMFC with the Partial PFr cathode (trilaminar catalytic layered), the water backflow effect reduced the MCO and cathode flooding, increasing the cell potential. In addition, with the stability tests performed for 120 min under 80 $mA \cdot cm^{-2}$ when discharging 2 M methanol at 25 °C, the researchers also observed that the Partial PF cathode structure was more stable compared with the No PFr cathode. These findings clearly point out that this structure may be a viable option to improve the performance and stability of PS-DMFCs.

(**a**) (**b**)

Figure 5. Pictures of the PS-DMFC assembled with trilaminar catalytic layered from (**a**) the cathode and (**b**) the anode side. Reproduced from [104].

With that goal in mind and to reduce the cell cost (by reducing the catalyst loadings, as shown in Table 2) and weight, Braz et al. [105] reported the use of different materials in the anode and cathode CCs of a PS-DMFC. The cell had and active area 25 cm^2 and two acrylic end plates, one with an open window of 25 cm^2 (cathode side) and the other with a fuel reservoir of 12.5 cm^3 (anode side). The CCs featuring flow fields with a circular-hole array pattern (open ratio of 34%) were made from 316 SS, Au-plated (1 µm thickness coating) 316 SS (SS + Au), and titanium (Ti). The cell performance was evaluated through polarization and stability tests, using electrochemical impedance spectroscopy (EIS) measurements and an innovative equivalent electric circuit (EEC) to accurately describe the PS-DMFC. Regarding the different CC materials tested, the best performance was achieved using SS and Ti as the cathode and anode CC, respectively. The maximum PD of 5.23 $mW \cdot cm^{-2}$ was achieved using a 7 M methanol concentration. Moreover, the stability tests revealed a loss of efficiency of 41% for a lifetime of 200 h, which they assigned to the degradation of the membrane and corrosion of the cathode CC (higher ohmic resistance), as well as degradation of the anode and cathode catalysts (higher activation resistances). Nevertheless, the researchers pointed out that, despite its higher cost, the use of Ti as the CC was very advantageous, allowing an increase in cell efficiency and stability, along with a decrease in system weight. They also pointed out that the use of lower catalyst

loadings (3 mg·cm^{-2} Pt/Ru and 1.3 mg·cm^{-2} Pt) allowed a 13% reduction in fuel cell cost, when compared to the common loadings (4 mg·cm^{-2} PtRu and 4 mg·cm^{-2} Pt). Thus, their work proposed a PS-DMFC with lower cost and weight, capable of working with higher methanol concentrations and less MCO, with a significant impact on further deployment of the technology, particularly for portable applications. These studies were also supported by a previous study from the same research group [106], concerning the effect of CC design/geometry on the performance of the PS-DMFC. The researchers designed and tested three different perforated CCs made from SS with different open ratios (namely, 34%, 41%, and 64%), in addition to an open window frame CC, used at both the anode and the cathode sides of the PS-DMFC. The results showed that feeding the cell with 1 to 7 M methanol concentrations and using the CC with the lowest open ratio (34%) on both the anode and the cathode sides allowed achieving the best power output (3.14 mW·cm^{-2}) with 2 M methanol. This was explained by the fact that a lower open ratio at the anode side led to lower MCO, lower contact resistances, and higher area for electron conduction. Similarly, a cathode CC with a lower open ratio allowed a higher metallic area for electron conduction and MEA support with higher compression, which decreased the contact resistance between the different fuel cell layers. Furthermore, a lower open ratio on the cathode side allowed increasing the water backflow and consequently decreasing the MCO. These findings were complemented by an experimental study carried out to evaluate the effect of the CDL properties on the power output of a PS-DMFC [107]. Their main goal was to explore the use of commercially available materials considered state-of-the-art components of CDLs for PS-DMFC systems. Therefore, four different carbon cloths and papers, presenting different properties such as thickness and surface treatment were tested. The maximum PD of 3.00 mW·cm^{-2} was achieved for a concentration of 5 M methanol, employing carbon cloth without MPL and a lower thickness as the CDL. This, according to the researchers, was mainly due to its higher porosity, which enabled higher oxygen and water diffusion rates, thus resulting in lower cathode activation losses. Additionally, regarding the MPL effect on the CDL structure, the authors verified that this was only advantageous when carbon paper was used. A similar study, this time exploring the effect of ADL properties on the performance of a PS-DMFC, was reported in [108]. The best performance was achieved using carbon cloth with MPL, presenting lower thickness and higher porosity, when the fuel had higher concentrations of methanol (maximum PD of 3.00 mW·cm^{-2} reached with a methanol concentration of 5 M). These improvements were mainly attributed to a better methanol transport and MOR rate on the anode side, combined with a lower MCO when operating the device with higher fuel concentrations. All these studies clearly showed that changes in the fuel cell structure and configuration are effective means to improve the performance and costs needed for real applications. Complementary to these studies, the work reported by Munjewar et al. [109] explored the effect of CC roughness on PS-DMFC performance. The researchers tested CCs made of 3 mm thick SS 316 perforated plates (with circular holes having an open ratio of 49.25%), obtaining different roughness on each pair of CC plates (cathode and anode) using a polishing machine. Hence, the roughness value depended on the sandpaper grade used, number of passes through the polishing machine, and the feed rate given to the sandpaper. In this way, seven pairs of CCs with average roughness values from 0.179 µm to 2.591 µm were fabricated. The cathode and anode GDLs were made of carbon cloth with a porosity higher than 70% and an MPL. These were assembled in a PS-DMFC with an active area of 5 cm^2 and a structure similar to that shown in Figure 1. To evaluate the assembled PS-DMFCs, the researchers performed polarization tests after OCV determination, as well as EIS and scanning electron microscopy (SEM) analysis. Additionally, they developed a mathematical model for mass transport resistance based on one-dimensional steady-state flow, which was obtained from EIS testing. In this way, they observed that the CC roughness had a significant impact on the PS-DMFC performance, and the best performance (maximum PD of 5.865 mW·cm^{-2} using 4 M methanol) was achieved with an optimum CC roughness of 0.869 µm. Moreover, the cell performance increased with the CC roughness as the

contact resistance decreased until reaching an optimal value, after which further increases in CC roughness were detrimental. In addition, since the tightening force was maintained constant for all cell assemblies, the variation in ohmic resistance was fully attributed to the surface roughness of the CC; accordingly, increasing the CC roughness increased the contact between the CC and GDL, thereby decreasing the ohmic resistance. From the SEM analysis, it could be clearly seen that increasing the surface roughness increased the surface area of the CC.

Considering the support provided by numerical models in exploring the PS-DMFC performance, the study by Zuo et al. [110] should also be mentioned. Their research, based on a temperature-induced convection effect model, showed that counterclockwise fuel circulation in the anode tank had a great impact by distorting the temperature distribution over the PS-DMFC, under open-circuit conditions. This effect was more obvious and significant for higher methanol concentrations. Moreover, for experimental verification of the model, a PS-DMFC was designed and manufactured, using 316L SS (thickness of 0.3 mm) CCs and PMMA to fabricate the fuel storage tank. The assembled cell with an active area of 4.0 cm^2 is depicted in Figure 6.

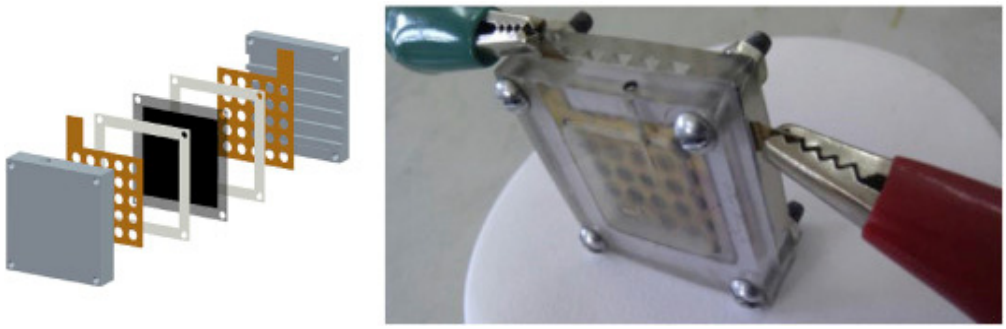

(**a**) (**b**)

Figure 6. Assembled PS-DMFC: (**a**) schematic of the structure; (**b**) picture of the device. Reproduced from [110] with permission from Elsevier 2018.

The results obtained indicated that, with an increase in the methanol concentration from 0.5 M to 3.0 M, the temperature increased, whereas the OCV decreased from 570 mV to 409 mV, respectively, due to MCO. Thus, this work can provide a theoretical basis and optimal operating parameters for safe start-up of DMFCs. Additionally, it is important to recall a previous study [111], in which the effect of non-isothermal conditions and gravity on the inner methanol concentration and thermal distribution of a PS-DMFC were taken into account to explore the cell operating process and performance. The simulation results showed that a more uniform reactant concentration and a higher temperature were obtained with the gravity effect. Again, the simulation results were experimentally confirmed, by operating a smaller PS-DMFC device (active area of 1 cm^2) using 316 SS CCs (thickness of 0.6 mm) with a single serpentine patterned flow field (Figure 7).

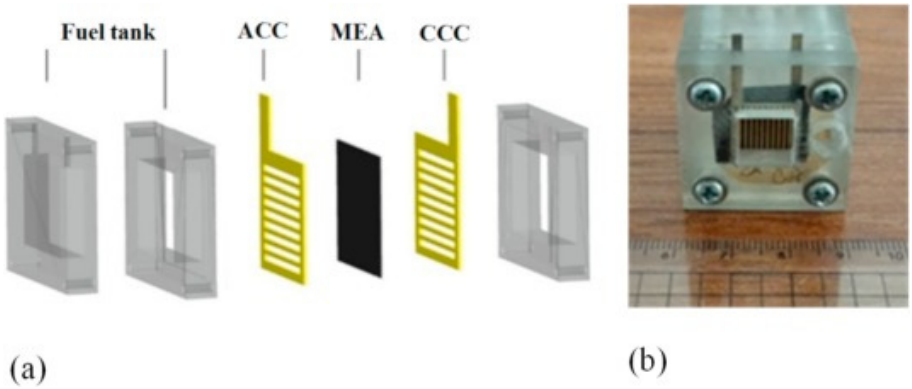

Figure 7. Assembled PS-DMFC: (**a**) schematic of the structure; (**b**) picture of the device. Reproduced from [111] with permission from Elsevier 2018.

The fuel cell was tested in three positions: horizontal orientation with the anode above the cathode ("Pattern A"), horizontal orientation with the anode below the cathode ("Pattern B"), and vertical orientation ("Pattern C"). The experimental results (polarization and power density curves) revealed that, within a certain methanol concentration range, the PS-DMFCs in Pattern A yielded better performance (maximum PD of 17.1 $mW \cdot cm^{-2}$ and 18.3 $mW \cdot cm^{-2}$ for methanol concentrations of 2.0 M and 3.0 M, respectively). It was also found that the cell performance in Pattern C (less affected by MCO due to gravity) surpassed that in Pattern A for high operating currents. However, for the high methanol concentration tested (4.0 M), operation in Pattern B reached a peak PD of 15.4 $mW \cdot cm^{-2}$ (higher than other two cell orientations) due to the complex tradeoff between the generated CO_2 bubbles and the optimal methanol concentration. Moreover, the researchers fully analyzed the anode CO_2 outflow and the cathode water backflow. The experimental results were in good agreement with simulation, demonstrating that both removals, CO_2 from anode and water from cathode, became more effective with gravity. Furthermore, they also highlighted that polarization curves in Pattern B tumbled in the high-current region, due to a greater generation of CO_2 bubbles at the anode, which moved upward due to buoyancy, thus blocking the methanol supply. This phenomenon was further investigated and presented in another paper [112], where the dynamic processes of bubble generation, growth, merging, and detachment in porous media and microchannels were analyzed in detail. The force responsible for bubble formation in the anode reaction region was calculated using a two-phase dynamic model. Both simulation and experimental results (obtained using a transparent PS-DMFC with an effective area of 1 cm^2) showed that the size and number of CO_2 bubbles were highly correlated with the fuel cell operating conditions. When the anode reaction was more intense, more CO_2 was produced, and smaller bubbles were observed. Thus, any method that accelerates the anode reaction can change the characteristics of the CO_2 bubbles. This can be achieved by increasing the operating temperature and/or methanol concentration. However, as mentioned before, establishing the best methanol concentration for a PS-DMFC is a tradeoff between increasing the cell temperature and increasing the methanol permeation toward the cathode. Furthermore, for any specified methanol concentration, the temperature of the cathode CC increase with the current density, while small CO_2 bubbles are more easily separated from the GDL and discharged to the microchannels. Yet, the movement of the bubbles in the microchannels is limited by the flow rate. Accordingly, when the flow path is a hydrophilic surface, the CO_2 bubbles move more easily in the channels and are more easily discharged from the flow field. Thus, on the basis of the relationship linking the viscosity, velocity, and methanol solution temperature at different current densities, the research group also reported the development of a thermal control microvalve channel structure [113]. The expectation was that the microvalve structure could achieve a self-adaptive fuel supply and effectively increase the power and stability during the PS-DMFC operation. According

to the model calculations of the whole cell (Figure 8) established using the COMSOL Multiphysics program, it was possible to see that the device operating at a small current density effectively reduced MCO. When the current density increased, the heat generated by the cell increased and the flow rate at the outlet of the microvalve increased, which was favorable for an increase in the cell reaction output.

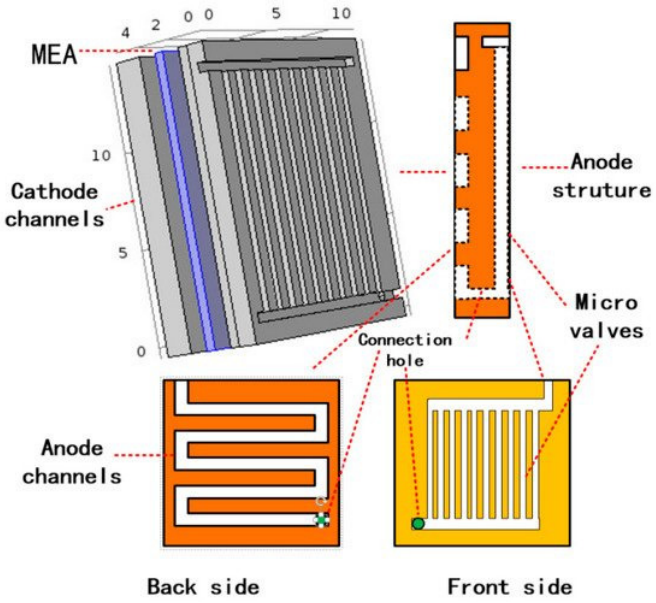

Figure 8. Schematic of the three-dimensional fuel cell model incorporating the microvalve structure [113].

The results obtained using the assembled self-adaptive PS-DMFC reached a maximum PD value of 16.56 mW·cm^{-2} when fed with a 2 M methanol solution, which was up to 7% better performance than a conventional one. Thus, the microvalve structure allowed the fuel cell to adaptively adjust the methanol solution flow rate, satisfying the proper demand of reactants throughout the operating process and effectively improving the working efficiency and stability, without external equipment, as it was simply driven by the heat generated by the device. Therefore, a further investigation of the self-adaptive thermal control design was pursued by the research group [114], in order to ensure that the PS-DMFC was always operating at an optimal temperature. Hence, according to the simulation and experimental analysis, a self-adaptive thermal control design of the fuel cell anode was realized using an "in-house" silicone heating sheet (SCS) together with a single-chip microcomputer in a PS-DMFC setup (active area of 1 × 1 cm^2). Thus, when operating the cell at an optimal temperature of 60 °C, the researchers revealed significant improvements in terms of the fuel cell system's output power and utilization compared with the traditional fuel cell. Moreover, while liquid water condensation and accumulation at the CCL are unavoidable in the conventional design, for the proposed cell with thermal control, no water drops appeared at the cathode, indicating excellent drainage characteristics. This was justified by the fact that the water produced in the ORR at the cathode evaporated due to the increased temperature and was removed from the fuel cell by convection. The same research group proposed another innovative approach, based on the particle swarm optimization (PSO) algorithm, to achieve an optimal thermal layout analysis and design of a PS-DMFC stack using printed circuit board (PCB) substrate [115]. In this work, it was possible to see that the three-dimensional thermal simulation model was in good agreement with their previous experimental results. This is of crucial importance since the heat transfer in the different designs of a DMFC had an influence on the temperature of each DMFC and the PS-DMFC stack assembled through the PCB, which can be used in portable electronic applications.

All of these conditions (environmental temperature and atmospheric pressure, as well as cell orientation and environmental conditions) can be considered external to the

system, as explained in a recent comprehensive study reported by Wang et al. [116], who investigated their effect on the performance of a PS-DMFC. In contrast, they considered internal/structural factors to include the hot press parameters of the MEA (temperature, pressure, and time), flow channel patterns (horizontal stripe pattern (HSP), vertical strip pattern (VSP), and circle pattern (CP)), and CC open ratios (35.8%, 45.6%, and 52%). They adopted both experimental and simulation methods based on previous studies [117]. Using this multivariable approach, results indicated that VSP was preferred for both anode and cathode CCs, with open ratios of 45.6% and 35.8%, respectively, in order to obtain the best performance. This was explained by a better discharge of the reaction products (CO_2 bubbles and water), along with a slight reduction in MCO. The first experimental polarization and power density curves were generated with a methanol concentration of 4 M, at 25 °C and approximately 75% relative humidity, using an MEA with an active area of 1.69 cm^2. In these conditions, the best performance, 14.91 $mW \cdot cm^{-2}$, was achieved using the MEA hot press parameters of 1.0 MPa, 135 °C, and 4 min. When exploring the effects of the external conditions, the researchers were able to reveal their significant impact on the performance of the fuel cell. Specifically, the vertical orientation with VSP channel was found to have the best performance, attributed to the high mass transport due to stronger natural convection. In addition, it was verified that the fuel cell performance increased with the vibration frequency from 0 up to 30 Hz, followed by a stabilization at higher frequencies (30 to 100 Hz). The external vibration (up to 30 Hz) could help in overcoming the surface tension forces between the liquid and the gas phase, promoting the discharge of CO_2 bubbles and facilitating methanol transport. Lastly, it was also verified that increasing the environmental temperature and atmospheric pressure had a positive impact on the PS-DMFC performance. The maximum PD increased from 5.5 to 17.5 $mW \cdot cm^{-2}$ when the temperature increased from −10 to 50 °C, due to an enhanced electrochemical reaction rate, reduced membrane resistance, and increased methanol diffusion rate at the anode side. Regarding the atmospheric pressure variation from 0.02 to 0.1 MPa (range selected to simulate the real atmospheric pressure changes with altitude, temperature, and weather), the decrease in PS-DMFC performance was explained according to the ideal gas law. A decrease in the oxygen concentration with a decrease in the atmospheric pressure led to a less favorable ORR at the cathode side. Overall, the researchers considered these findings useful as a guide for the development of high-performance and reliable portable power sources based on PS-DMFCs.

Another approach to achieve enhanced power outputs in PS-DMFCs was reported by Rao et al. [118], where MEAs (active area of 2.89 cm^2) were sandwiched between two similar Al reservoirs and CCs with flow channel plates having a rectangular and trapezoidal cross-sectional geometry. The microelectromechanical systems (MEMS) technology was employed for the fabrication of the microflow channels, etched in silicon wafers and finished with a metallic layer (Cr–Au) by sputter deposition, for enhanced electric conduction properties. This study showed for the first time that the flow channels with a trapezoidal cross-section enhanced the maximum PD output (6.64 $mW \cdot cm^{-2}$) when compared with the rectangular cross-section (3.9 $mW \cdot cm^{-2}$) for a 7 M methanol solution (concentration found to be optimum for the devices operating under passive mode in a vertical orientation at 25 °C). The researchers explained that these results were due to the higher reactant flow velocity, caused by the smaller cross-sectional area of the trapezoidal flow channels compared to the rectangular flow channels, with the same open ratio. In another study reported by Yang et al. [119], the silicon-based MEMS technology and CNTs were used to build porous silicon electrodes. Using plates exhibiting differences in terms of flow field and diffusion layer structure, distinct electrodes with a hill-like structure (HLS) and a through-hole silicon (THS) structure were manufactured. In addition, CNTs were used on the GDL surface to serve as a catalyst support, expanding the area for chemical reactions, thus improving their performance. As a control, conventional carbon paper (CP) GDLs were also used to evaluate the PS-DMFC performance at room temperature fed with a 2 M methanol solution. The THS electrode was placed only on the cathode side because

its relatively large holes were considered unsuitable for methanol diffusion. Thus, two anode–cathode combinations were investigated by the researchers, HLS (anode) with THS (cathode) and HLS (anode) with HLS (cathode), in addition to the control, CP (anode) with CP (cathode). The results revealed that the HLS–THS combination achieved the optimal performance (maximum PD of 0.186 $mW \cdot cm^{-2}$), which was 4.4 times higher than the performance of the conventional CP–CP (control) electrodes. According to the researchers, this was probably due to the dissimilar structure of the HLS–THS that provided a larger reaction area. In addition, the THS structure at the cathode had a higher contact with the PEM; thus, more oxygen could reach the catalyst, resulting in a more efficient process. Hence, the HLS–THS combination resulted in a device configuration with lower impedance and higher performance. Additionally, in this study, the researchers modified the methanol fuel, by adding surfactants (nonionic poly(ethylene glycol) (PEG) and anionic sodium dihexyl sulfosuccinate (SDSS)) to reduce the surface tension and enhance its wettability, as well as CO_2 removal capacity. According to the several tests performed, it was verified that, although PEG led to a greater improvement in wettability of the methanol solution than the SDSS surfactant, it severely obstructed the MOR. Therefore, the HLS–THS electrode combination was selected to explore the effects of adding SDSS (0%, 0.1%, and 0.5%) on the fuel cell performance. Through a comparison, the researchers confirmed that the use of SDSS substantially stabilized the voltage changes and prolonged the duration of the device. However, at higher concentrations, it enhanced both fuel wettability and MCO, consequently accelerating fuel consumption. Hence, an appropriate amount of surfactant can improve the CO_2 removal of PS-DMFCs.

Other variations in the methanol characteristics to overcome MCO were highlighted in the review by Abdelkareem et al. [120]. Specifically, by supplying high concentrations of methanol (reaching 100 wt.%) to the anode surface in the vapor phase through a gas layer where it was condensed, MCO could be greatly reduced to the level of using 2–4 M liquid methanol solutions. Thus, two possible types of PS-DMFCs, low methanol concentration (liquid-fed) and high methanol concentration (vapor-fed), as shown in Figure 9, were described in detail, not only from the thermodynamic point of view, but also in terms of the operation and structural conditions.

This is very pertinent since methanol transport and water transport are different in these two types of cells. As aforementioned, in liquid-fed DMFCs, water flooding of the cathode is a common problem that limits the oxygen access to the active cathode sites. On the other hand, in vapor-fed DMFCs, water deficiency appears at the anode, and the possibility of an incomplete MOR is higher, especially at low operating temperatures. Thus, in the vapor-fed passive DMFC, a water management layer (WML) was added to the cathode surface to reduce water loss to the surrounding atmosphere and to enhance the water back-diffusion from the cathode to anode. However, despite the possibility of using high methanol concentrations, the authors reported that no commercial products are yet available. Nevertheless, they pointed out that good porosity and high hydrophobicity are important characteristics for liquid- and vapor-fed PS-DMFCs. Furthermore, the application of graphene on the composite membrane structure of Nafion® was shown to be promising, since it did not affect the ionic conductivity and allowed restricting the MCO. The effect of typical GDLs (PTFE-treated carbon paper or cloth) on the performance of liquid- and vapor-fed PS-DMFCs, under active operation conditions, was also investigated by Abdelkareem et al. [121], in line with a previous study from Oliveira et al. [122] for the liquid-fed PS-DMFC. It was shown that the GDL properties played a crucial role in the performance of these devices, and, although catalyst utilization was higher when using carbon paper than when using carbon cloth, the fuel cell performance using the latter was enhanced in both liquid- and vapor-fed PS-DMFCs. The researchers credited the results from this comparative study to the uniform distribution of the pores, rougher surface, and lower tortuosity of the carbon cloth, which allowed homogeneous mass transfer at the anode and cathode. Furthermore, it was verified that the detachment of water droplets was easier in the case of the carbon cloth, due to its higher dynamic hydrophobicity [123].

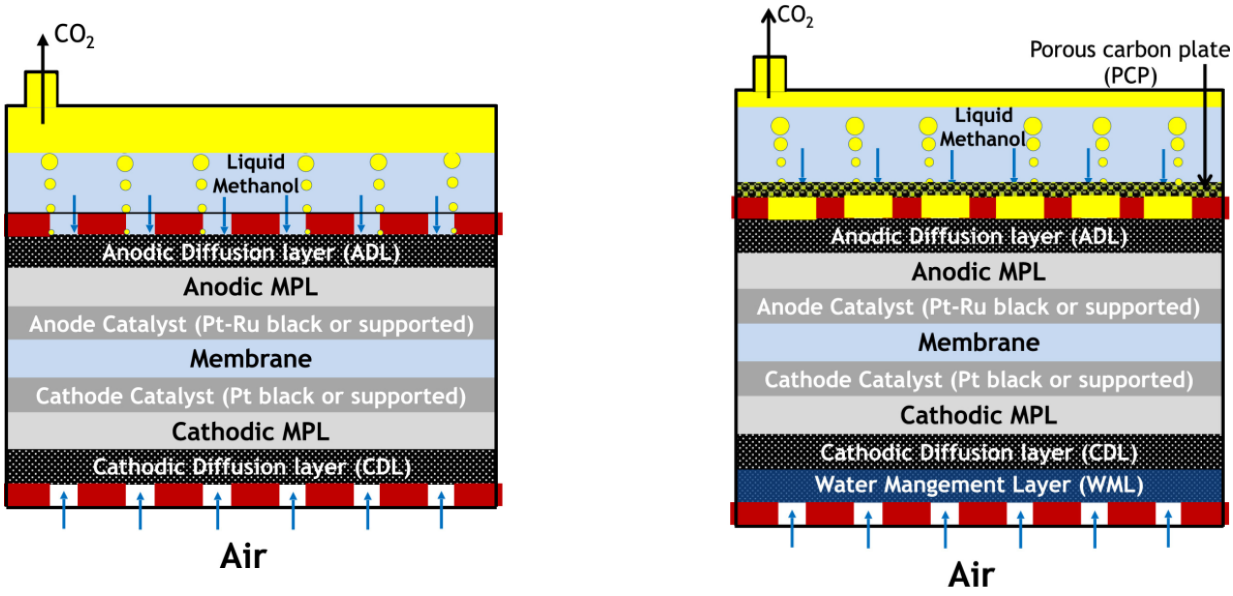

Figure 9. Schematic diagram of passive DMFCs: (**a**) liquid-fed; (**b**) vapor-fed. Reproduced from [120] with permission from Elsevier 2018.

An alternative approach to supply high-concentration methanol solutions in a limited fuel tank was reported by Zuo et al. [124]. These researchers developed and tested the performance of a fuel cell with an anode dual cavity using a simpler structure (Figure 10), where the barrier layer in the middle of the cavity could be easily replaced.

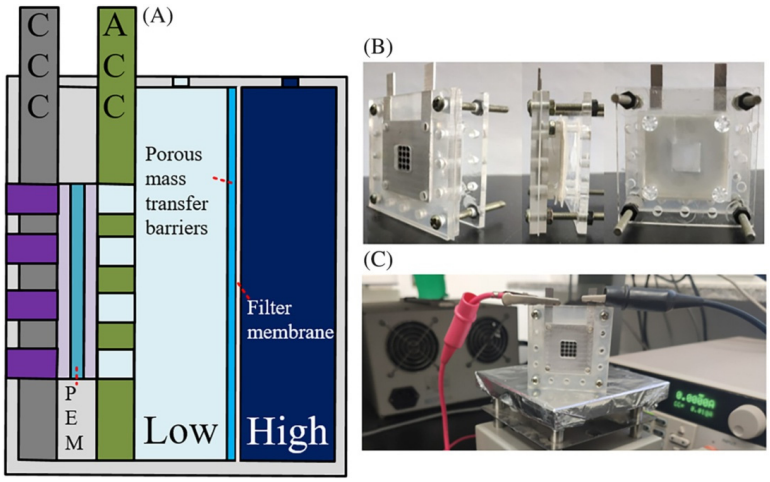

Figure 10. PS-DMFC with anode dual-cavity structure: (**A**) schematic diagram; (**B**) picture of the assembled device; (**C**) picture of the experimental setup. Reproduced from [124] with permission from John Wiley and Sons 2021.

The major goal of this approach was to make the structure suitable for use in small DMFCs, in order to supply high-concentration methanol solutions. Thus, the effect of the SS felt, plastic porous dielectric barrier layer, and hydrophilic and hydrophobic filter membrane on the performance of a PS-DMFC was explored. The experimental results showed that the maximum performance with a dual-cavity structure was higher than that with a traditional structure (maximum PD of 17.3 $mW \cdot cm^{-2}$). Moreover, the researchers also demonstrated that the dual-cavity structure with a high methanol concentration could effectively extend the cell discharge time, especially under high current densities. In

addition to the fact that the mass transfer barriers with different pore sizes had obvious differences in methanol barrier performance, hydrophilic and hydrophobic membranes could effectively affect the methanol permeability. Thus, as stated by the researchers, an appropriate filter membrane (efficient, easy to prepare, and replaceable) should be selected according to the substrate and ability to maintain a constant concentration in the low-concentration cavity during cell operation. As pointed out by the authors, these issues need to be further studied, along with a strategy for increasing the fuel concentration without hindering the anode water supply.

A more radical approach to a new type of PS-DMFC was presented by Lu et al. [125], which they called the "all-solid-state" passive DMFC. It was based on "solid methanol" fuels prepared by combining a methanol solution and an absorbent material. Thus, it was very different from conventional liquid-fed devices, as highlighted in Figure 11.

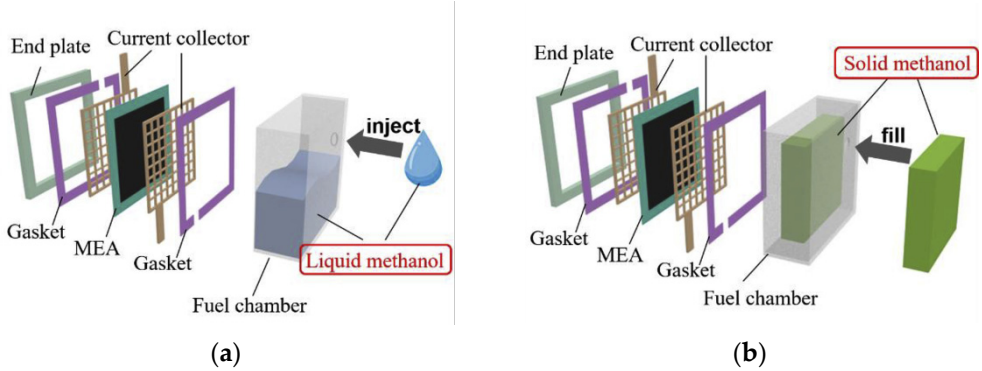

Figure 11. Schematic diagram of passive DMFCs: (**a**) conventional liquid-fed device; (**b**) new solid-state device. Reproduced from [125] with permission from Elsevier 2020.

It should be recalled (as the authors pointed out) that the freezing point of methanol is as low as −97.8 °C, a temperature that is not suitable for operating DMFCs or for easily obtaining solid methanol (i.e., by freezing methanol and methanol aqueous solutions). Thus, to explore a feasible method for preparing "solid methanol", various functional/absorbent materials were used, namely, absorbent cotton, commercial super absorbent polymer (SAP) (which is composed of 88% sodium polyacrylate, 10% water and 2% crosslinker), and silica aerogel. In this way, the researchers showed that the newly proposed all-solid-state PS-DMFC could be operated in any orientation, while the performance remained stable. The results showed that the solid fuels improved the mass transport, mainly due to the disappearance of CO_2 bubbles on the anode side, which diffused directly outside the cell without hindering methanol and water transport. Furthermore, compared to the liquid methanol solution, using "solid methanol" in PS-DMFC increased the maximum PD and the discharge energy of the DMFC, under the same experimental conditions. The best performance using a "solid methanol" fuel was achieved using SAP, 20.5 $mW \cdot cm^{-2}$, which was 30.8% higher than that using a liquid methanol solution. In addition, the antileakage properties of the "solid" fuels made the PS-DMFCs safer and more portable. However, as pointed out, despite the good results achieved with the SAP-based "solid methanol" fuel, this material needs to be produced in advance, rendering it unsuitable for continuous supply. Another variation was reported in the comprehensive study performed by Boni et al. [126], where the effect of two ACLs (PtRu/black and PtRu/C), as well as the CC open ratio, on the performance of a PS-DMFC was investigated, along with the incorporation of a liquid electrolyte (LE) layer. The LE layer consisted of piled hydrophilic filter papers, which were soaked in a diluted sulfuric acid solution and introduced between two Nafion® membranes. In this case, the aim was to reduce the MCO and to improve the performance of the PS-DMFC, following previously reported studies [127]. Therefore, a conventional PS-DMFC (active area of 25 cm^2) was assembled with SS 316L CC plates with opening ratios of 45.40%, 55.40%, and 63.05%, and operated with 1–5 M methanol solutions.

The experimental results showed that the fuel cell performance was improved when using the MEA with two ACLs (PtRu/black + PtRu/C, MEA-2) compared with the conventional one using the same loading with only one type of ACL (PtRu/C, MEA-1) (see Table 2). The maximum PD (3.872 $mW \cdot cm^{-2}$) was obtained with the two ACLs and the CC with an open ratio of 55.40%, using a 3 M methanol solution. However, it was also shown that the optimum methanol concentration, that which gave the best cell performance, depended on the CC open ratio, since a higher open ratio promoted the mass transfer of the reactants and facilitated product removal, thereby improving the cell performance, but also leading to an increase in MCO, which adversely affected the cell performance. The results also showed that the fuel cell performance was improved by incorporating the LE layer, due to a decrease in the MCO and a decrease in the mass transfer losses on the cathode side.

Concerning different approaches to fabricate affordable and efficient DMFCs, it should be highlighted that improving the activity and reducing the Pt loading are two main issues that must be addressed by the scientific community. Thus, there has been an enormous effort by researchers of the Fuel Cell Institute, Universiti Kebangsaan Malaysia, to address these issues. Ramli and Kamarudin [128] provided a review paper focused on the activity of Pt-based catalysts combined with alloys, metals, transition metals, metal carbides, metal nitrides, and various different carbonaceous materials as their support. Ishak et al. [129] compiled information regarding the synthesis and characterization of advanced biogenic Pt nanoclusters from several plant extracts drawn from agricultural waste (such as banana peels, pineapple peels, and sugarcane bagasse extracts) to improve the MOR in DMFCs. Another paper, previously mentioned [37], summarized the recent progress on anode catalysts, both noble and noble-free, in acidic/alkaline electrolyte for MOR, as well as on the types of catalyst support materials for DMFC anodes. This paper also highlighted the major challenges and future perspectives in achieving the optimum performance from the perspective of tailoring the properties of MOR electrocatalysts. However, a more focused compilation/review regarding the analysis of the current status, opportunities, and challenges in fuel cell catalytic application of aerogels was provided by Shaari and Kamarudin [130]. This report included aerogel synthesis methods for catalysts and catalyst supports, and it discussed the potential of aerogel in fuel cells in terms of electrochemistry and power density, as well as the structure and operating conditions. Lastly, the report provided by Shaari et al. [131] regarding the application of carbon quantum dot (CQD) and graphene quantum dot (GQD) composites in fuel cells should be mentioned, in which their potential to enhance the performance of this technology was clearly stated. These studies are highlighted since they can be a reference for researchers to identify different opportunities to improve fuel cell performance, which relies heavily on costly PGM catalysts, such as Pt and Ru. The goal should be to modify the catalyst structure and morphology in order to increase the performance of the devices, while reducing their overall cost toward their commercialization. Accordingly, Jeong et al. [132] proposed the use of Ru-sputtered Pt/C-based MEAs in PS-DMFCs, reducing the use of Ru by more than 80% compared to the conventional Pt-Ru/C (50:50 wt.%)-based MEAs. The results showed an increase in performance and catalytic durability using the Ru-sputtered MEAs (active area 1×1 cm^2) and a 4 M methanol solution. The OCV and the maximum PD for the Ru-sputtered MEA were 0.417 V and 3.28 $mW \cdot cm^{-2}$, whereas values for the standard (Pt/C) MEA were 0.52 V and 3.01 $mW \cdot cm^{-2}$, respectively. In addition, while monitoring the OCV for 1 h, it was found that the Ru-sputtered MEA presented an 11.2% decrease from the initial value, while the standard MEA presented a decrease of 17.4%. The researchers demonstrated that the different fabrication process allowed a reduction in the cost, since the industrial infrastructure for sputtering is easily available, due to the development of the semiconductor industry. As a further step in the use of PGM catalysts, Jeong et al. [133] studied the deposition of both PGMs (Pt and Ru) by sputtering on the electrolyte membrane. The thickness of the sputtered Pt and Ru was also tested to determine the structural effect of sputtered layers. The MEAs with four different levels of surface roughness were first prepared by rubbing Nafion® 117 with different sandpapers. The performance of the

PS-DMFCs with the new sputtered MEAs was measured, and that the comparison revealed that the device with a thin ACL (75 nm thick Ru on 150 nm thick Pt) showed a higher PD (0.053 $mW \cdot cm^{-2}$) than that with a thick ACL (0.033 $mW \cdot cm^{-2}$). Although both power curves apparently exhibited an increasing tendency, the PS-DMFC with a thicker CL could not outperform the thin one at high current densities, due to the disturbance of mass transport by the thick ACL. The OCV of the PS-DMFC with a thin CL was lower (0.177 V) than the OCV of that with a thick one (0.216 V), due to an insufficient loading of Pt and deficient active sites, since these were formed only at the interface between the electrolyte and the electrode by the sputtering process. The researchers observed that the performance of the PS-DMFCs using the as-prepared MEAs (0.053 $mW \cdot cm^{-2}$) was improved as the roughness of the MEA was increased (the best value obtained was 0.086 $mW \cdot cm^{-2}$); however, excessive roughness induced a deterioration of the performance (0.046 $mW \cdot cm^{-2}$). Consequently, it was concluded that further investigations into the relationship between the roughness of the electrolyte membrane and the electrochemical performance were required to clarify the processes inside the PS-DMFCs and the sputtered ACLs. Nevertheless, two meaningful results were obtained: (1) sputtered Pt and Ru can be used as the ACL for PS-DMFCs; (2) the structure of the ACL (thickness of PtRu) and the roughness of the electrolyte membrane are significant parameters affecting the DMFC performance.

In a more conventional approach, an alternative strategy to enhance the electrocatalyst performance is the optimization of its interaction with the support material (as stated earlier). Therefore, an ideal catalyst support should offer good catalyst–support interaction and electrical conductivity, as well as a large surface area and mesoporous structure, to bring the catalyst NPs close to the reactants. Some practical examples applied to PS-DMFCs can be found in the study reported by Fard et al. [134], which investigated the application of N-doped CNTs as catalyst supports for PtRu and Pt NPs in a DMFC. They designed and fabricated different MEAs with an active area of 4 cm^2, with CB (MEA1), CNT (MEA2), and N-CNT (MEA3) as the catalyst supports, using 20% PtRu and 20% Pt as the anode and cathode catalysts, respectively. The PS-DMFC was tested at room temperature with 2, 3, and 4 M methanol solutions. The results showed that the cell with PtRu/N-CNT (MEA3) presented the best performance, with a PD of 26.1 $mW \cdot cm^{-2}$, which was 18% and 62% higher than that obtained for MEA2 and MEA1, respectively. The researchers concluded that N-CNTs remarkably improved the physical and electrochemical characteristics of the catalyst by increasing the electrical conductivity, due to a more uniform distribution of smaller metal NPs. This boosted the interaction between the support and the catalyst, as well as enabled the long-term stability of the MOR. Following the same logic, another approach was reported by Abdullah et al. [135], whereby a novel titanium dioxide carbon nanofiber (TiO_2-CNF) support was introduced on a PtRu catalyst. The TiO_2-CNF was prepared by electrospinning, followed by carbonization and PtRu deposition (PtRu/TiO_2-CNF). The synthesized electrocatalyst, PtRu/TiO_2-CNF, was tested in a PS-DMFC, and the performance was compared with a commercial electrocatalyst (PtRu/C) using the same composition (20 wt.% of PtRu), an MEA with an active area of 4 cm^2, and a 3 M methanol solution. The PtRu/TiO_2-CNF showed a higher performance (3.8 $mW \cdot cm^{-2}$) than the commercial electrocatalyst (2.2 $mW \cdot cm^{-2}$), almost twofold higher. The researchers attributed the highest catalytic activity to the nanofiber catalyst structure and the introduction of TiO_2 as support. The researchers reported other research work regarding the optimization of the ratio between the main catalyst (PtRu) and supporting material (TiO_2-CNF), as well as the electrocatalyst loading, toward a high DMFC performance [136]. The optimization process involved a screening process followed by a response surface methodology (RSM), a collection of statistical and mathematical techniques that allow evaluating the interaction between different parameters, generating substantial data from fewer experiments. In this study, the PtRu composition and the electrocatalyst loading were varied in the ranges of 15–60 wt.% and 0.45–0.7 $mg \cdot cm^{-2}$, respectively. It was verified that the cell optimization using RSM, with the PtRu catalyst composition and electrocatalyst loading as factors and

the current density as a response, resulted in a quadratic model with good correlation between the predicted and experimental data (error of 0.4%). The best PtRu/TiO_2-CNF performance was confirmed by an experimental test, achieving a power density identical to the one predicted. Alias et al. [137] reported a different application for TiO_2, since this material was added to the CNF and CB material used in the MPL of the anode. The surface characterization of the modified MPL with different porous layers was performed using SEM analysis. The modification of the CNF and CB MPL with TiO_2 allowed achieving a maximum PD of 10.73 mW·cm^{-2} and 11.47 mW·cm^{-2} with a 3 M methanol solution and a reduction in these values by 2.8% and 11.9% using a 5 M methanol solution, respectively, at room temperature. The TiO_2 modification was advantageous, since it could provide good electron conductivity and control the methanol transport. Moreover, the EIS tests showed that the addition of TiO_2 provided a good mass transfer and lower charge transfer resistance, facilitating CO_2 removal and methanol transport to the ACL. Long-term analysis of the modified MPL with different porous layers showed that the resulting current increased and was more stable. The reductions observed after 3 h of operation with a 3 M methanol solution using CNF-TiO_2 and CB-TiO_2 were estimated to be only 0.31% and 1.37%, respectively. It should be highlighted that the catalyst loadings used in this study (see Table 2) were significantly higher than those used in other studies; thus, a direct comparison of their performance needs to consider this factor.

Ramli et al. [138] explored the use of alternative catalyst supports, namely, carbon nanocages (CNCs) for PtRu, due to their high specific surface area and electrical conductivity, good structural properties, and low cost. The purpose of this study was to demonstrate the electrocatalytic activities of four synthesized Pt-based bimetallic compounds, PtRu, PtNi, PtCo, and PtFe, on the new carbon support. The CNC support was synthesized from a polypyrrole source by pyrolysis, followed by the preparation of the electrocatalysts by employing a microwave-assisted ethylene glycol reduction method, which was considered by the researchers to be a simpler and faster method. The properties of all electrocatalysts and supports were structurally and morphologically characterized, followed by testing in a PS-DMFC, in conditions similar to those used by Abdullah et al. [135]. The new electrocatalysts were used at the anode side, and a 2 M methanol solution was fed to the system. The results showed that the PtFe/CNC electrocatalysts had a better CO tolerance than PtRu/CNC, PtNi/CNC, and PtCo/CNC. The tests in the PS-DMFC with the PtRu/CNC electrocatalysts showed a maximum PD of 3.35mW·cm^{-2}, which was 1.72 times higher than that obtained with a PtRu/C commercial electrocatalyst. This was due to the advantages of the CNC over C as a support material, as well as to the synergetic interaction with the bimetallic PtRu, which enhanced the MOR process. Hence, PtRu/CNC was considered a promising anode catalyst for PS-DMFCs.

2.2. Alkaline DMFCs

As mentioned before, recent advances in the preparation of chemically stable AEMs opened a window of opportunity for the development of high-performance fuel cells, including PS-DMFCs. Thus, Golmohammadi et al. [139] reported a sustainable approach for the fabrication of alkaline MEAs using new PGM-free electrocatalysts for the ORR, such as nickel–cobalt (Ni–Co) oxides, with biomass-based CNFs as the support. This strategy had some important advantages including the use of renewable and abundant resources, eco-friendliness, easy processing, and low cost. In fact, the researchers resorted to an endogenous plant called "Karrapo" (KP), which they had previously investigated due to its ability to form porous structures [140]. In this way, KP was used for the first time as a low-cost biomass to produce nanofibers in order to serve as the framework to synthesize Ni–Co nanocapsules with a large surface area. According to the researchers, preparing the KP and Ni–Co (Ni–Co/NFKP) materials was simpler and did not involve expensive and toxic materials. The new electrocatalysts were compared to commercial Pt/C catalysts, testing two different MEAs, i.e., MEA-1, where Pt/C was used as the cathode and anode catalyst, and MEA-2, where Ni–Co/NFKP was used as the cathode catalyst

and Pt/C was used as the anode catalyst. The active area of each MEA was 4.75 cm^2, and an AEM A-006 (OH^- form, Tokuyama membrane) membrane was used, along with 316 SS as the CCs. A methanol solution (5%) with KOH (10%) was employed as the fuel for operating the AEM-PS-DMFC. The results showed similar polarization curves, with the major differences observed for the low-current-density region, where MEA-2 had a higher activation overpotential than MEA-1. Moreover, in the stability test, MEA-2 showed a lower decrease in the current density than MEA-1, indicating that the use of Ni–Co/NFKP at the cathode led to a better electrocatalytic activity and stability. One could argue that the PD obtained with the proposed material did not show an improvement and that the stability test was not overwhelmingly clear; however, considering the overall eco-sustainable approach, it is relevant to further investigate this MEA fabrication route.

A different fabrication route was presented by Farzaneh et al. [141], where, in continuation of their previous work [142], nanostructured pyridinic-rich nitrogen-doped graphene was applied as an electrocatalyst for ORR in alkaline fuel cells. In this study, the performance of hydrothermally produced nitrogen-doped reduced graphene oxide (NRGO) with a nitrogen content of 4.6 wt.% was compared with a commercial Pt/C as the cathode electrocatalyst for a PS-DMFC using an AEM electrolyte. The device (an "in-house" AEM-PS-DMFC with an active area of 4.75 cm^2 and 316 SS CCs) and the operating conditions used were very similar to those used in a previous study [142]. The AEM was A-006 (OH^- form, Tokuyama membrane), the ACL was a commercial 20 wt.% Pt/C catalyst, and methanol solutions of 1.5, 3.0, and 4.5 M were used with 1 M KOH as fuel. An extra reference electrode was placed in the methanol solution tank to allow recording the cathode polarization curves. The results obtained indicated that the cell with the NRGO cathode could operate at higher methanol concentrations, since, for the same methanol concentration (3 M), the maximum PD, the fuel or faradaic efficiency, and the current stability (measured at 0.4 V for 7 h) were about 309%, 369%, and 177% higher than when using Pt/C. Moreover, a higher cathode CC temperature was observed in the cell with Pt/C (in spite of its lower power output), which is evidence of the oxidation of permeated methanol on the cathode surface (exothermic MOR). This observation was validated by EIS, since the researchers found that the COads (an MOR intermediate) oxidation reaction on the cathode side of the cell with Pt/C led to a large impedance of the overall cell operation, in contrast to that using NRGO. In summary, the results showed that using an efficient metal-free and highly methanol-tolerant ORR electrocatalyst, such as NRGO, is a promising approach for designing more efficient and cost-effective AEM-PS-DMFCs.

2.3. DMFC Stacks

In spite of all the advances and improvements reported for PS-DMFCs, with an acidic or alkaline electrolyte, it should be recalled that a single-cell voltage output is limited to less than 0.5 V; thus, for small portable applications, with higher voltage requirements (usually higher than 2.0 V), this value cannot be achieved using a single cell. Thus, a DMFC stack, which is sometimes referred to as a cell network, can be a solution to this problem. Moreover, simulation tools can help by providing crucial information regarding the different devices, as previously shown for single cells. An example for mini portable applications, such as cell phones, tablets, and battery chargers, targeting a current and voltage of 1400 mA and 3.7 V, respectively, for a cell network power of 5.18 W, was reported by Ismail et al. [143]. Their approach was based on the development of an optimization model describing DMFC stacks, via a cell integrated network. Thus, a superstructure model was presented, which accomplished the design parameters for a target voltage and current of 3.7 V and 1400 mA, respectively. This was achieved through the optimization of 16 cells arranged in series using Matlab. In summary, an active area of 128 cm^2 was necessary, which resulted in an individual active area of 8 cm^2. Moreover, the model also predicted the fuel requirements and the total CO_2 emission flow rate via the cells. The volume for the cell network was estimated to be 334.60 cm^3 with a price of 1400 USD, according to the economic analysis provided in the study. Therefore, this work presented

a detailed optimization model and economic analysis for the design of DMFC stacks. In order to optimize the output characteristics and the energy conversion of the PS-DMFC stack and to take a step further in the analysis, Fang et al. [144] presented a new modeling approach, based on the Debye–Hückel ionic atmosphere theory, to describe the charge conduction and electrochemical kinetics during the polarization coupling process of each cell unit within the stack. The proposed model was solved numerically by LabVIEW of National Instruments, using a model structure of a PS-DMFC stack made of four-cell units interconnected in series. The simulated current–power profiles obtained from the model were experimentally validated by assembling an "in-house" PS-DMFC stack made of four-cell units (with an unitary active area of 1.2 × 1.2 cm^2) connected according to the geometry and physical parameters of the presented model (Figure 12).

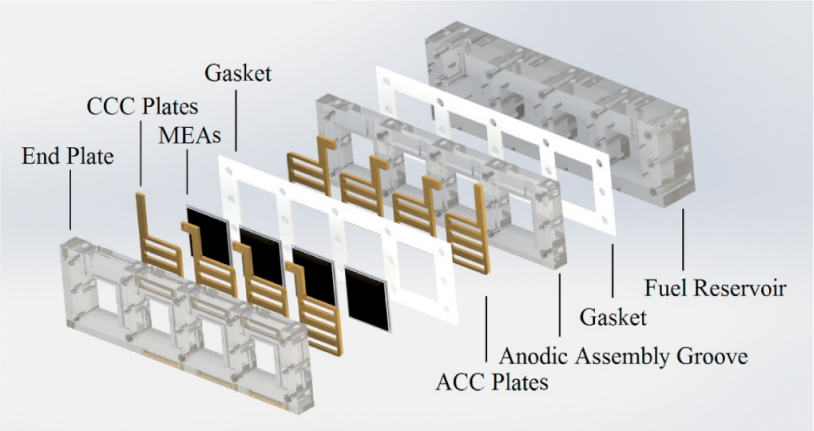

Figure 12. Schematic of the assembled PS-DMFC stack to verify the model based on Debye–Hückel ionic atmosphere theory in exploded view. Reproduced from [144] with permission from Elsevier 2021.

The tests were performed with increasing methanol concentrations from 1 to 4 M. For the higher methanol concentration, different oxygen concentrations were tested, whether obtained directly from the air environment (volume fraction of 21%) or using an air-tight box (volume fraction of 50% and 95%). The effect of operating temperature, which was increased from 20 to 60 °C, was also assessed using an incubator. In summary, this new approach allowed the analysis and simulation of the polarization curves with a reduced error (about 8%). An improvement in the output power was achieved (by about 2%, on average) when increasing the oxygen concentration. Moreover, it was also observed that increasing the operating temperature weakened the coupling forces within the stack. Additionally, by analyzing the results of the dynamic operation of the stack while continuously changing the operating current, it was shown that the polarization coupling caused a voltage peak during unloading. Furthermore, high loading currents and unloading speed raised the voltage peak. These dynamic discharge profiles of instant loading and unloading are important to be considered, since they characterize the momentary switching process of the device. Moreover, as the MCO decreased, it was demonstrated that the dynamic energy conversion efficiency of the assembled PS-DMFC stack was higher. Therefore, the proposed model was considered as a breakthrough for solving the polarization coupling between PS-DMFC stacks and modern microelectronic portable systems, which will be addressed in future studies.

Another strategy for the design and fabrication of a quick-fit architecture PS-DMFC, which was extended to two- and six-cell stack working prototypes, was reported by Abraham and Chetty [145]. The authors presented a novel clamping mechanism (a single SS tightening cylinder) as an alternative to the conventional screw-bolt-based clamping design for planar PS-DMFCs with an active area of 3 × 2 cm^2. This new clamping mechanism was able to hold the cell components together firmly, avoiding fuel leakage and limiting cell

resistance, in addition to being easily extendable for stack operation, providing the possibility of individual cell diagnostics, and allowing the replacement of a faulty individual cell. Moreover, the researchers also used these new configurations to evaluate the performance of Pt and PtRu catalysts prepared by pulse electrodeposition on Ti mesh-based electrodes, which were employed and compared to the traditional carbon-based electrodes on the basis of their previous studies [146] and the well-known beneficial physicochemical properties of Ti mesh. In this study, the Ti mesh was used in order to decrease the MEA overall thickness, by acting as a catalyst support and a CC. The researchers showed that it was even able to replace the GDL at the anode. For the cathode side, the absence of a GDL drastically reduced the cell performance, which was attributed to limited diffusion of O_2. Thus, the best performance was achieved with a 2 M methanol solution, PtRu on an 80 mesh (47% open ratio) Ti anode, and Pt/C-coated GDL with 40 mesh (71% open ratio) Ti cathode, reaching an OCV of 0.496 V and a maximum PD of 2.7 $mW \cdot cm^{-2}$. This optimized single cell was extended to two-cell and six-cell mini-stacks, by connecting the cells in series using copper wires with alligator clips on each end (Figure 13).

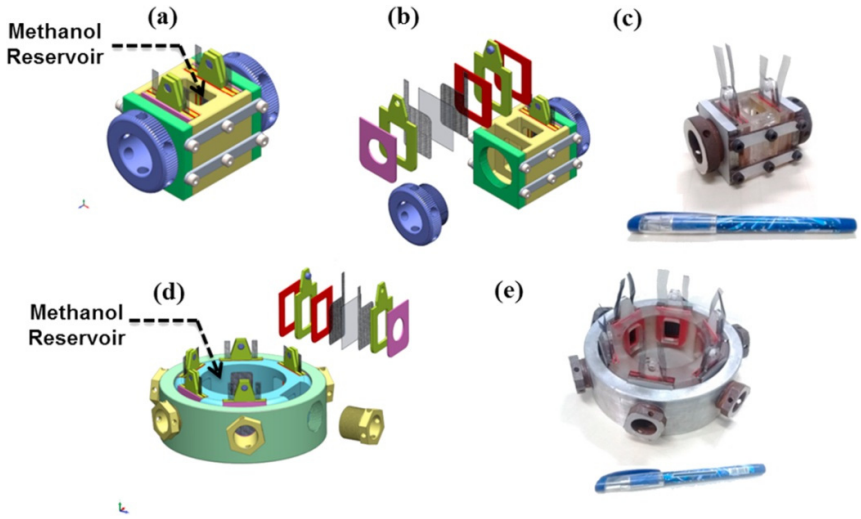

Figure 13. Schematic of novel quick-fit PS-DMFCs stacks: (**a**) configuration of the two-cell mini-stack; (**b**) exploded view depicting the various components and (**c**) picture of the device; (**d**) configuration of the six-cell mini-stack and (**e**) picture of the device. Reproduced from [145] with permission from Elsevier 2021.

The six-cell mini-stack (total active area of 36 cm^2) reached an OCV of 2.9 V and a maximum PD of 1.7 $mW \cdot cm^{-2}$, while the two-cell mini-stack (total active area of 12 cm^2) reached an OCV of 1 V and a maximum PD of 2.5 $mW \cdot cm^{-2}$. The decrease in power for the six-cell stack could be explained by an increase in resistance owing to the higher number of cell connections. Nevertheless, further tests were performed with the six-cell PS-DMFC stack, which was able to operate at 1.5 V for 2 h with a 2 M methanol solution and was also used to power a small fan motor, as proof of concept.

As mentioned above, an important consideration in the DMFC stack structure design is the internal connections, and this aspect was highlighted in the paper by Wang et al. [147]. The main objective of their study was to develop a high-performance low-cost bipolar passive DMFC stack for portable applications, using a novel CC design, which seamlessly integrated internal and external electrical connections, thereby reducing the resistance losses. In this way, the researchers assembled in series a typical four-cell passive DMFC stack, where each MEA had an active area of 2.0×2.5 cm^2 (Figure 14). The maximum PD of the passive stack, when tested under different methanol concentrations, was 18.7 $mW \cdot cm^{-2}$ at 3 M. Moreover, the researchers also studied the effect of two orientation modes for the BPs on the performance of the PS-DMFC stack, which they called modes A and B, corresponding to the cathode air channels placed parallelly and vertically, respectively.

The results indicated that the PS-DMFC stack in mode B exhibited a better and more stable performance than its counterpart in mode A when discharging high currents, with almost no difference when discharging low currents. These findings were explained by the fact that, in mode B, the water produced and accumulated in the air channels at the cathode under high discharging currents can be easily transferred to the outside through the air channel by gravity. Additionally, during long-term testing, they observed that the PS-DMFC stack in mode B had a better performance and, thus, better MOR and ORR kinetics. Lastly, a "good" performance of the bipolar passive DMFC stack was confirmed by powering a micro fan (rated power 150 mW) every 20 days for 100 days. This test also revealed that the stack performance deterioration aggravated with time; on the 100th day, the performance was only 83.33% of the initial value. This was explained by the attenuation of the catalytic performance in the MEAs, caused by MCO and catalyst contamination by pollutant compounds present in the environment, such as sulfides.

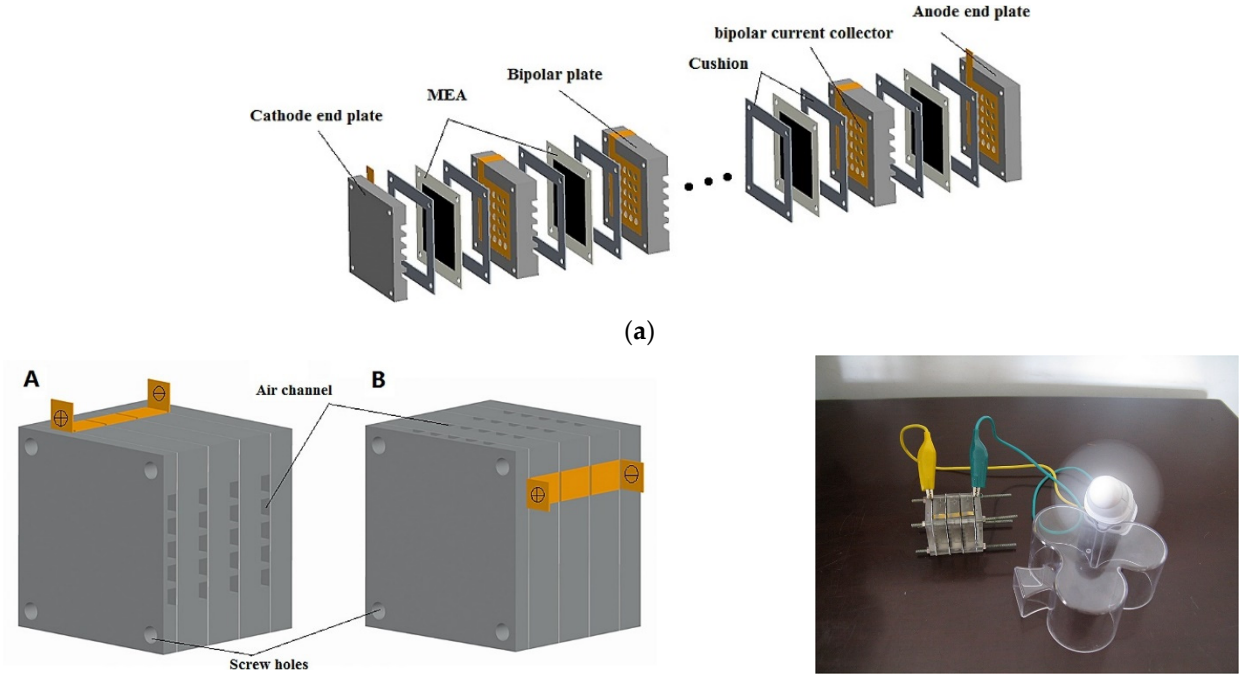

Figure 14. (**a**) Schematic of the proposed bipolar PS-DMFC stack structure; (**b**) the tested orientations of bipolar plates (BPs); (**c**) picture of bipolar PS-DMFC stack applied to power a small operating fan. Reproduced from [147] with permission from Elsevier 2017.

Further research regarding the quest for alternatives to metallic BPs was also explored by Hao et al. [148]. As previously pointed out, this is a key issue, since these components should have high electrical conductivity and excellent mechanical properties, as well as low fabrication costs. However, they can be corroded in the acidic environment of the PEM fuel cell anode, even if anticorrosion coatings are applied. Hence, this study was pertinent, where BPs made of magnesia phosphate cement (MPC) composite with two different patterns (nine and 16 circular holes with same total hole area) fabricated through a hot-press-assisted hydration process were used, following their previous studies [149,150]. According to the authors, the MPC material satisfied both the technical and the cost targets of the US Department of Energy 2015 requirements. Both the single-cell PS-DMFC (with an active area of ~4.52 cm^2, approximate to the total area of the BP holes) and the fuel cell stack (composed of three of these single cells in series) were assembled using the novel MPC-based BPs (Figure 15).

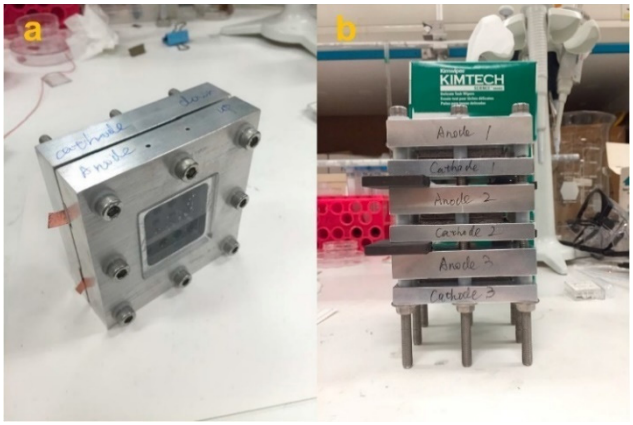

Figure 15. Pictures of (**a**) the single cell PS-DMFC and (**b**) the fuel cell stack assembly using MPC-based BPs. Reproduced from [148] with permission from Elsevier 2019.

The performance tests were conducted at 70–90 °C, by placing them horizontally inside an oven. The results showed that the use of MPC-based BPs enabled a good performance, since they were electrochemically stable and presented low impedance. Moreover, the PS-DMFC stack assembled with 16-hole MPC-based BPs achieved a maximum current density of 79.78 mA·cm^{-2} and a PD of 25.54 mW·cm^{-2} at 80 °C, when fed with 6.0 M methanol solution. In addition, the researchers demonstrated that the mass and heat transfer of the 16-hole MPC-based BPs provided better performance than the that of the nine-hole ones (see values in Table 2), which was attributed to the denser channel arrangement, making the distribution of methanol through the anode more uniform and ensuring a fast MOR rate. Furthermore, in the fuel availability test, a 3.5 h running time was achieved under a current density of 25 mA·cm^{-2}. The post-test investigation indicated that some reinforcements on the BP surface would be required for improving the long-term operation performance. Santiago et al. [151] published a study concerning the selection of thermoplastic polymers, for potential use as BPs in DMFC applications, due to their low density and cost. Additionally, thermoplastic polymers can be used in three-dimensional (3D) printing techniques for the manufacture of BPs prototypes, with the advantage of being easily recyclable. Therefore, their use in BPs would drastically reduce the environmental impact of the DMFC life cycle, as well as enhance commercialization. Santiago et al. [151] applied four multicriteria decision-making (MCDM) methods, in order to carry out a reliable selection among seven thermoplastic materials. Additionally, long-term experiments with these polymers were carried out in a simulated environment, which reproduced the conditions inside the DMFCs, in order to collect reliable data on the behavior of the materials during the selection process. By applying such methods, the researchers found that acrylonitrile butadiene styrene (ABS) was the preferred material for stationary applications, in which the cost, degradation rate, and dimensional stability were the dominant criteria, whereas density, degradation rate, and dimensional stability were the key factors for portable devices. By contrast, polycarbonate (PC) was the most appropriate material for DMFCs on board unmanned aerial vehicles (UAVs), where, in addition to density and dimensional stability, solution absorption is also relevant. Hence, the authors concluded that their methodology allowed a reliable choice of the most suitable thermoplastic polymers for use in BPs for DMFC applications.

Table 2. Best performance of PS-DMFC devices (single or stack) and principal conditions.

Type	[MeOH]/M	Membrane	Anode	Cathode	Operating T	OCV (mV)c	Max. P ($mW \cdot cm^{-2}$)	Refs.
Single-Button	1	Nafion® 117	4 ($mg \cdot cm^{-2}$) PtRu/C, 3DG	2.0 ($mg \cdot cm^{-2}$) Pt/C, CP	RT (n.d.)	~500 *	4.78	[92]
Single	4	Nafion® 117	4 ($mg \cdot cm^{-2}$) Pt-Ru Black	2.0 ($mg \cdot cm^{-2}$) Pt Black	RT (n.d.)	~650 *	5.93	[94]
Single-CFSF	4	Nafion® 117	4 ($mg \cdot cm^{-2}$) Pt-Ru, CP	2.0 ($mg \cdot cm^{-2}$) Pt/C, CP (w/MPL)	26 °C	~500 *	18.4	[97]
Single-CNW	2	Nafion® 117	4 ($mg \cdot cm^{-2}$) Pt-Ru, CP	2.0 ($mg \cdot cm^{-2}$) Pt, CP (w/MPL)	25 °C	~780 *	27.53	[99]
Single	2	Nafion® 117	4 ($mg \cdot cm^{-2}$) Pt-Ru, CP	2.0 ($mg \cdot cm^{-2}$) Pt, CP (w/MPL)	25 °C	~750 *	17.93	[99]
Single-oNovel	4	Nafion® 117	(Commercial electrode)	(Commercial electrode)	23 °C	~550 *	~18.5 *	[100]
Single-eNovel	4	Nafion® 117	(Commercial electrode)	(Commercial electrode)	23 °C	~550 *	~17.0 *	[100]
Single-oCon	4	Nafion® 117	(Commercial electrode)	(Commercial electrode)	23 °C	~570 *	~17.5 *	[100]
Single-oCPNovel	14	Nafion® 117	(Commercial electrode)	(Commercial electrode)	23 °C	(n.d.)	13.2	[100]
Single- rGO	4	Nafion® 117	(Commercial electrode)	2.0 ($mg \cdot cm^{-2}$) Pt/C, SSFF-rGO	25 °C	~600 *	25.04	[102]
Single	2	Nafion® 117	(Commercial electrode)	2.0 ($mg \cdot cm^{-2}$) Pt/C, CP	25 °C	~580 *	20.54	[102]
Single-3D GF	3	Nafion® 117	4 ($mg \cdot cm^{-2}$) Pt-Ru, CP	2.0 ($mg \cdot cm^{-2}$) Pt/C, CP (w/3D GF)	25 °C	~750 *	27.6	[103]
Single	3	Nafion® 117	4 ($mg \cdot cm^{-2}$) Pt-Ru, CP	2.0 ($mg \cdot cm^{-2}$) Pt/C, CP	25 °C	~650 *	19.4	[103]
Single	7	Nafion® 117	3 ($mg \cdot cm^{-2}$) Pt-Ru, CC (w/MPL)	1.3 ($mg \cdot cm^{-2}$) Pt, CC	20 °C	~650	5.23	[105]
Single	2	Nafion® 117	3 ($mg \cdot cm^{-2}$) Pt-Ru, CC (w/MPL)	1.3 ($mg \cdot cm^{-2}$) Pt, CC	20 °C	~650 *	3.14	[106]
Single	5	Nafion® 117	3 ($mg \cdot cm^{-2}$) Pt-Ru, CC (w/MPL)	1.3 ($mg \cdot cm^{-2}$) Pt, CC	20 °C	~720 *	3.00	[107,108]
Single	4	Nafion® 115	4 ($mg \cdot cm^{-2}$) Pt-Ru/C, CC (w/MPL)	2 ($mg \cdot cm^{-2}$) Pt/C, CC (w/MPL)	25–27 °C	~550 *	5.865	[109]
Single	2	Nafion® 117	4 ($mg \cdot cm^{-2}$) Pt-Ru Black	4 ($mg \cdot cm^{-2}$) Pt Black	RT (n.d.)	~464 *	12.05	[110]
Single-A	3	Nafion® 117	(n.d.) ($mg \cdot cm^{-2}$) Pt-Ru	(n.d.) ($mg \cdot cm^{-2}$) Pt	RT (n.d.)	~600 *	18.3	[111]
Single-B	4	Nafion® 117	(n.d.) ($mg \cdot cm^{-2}$) Pt-Ru	(n.d.) ($mg \cdot cm^{-2}$) Pt	RT (n.d.)	~570 *	15.4	[111]
Single	10	Nafion® 117	4 ($mg \cdot cm^{-2}$) Pt-Ru/C, CC	4 ($mg \cdot cm^{-2}$) Pt/C, CC	RT (n.d.)	602	26.614	[112]
Single-SA	2	PEM (n.d.)	(n.d.), CC	(n.d.), CC	RT (n.d.)	650	16.56	[113]
Single	2	PEM (n.d.)	(n.d.), CC	(n.d.), CC	RT (n.d.)	650	15.37	[113]
Single-SCS	2	Nafion® 117	(n.d.) ($mg \cdot cm^{-2}$) Pt-Ru	(n.d.) ($mg \cdot cm^{-2}$) Pt	60 °C	~750 *	52.16	[114]
Single	2	Nafion® 117	(n.d.) ($mg \cdot cm^{-2}$) Pt-Ru	(n.d.) ($mg \cdot cm^{-2}$) Pt	20 °C	~750 *	20.8	[114]
Single	4	Nafion® 117	2 ($mg \cdot cm^{-2}$) Pt-Ru, CP	4 ($mg \cdot cm^{-2}$) Pt, CP	25 °C	(n.d.)	14.91	[116]
Single-MEMS/T	7	Nafion® 117	3.5 ($mg \cdot cm^{-2}$) Pt-Ru, CP	3.5 ($mg \cdot cm^{-2}$) Pt, CP	25 °C	~700 *	6.64	[118]
Single-MEMS/R	7	Nafion® 117	3.5 ($mg \cdot cm^{-2}$) Pt-Ru, CP	3.5 ($mg \cdot cm^{-2}$) Pt, CP	25 °C	~575 *	3.90	[118]
Single-MEMS/Si	2	Nafion® 117	(n.d.) ($mg \cdot cm^{-2}$) Pt/CNTs, HLS	(n.d.) ($mg \cdot cm^{-2}$) Pt/CNTs, THS	RT (n.d.)	501	0.186	[119]
Single-MEMS/CP	2	Nafion® 117	(n.d.) ($mg \cdot cm^{-2}$) Pt, CP	(n.d.) ($mg \cdot cm^{-2}$) Pt, CP	RT (n.d.)	265	0.042	[119]
Single-MEA1	4	Nafion® 117	4 ($mg \cdot cm^{-2}$) Pt-Ru/C, CC	2 ($mg \cdot cm^{-2}$) Pt, CC	RT (n.d.)	~530 *	~2.50 *	[126]

Table 2. *Cont.*

Type	[MeOH]/M	Membrane	Anode	Cathode	Operating T	OCV (mV)c	Max. P ($mW \cdot cm^{-2}$)	Refs.
Single-MEA2	4	Nafion® 117	4 ($mg \cdot cm^{-2}$) (Pt-Ru/C + Pt-Ru/black), CC	2 ($mg \cdot cm^{-2}$) Pt, CC	RT (n.d.)	~570 *	3.36	[126]
Single-MEA2	3	Nafion® 117	4 ($mg \cdot cm^{-2}$) (Pt-Ru/C + Pt-Ru/black), CC	2 ($mg \cdot cm^{-2}$) Pt, CC	RT (n.d.)	~580 *	3.872	[126]
Single-MEA2/LE	5	Nafion® 117	4 ($mg \cdot cm^{-2}$) (Pt-Ru/C + Pt-Ru/black), CC	2 ($mg \cdot cm^{-2}$) Pt, CC	RT (n.d.)	~650 *	~5.25 *	[126]
Single-SPUT.	4	Nafion® 117	1.0 ($mg \cdot cm^{-2}$) $Ru_{SPUTTERED}$-Pt/C, CP	1.0 ($mg \cdot cm^{-2}$) Pt/C, CP	RT (n.d.)	417	3.28	[132]
Single	4	Nafion® 117	1.0 ($mg \cdot cm^{-2}$) Pt/C, CP	1.0 ($mg \cdot cm^{-2}$) Pt/C, CP	RT (n.d.)	520	3.01	[132]
Single-NCNT	3	Nafion® 117	4 ($mg \cdot cm^{-2}$) Pt-Ru/NCNT, CP (w/MPL)	2.0 ($mg \cdot cm^{-2}$) Pt/NCNT, CP (w/MPL)	RT (n.d.)	730	26.1	[134]
Single-TiO_2-CNF	3	Nafion® 117	2 ($mg \cdot cm^{-2}$) PtRu/TiO_2-CNF, CC	2 ($mg \cdot cm^{-2}$) Pt/C, CC	RT (n.d.)	~500 *	3.8	[135,136]
Single	3	Nafion® 117	2 ($mg \cdot cm^{-2}$) PtRu/C, CC	2 ($mg \cdot cm^{-2}$) Pt/C, CC	RT (n.d.)	~450 *	2.2	[135,136]
Single	3	Nafion® 117	8 ($mg \cdot cm^{-2}$) Pt-Ru Black/CB, CC	8 ($mg \cdot cm^{-2}$) Pt Black, CC	RT (n.d.)	~680 *	11.10	[137]
Single	5	Nafion® 117	8 ($mg \cdot cm^{-2}$) Pt-Ru Black/CB, CC	8 ($mg \cdot cm^{-2}$) Pt Black, CC	RT (n.d.)	~650 *	10.8	[137]
Single-CNF	3	Nafion® 117	8 ($mg \cdot cm^{-2}$) Pt-Ru Black/CNF, CC	8 ($mg \cdot cm^{-2}$) Pt Black, CC	RT (n.d.)	~620 *	13.17	[137]
Single-CNF	5	Nafion® 117	8 ($mg \cdot cm^{-2}$) Pt-Ru Black/CNF, CC	8 ($mg \cdot cm^{-2}$) Pt Black, CC	RT (n.d.)	480	9.98	[137]
Single-TiO_2	3	Nafion® 117	8 ($mg \cdot cm^{-2}$) Pt-Ru Black/TiO_2, CC	8 ($mg \cdot cm^{-2}$) Pt Black, CC	RT (n.d.)	~500 *	7.44	[137]
Single-TiO_2	5	Nafion® 117	8 ($mg \cdot cm^{-2}$) Pt-Ru Black/TiO_2, CC	8 ($mg \cdot cm^{-2}$) Pt Black, CC	RT (n.d.)	~600 *	7.11	[137]
Single-TiO_2-CB	3	Nafion® 117	8 ($mg \cdot cm^{-2}$) Pt-Ru Black/TiO_2-CB, CC	8 ($mg \cdot cm^{-2}$) Pt Black, CC	RT (n.d.)	~660 *	11.47	[137]
Single-TiO_2-CB	5	Nafion® 117	8 ($mg \cdot cm^{-2}$) Pt-Ru Black/TiO_2-CB, CC	8 ($mg \cdot cm^{-2}$) Pt Black, CC	RT (n.d.)	630	10.10	[137]
Single-TiO_2-CNF	3	Nafion® 117	8 ($mg \cdot cm^{-2}$) Pt-Ru Black/TiO_2-CNF, CC	8 ($mg \cdot cm^{-2}$) Pt Black, CC	RT (n.d.)	~640 *	10.73	[137]
Single-TiO_2-CNF	5	Nafion® 117	8 ($mg \cdot cm^{-2}$) Pt-Ru Black/TiO_2-CNF, CC	8 ($mg \cdot cm^{-2}$) Pt Black, CC	RT (n.d.)	560	10.42	[137]
Single-CNC	2	Nafion® 117	2 ($mg \cdot cm^{-2}$) PtRu/CNC, CC	2 ($mg \cdot cm^{-2}$) Pt/C, CC	RT (n.d.)	~500 *	3.35	[138]

Table 2. *Cont.*

Type	[MeOH]/M	Membrane	Anode	Cathode	Operating T	OCV (mV)c	Max. P ($mW \cdot cm^{-2}$)	Refs.
Single	2	Nafion® 117	2 ($mg \cdot cm^{-2}$) PtRu/C, CC	2 ($mg \cdot cm^{-2}$) Pt/C, CC	RT (n.d.)	~430 *	1.95	[138]
Single	(5% and KOH 10%)	A 006 Tokuyama	2.0 ($mg \cdot cm^{-2}$) Pt/C, CP	2.0 ($mg \cdot cm^{-2}$) Pt/C, CP	RT (n.d.)	~450 *	~1.2 *	[139]
Single-NFKP	(5% and KOH 10%)	A 006 Tokuyama	2.0 ($mg \cdot cm^{-2}$) Pt/C, CP	2.0 ($mg \cdot cm^{-2}$) NiCo/NFKP, CP	RT (n.d.)	~500 *	~0.9 *	[139]
Single-NRGO	3 and KOH 1 M	A 006 Tokuyama	2 ($mg \cdot cm^{-2}$) Pt/C, CP	5 ($mg \cdot cm^{-2}$) NRGO, CP	RT (n.d.)	681	4.332	[141]
Single	1.5 and KOH 1 M	A 006 Tokuyama	2 ($mg \cdot cm^{-2}$) Pt/C, CP	5 ($mg \cdot cm^{-2}$) Pt/C, CP	RT (n.d.)	645	1.818	[141]
Single	2	Nafion® 117	4 ($mg \cdot cm^{-2}$) Pt/Ru/Ti	2 ($mg \cdot cm^{-2}$) Pt/C, CP (w/MPL)	RT (n.d.)	496	2.7	[145]
Stack (2 cells)	2	Nafion® 117	4 ($mg \cdot cm^{-2}$) Pt/Ru/Ti	2 ($mg \cdot cm^{-2}$) Pt/C, CP (w/MPL)	RT (n.d.)	1000	2.5	[145]
Stack (6 cells)	2	Nafion® 117	4 ($mg \cdot cm^{-2}$) Pt/Ru/Ti	2 ($mg \cdot cm^{-2}$) Pt/C, CP (w/MPL)	RT (n.d.)	2900	1.7	[145]
Stack (4 cells) BP	3	PEM (n.d.)	4 ($mg \cdot cm^{-2}$) (n.d.), CP	2 ($mg \cdot cm^{-2}$) (n.d.), CP	20 °C	1260	18.7	[147]
Stack (3 cells) MPC16	6	Nafion® 117	1.0 ($mg \cdot cm^{-2}$) Pt/Ru/C, CP	1.0 ($mg \cdot cm^{-2}$) Pt/C, CP	80 °C	1340	25.24	[148]
Single-MPC16	6	Nafion® 117	1.0 ($mg \cdot cm^{-2}$) Pt/Ru/C, CP	1.0 ($mg \cdot cm^{-2}$) Pt/C, CP	85 °C	452	7.91	[148]
Single-MPC9	4	Nafion® 117	1.0 ($mg \cdot cm^{-2}$) Pt/Ru/C, CP	1.0 ($mg \cdot cm^{-2}$) Pt/C, CP	85 °C	480	5.17	[148]

(RT = room temperature; n.d. = not disclosed; * value estimated from the plot; w/ = with; CP/CC = carbon paper/carbon cloth).

3. Other Alcohols and Alternative Oxidants

While the practicability of fuel cell technology for portable power applications has been demonstrated with PS-DMFCs, the issue of which alcohol and alternative oxidants can be used to operate these devices is still very much open. The environmental impacts of these kind of devices can be found in a detailed review by Abdelkareem et al. [152]. Moreover, a systematic assessment of the fuel safety and health aspects for DAFCs was also reported by Elsaid et al. [153], calling attention to these issues and their strong impact on the safer operation of the devices, for portable and mobile applications. Thus, there is a clear concern from the research community when tackling these matters, not only in terms of the diversity of materials tested but also how operational conditions can be tuned in order to enhance the performance of the devices and flexibility of applications, in a safer and more sustainable manner. Some examples, supported by the published papers in the field, which strive to advance fuel cell technology for R&D and further commercialization, are discussed in this section.

3.1. Ethanol

As already mentioned, ethanol is considered as the most plausible candidate to replace methanol in DAFCs [154]. Shrivastava et al. [24] studied the parameters that significantly affect the fuel cell performance by developing and using a PS-DEFC with 25 cm^2 active area and a Nafion® 115 membrane as electrolyte. This device showed a performance improvement with an increase in the ethanol feed concentration, until it reached a maximum, after which a decrease in performance was observed with an increase in the ethanol concentration. A similar trend in the cell performance was observed with an increase in the ambient temperature and bolt torque. The maximum cell performance of 7 N·m was observed with a 4 M ethanol feed concentration, at 60 °C (Table 3). Furthermore, they verified that the device performance was improved (by 8.5% to 13%) when operated in the horizontal orientation compared to the vertical one, due to the fact that the horizontal orientation provided better CO_2 removal, as well as better cathode water removal. Therefore, this study reinforced that an improvement in PS-DEFC performance can be obtained by carefully selecting the working parameters of the cell.

Moreover, similar to what was presented for PS-DMFCs, for PS-DEFCs, it is also possible to find examples of sustainable biomass-supported alternative approaches. As stated earlier, the alkaline medium is ideal since Pt-based catalysts can be readily replaced by non-noble metals (and their alloys). Moreover, unlike the MOR, the EOR in alkaline solution is more feasible with palladium (Pd) than Pt-based catalysts, as supported by Fashedemi et al. [155]. This work covered not only passive but also active DAFCs, including methanol- and ethanol-fed devices and the new core–shell Pd-based electrocatalysts developed by the authors. These new catalysts were prepared using cost-effective transition metals (Fe, Co) and Pd as the shell (FeCo@Fe@Pd) through a microwave-assisted solvothermal method, which induced top-down nanostructuring. The as-prepared nanoelectrocatalysts were also supported on carboxylated multiwalled carbon nanotubes (CNT-OH) as substrates, following the previous experiences of the researchers [156–159]. Then, the new catalysts were used in the preparation of anodes supported on a 5.13 cm^2 nickel foam plate. These, together with a commercial Tokuyama A-201 AEM and cathodes containing a Fe–Co/C electrocatalyst on carbon cloth, constituted the MEAs tested in a homemade device, run with a 10% alcohol and 2 M KOH fuel solution in ambient air. In this way, the researchers were able to compare the cell performance when using the core–shell nanoelectrocatalyst (FeCo@Fe@Pd/CNT-OH) and its monometallic Pd counterpart (Pd/CNT-OH). Outstanding performance of the core–shell FeCo@Fe@Pd catalyst was observed compared to the single Pd metal on the same substrates, even at moderate temperatures (15 to 18 °C). Specifically, fourfold and threefold increases in the PD value were observed for the DEFC and DMFC, respectively (Table 3). In addition, taking advantage of the information gathered from the galvanostatic curves obtained when running both devices at 102 mA, the researchers estimated the faradaic efficiency for both catalysts,

which was calculated as the ratio of the actual and theoretical discharging capacity. The values obtained indicated that the (FeCo@Fe@Pd/CNT-OH) nanoelectrocatalyst had 50% better efficiency than its Pd counterpart (Table 4).

These experimental findings were further corroborated by density functional theory (DFT) calculations, which were performed in order to further characterize the surface activity of both nanocatalysts toward the AOR. The simulations revealed an increased electronic involvement in the partially filled d-orbitals of the FeCo@Fe@Pd/CNT-OH core–shell catalysts in contrast to those of the p-orbitals of Pd/CNT-OH, thus resulting in an improved conductivity of the Pd surface of the core–shell nanocatalyst and promoting its catalytic properties in both alkaline PS-DAFCs. These results clearly demonstrated the attractiveness of alkaline PS-DEFCs as a more renewable and clean energy power source devices. A similar approach can be found in the work from Fuku et al. [160], where the synthesis of a novel bioinspired metal oxide support for a Pd-based catalyst and its application in AEM-PS-DEFC were reported. The goal was to improve the activity, efficiency, and selectivity of the Pd catalysts, consequently improving the device performance. Thus, according to the researchers, Pd NPs were supported on NiO/C, through a green facile one-step process, using pomegranate peel extracts as the reducing agent. Performance tests were carried out using an alkaline passive fuel cell consisting of an AEM (N15 A201) MEA with an active area of 2.25 cm^2, provided by Tokuyama Corporation, and commercial catalysts in the anode and cathode, namely, commercial-Pd/C (anode) and FeCo/C (cathode), as well as "in-house" Pd-NiO/C (anode) and Pd/C(commercial-cathode) electrocatalysts. Enhanced fuel cell performances relative to the commercial Pd/C catalyst were obtained under passive conditions using 1 M ethanol in 1 M KOH, with a current density and PD of 66 $mA \cdot cm^{-2}$ and 26 $mW \cdot cm^{-2}$, respectively. These results showed an important increase in the fuel efficiency due to the inclusion of NiO/C-support catalysts. Hence, this work encouraged application of the green protocol for synthesis of bioinspired electrocatalysts to a wide range of materials, especially in PS-DAFC applications for smart electronic devices and manufacturing processes.

Other alternative approaches can be found in different studies that investigated the effect of using MEAs fabricated with PGM-free catalysts on the performance of AEM-PS-DEFCs. Osmieri et al. [65] presented a study concerning the synthesis and full characterization of an Fe−Co−N−C electrocatalyst for the ORR, employing a sacrificial method, where pyrrole was used as a unique and inexpensive precursor for N-doped carbonaceous materials. As aforementioned, conducting polymers such as polyaniline and polypyrrole can be conveniently employed in the preparation of PGM-free ORR catalysts. In particular, polypyrrole has received much attention as a catalyst support and electrode material due to its peculiar metallic/semiconductor properties, excellent conductivity, facile synthesis, and remarkable environmental stability [161]. Thus, the new Fe–Co–N–C PGM-free catalyst was used as a CCL together with Pd on CB as the ACL and an AEM (Tokuyama A-201) to construct an alkaline MEA with an active area of 1 cm^2. This MEA was tested in a PS-DEFC fed with a mixture of 2 M EtOH and 2 M KOH, at room temperature. The researchers obtained a high OCV value despite alcohol crossover, showing that the cell potential was not much affected, since the PGM-free catalyst was very active toward the ORR and had no catalytic activity toward ethanol oxidation. A maximum PD of 28 $mW \cdot cm^{-2}$ was achieved with the proposed catalyst. Another study concerning the cell performance and ethanol crossover, this time in an acidic PS-DEFC stack, was reported by Ekdharmasuit [162]. In this case, to reach the voltage requirement needed for most electronics, a dual-cell stack with a single ethanol tank was designed and tested. This also had the advantage of reducing the weight and volume of the device for practical applications. The MEA was made by applying thin layers of an "in-house" (Pt–Sn/C) anode and a commercial Pt/C cathode on each side of a treated Nafion® 115 membrane and pressing them together. The dual-cell stack was fabricated by gathering two fuel reservoirs in one or two end plates and two single cells (Figure 16).

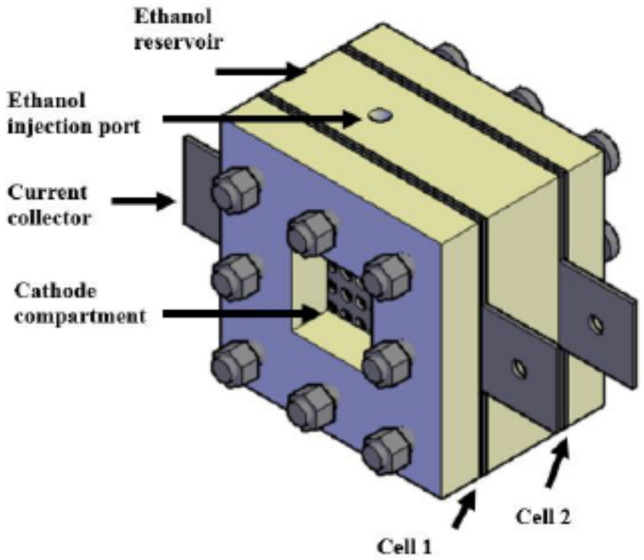

Figure 16. Schematic of assembled dual-cell PS-DEFC stack. Reproduced from [162] with permission from EDP Sciences 2020.

The cell performance and alcohol crossover rate were determined at different ethanol concentrations (1 to 3 M). The stability or degradation of the stack performance was assessed using a long-term steady voltage discharging measurement (conducted under a constant voltage of 1 V for 5 h) and EIS. It was reported that, before the stability or degradation test, the optimum ethanol concentration was 2 M, achieving a maximum PD of 1.516 $mW \cdot cm^{-2}$. However, since the alcohol crossover increased with the ethanol concentration, a concentration in excess of 2 M led to a detrimental impact on the OCV and cell performance. Nevertheless, after stability or degradation testing, the best ethanol feed concentration was changed to 3 M (with a maximum PD of 1.319 $mW \cdot cm^{-2}$), and EIS results showed that the cell resistance was apparently reduced. These results were justified, due to the difference in current density discharged during long-term operation and the fact that the mass transport of both liquid fuel and air reached an equilibrium during the long-term operation. In summary, the dual-cell PS-DEFC stack gave the best results with a 2 M ethanol solution, but the stability was hampered by long-term constant voltage discharge. Therefore, further improvements for practical applications are mandatory.

3.2. Other Alcohols

Following the pioneering study published in 2007 by Gojković et al. [163], in which mixtures of methanol and 2-propanol were used as a potential fuel for DAFCs, Munjewar et al. [164] investigated the effect of adding small concentrations of 2-propanol on the PS-DMFC performance using a traditional PtRu/C catalyst. Therefore, different alcohol concentration ratios (ACR) were used while keeping the methanol concentration constant and varying the 2-propanol concentration in the solution. As elucidated by the researchers, the tests were carried out not to obtain the maximum PD, but to discuss and analyze the performance of PS-DAFCs, which increased with the addition of a small amount of 2-propanol. The performance increased by 63% with an ACR of 1:0.5 for a 4 M methanol solution, reaching the maximum power output of 3.707 $mWcm^{-2}$. It was also observed that a further increase in 2-propanol concentration led to the generation of a higher amount of CO_2, which deteriorated the fuel cell performance. It was also pointed out that an increase in the alcohol concentration in the tank led to an increase in the alcohol crossover, an increase in the amount of water at the cathode side, and an obstruction of the oxygen supply. Moreover, it was also found that the introduction of 2-propanol in methanol improved the exothermic reaction rate, resulting in a higher cell temperature (~10 °C increase for the higher ACR). Hence, due to the higher temperature of the cell, the

AOR and ORR were kinetically enhanced, improving cell performance. All these findings highlight the potential of using a mixture of methanol and 2-propanol as fuel to improve the PS-DAFC performance.

Another possibility is to use other alcohols, such as glycerol (G) ($CH_2OH–CHOH–CH_2OH$ and ethylene glycol (EG) ($(CH_2OH)_2$), also called ethane-1,2-diol, the simplest member of the glycol family of organic compounds. These are the most investigated polyhydric alcohols for alkaline DAFCs, as their oxidation, although incomplete, is considered to be better performed than in acid medium [77]. These alcohols have a relatively high theoretical energy density, 5.2 $kW{\cdot}h{\cdot}kg^{-1}$ and 5.0 $kW{\cdot}h{\cdot}kg^{-1}$ for ethylene glycol and glycerol, respectively. Furthermore, they are biomass-derived; glycerol is the primary product in biodiesel production through transesterification of plant oils and animal fat, while ethylene glycol is obtained from oxidation of ethylene. Thus, both alcohols can be produced in renewable and environmentally friendly ways [158]. For more information regarding selective electrooxidation of glycerol into value-added chemicals, the short overview compiled by Coutanceau et al. [165] is recommended, as well as the review from Antolini [166] regarding the glycerol electrooxidation reaction (GOR) in alkaline media and alkaline DGFCs. Further R&I studies regarding electrocatalyst development toward the GOR can be found in the review paper presented by Othman et al. [167]. It should be pointed out that Pt- and Pd-based catalysts have been employed in DGFCs. Pt-based catalysts lead to better kinetics but suffer from CO poisoning, while Pd-based alloy nanostructures show enhanced electrocatalytic activities in alkaline media. Moreover, Pd–Au bimetallic catalysts are considered a good combination, resulting in extremely active NP catalysts toward the GOR [158,165–167]. Thus, Yahya et al. [21,168] reported the study of a nanostructured Pd–Au-based electrocatalyst in a PS-DGFC. Their aim was to synthesize and characterize the catalytic activity of Pd1Au1 supported by vapor-grown carbon nanofiber (VGCNF) anode catalyst. The new catalyst was prepared via a chemical reduction method, such that the presence of mesoporous VGCNF as a support enabled minimization of the Pd–Au loading. Therefore, the high electrocatalytic activity of Pd_1Au_1/VGCNF could be related to the high dispersion of the metal NPs and to the intrinsic properties of the VGCNF. To test the materials, different MEAs (with an active area of 2.0 × 2.0 cm^2) consisting of two single-sided electrodes and an AEM membrane (FAA-3 membrane, FumaTech) were assembled. The new materials (Au/VGCNF, Pd/VGCNF, and Pd_1Au_1/VGCNF) were applied as the ACL, while Pt/C was used as the CCL. The performance of the MEAs was evaluated through polarization curves and EIS measurements. The maximum PD of the PS-DGFC was 3.9 $mW{\cdot}cm^{-2}$, for the fuel mixture of 2 M glycerol and 5 M NaOH. The EIS data indicated that Pd_1Au_1/VGCNF had a smaller kinetic resistance in comparison with the other two electrocatalysts. Furthermore, in terms of electrocatalyst prices, the price for Pd_1Au_1/VGCNF is 0.26 USD/mg cheaper than the price for commercial Pd black, which is 0.41 USD/mg. As the power output of the device was affected by GDL morphological defects and AEM stabilities, in addition to MEA manufacturing, further investigations of the alkaline fuel cells are needed to address this problem, since it is vital for the long-term operation of PS-DGFCs. In line with this necessity, Olivares-Ramírez et al. [169] reported a study focused on the evaluation of the energy generated in AEM-based PS-DGFCs using glycerol from different sources, namely, high-purity glycerol (HPG), saponification process-derived glycerol (SPDG), crude glycerol from sunflower oil biodiesel (CGSOB), and crude glycerol from cooking oil biodiesel (CGCOB). The device used was assembled by sandwiching the MEA between two epoxy-based SU-8 CCs and placing them between two PMMA pieces. A square window of 1.1 × 1.1 mm^2 was milled through the acrylic pieces to allow the addition of reactants. The design of this device was very compact (classified as a micro fuel cell), and the active area of the MEA was 0.25 cm^2 (Figure 17).

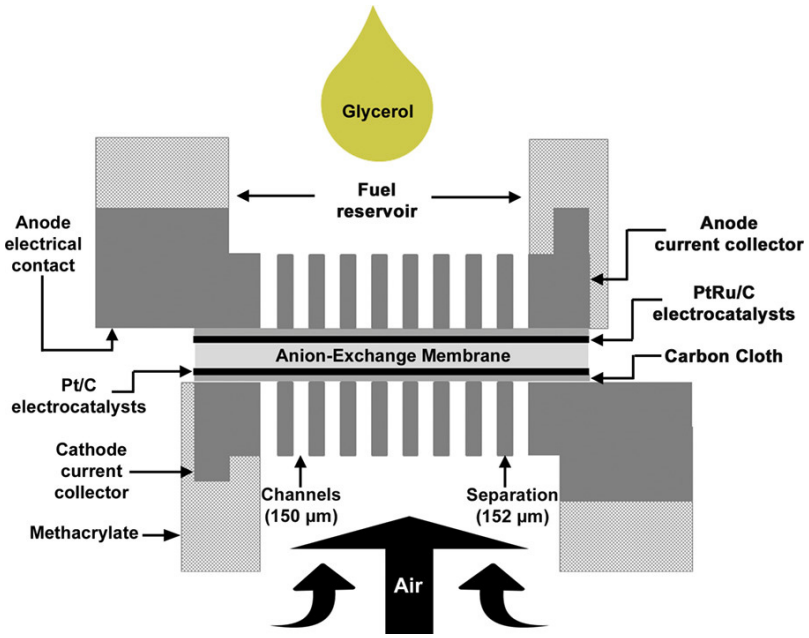

Figure 17. Schematic drawing showing the cross-section of the assembled AEM-based PS-DGlyFC. Reproduced from [169] with permission from John Wiley and Sons 2019.

Thus, the AEM-PS-DGFC tests only needed 15 µL of 0.1 M glycerol in 0.3 M KOH, introduced at the anode reservoir, which was facing upward. This solution permeated through the microchannels of the ACC to reach the ACL. The cathode, which was facing downward, was filled with oxygen from ambient air by natural convection. Regarding the performance of the fuel cell, it was observed that the OCV was 0.6 V for all glycerol samples, while the maximum PD was 1.008, 0.932, 0.871, and 0.865 $mW \cdot cm^{-2}$ for HPG, SPDG, CGSOB, and CGCOB, respectively. Additionally, the current density obtained using HPG (5.389 $mA \cdot cm^{-2}$) was higher than that when using SPDG, CGSOB, and CGCOB (4.934, 4.729, and 4.67 $mA \cdot cm^{-2}$, respectively). The researchers also evaluated the energy price and demonstrated that the energy cost generated through HPG was approximately 16.5 times the energy cost of SPDG and 130 times the energy cost of CGCOB. It was concluded that, although a decrease of 14.19% in the power density was observed when CGCOB was employed, its lower cost favors its use as a fuel in AEM-based PS-DGFCs. This work highlighted the potential of a compact power source that can benefit from the advantages associated with crude glycerol, such as high chemical density, availability, and low cost.

3.3. Alternative Oxidants

In view of the application of fuel cells in air-free environments, such as outer space and underwater, the use of hydrogen peroxide (H_2O_2) acting as an oxidant to replace air or pure oxygen has been extensively investigated. Thus, hybrid or alkaline–acid (AA) fuel cells (also known as split pH fuel cells) running with ethylene glycol (in alkaline solution) as fuel and H_2O_2 (in acid solution) as oxidant were proposed by Pan et al. in active [170,171] and passive [172] modes. This device takes advantage of the pH split between the fuel and oxidant feed (~0 and ~14 at the cathode and anode, respectively), which increases the theoretical cell voltage and the oxidation rate of the fuel, leading to a higher fuel cell performance. This work was complemented by a one-dimensional mathematical model considering the ethylene glycol molecules and hydroxyl ions at the reaction sites, where the mass/charge transport and electrochemical reactions showed good agreement with the experimental data [173]. A scheme of the working principle of the AA-PS-DEGFC is shown in Figure 18a. The MEA with an active area of 2.0 × 2.0 cm^2, consisted of a Pd-based anode catalyst, a cation-exchange membrane (Nafion®-pretreated to assure the transport of potassium ions from the anode to the cathode, completing the internal ionic circuit), and an

Au-based cathode catalyst. An end plate, a heating plate, and a CC were added to both sides of the MEA (Figure 18b).

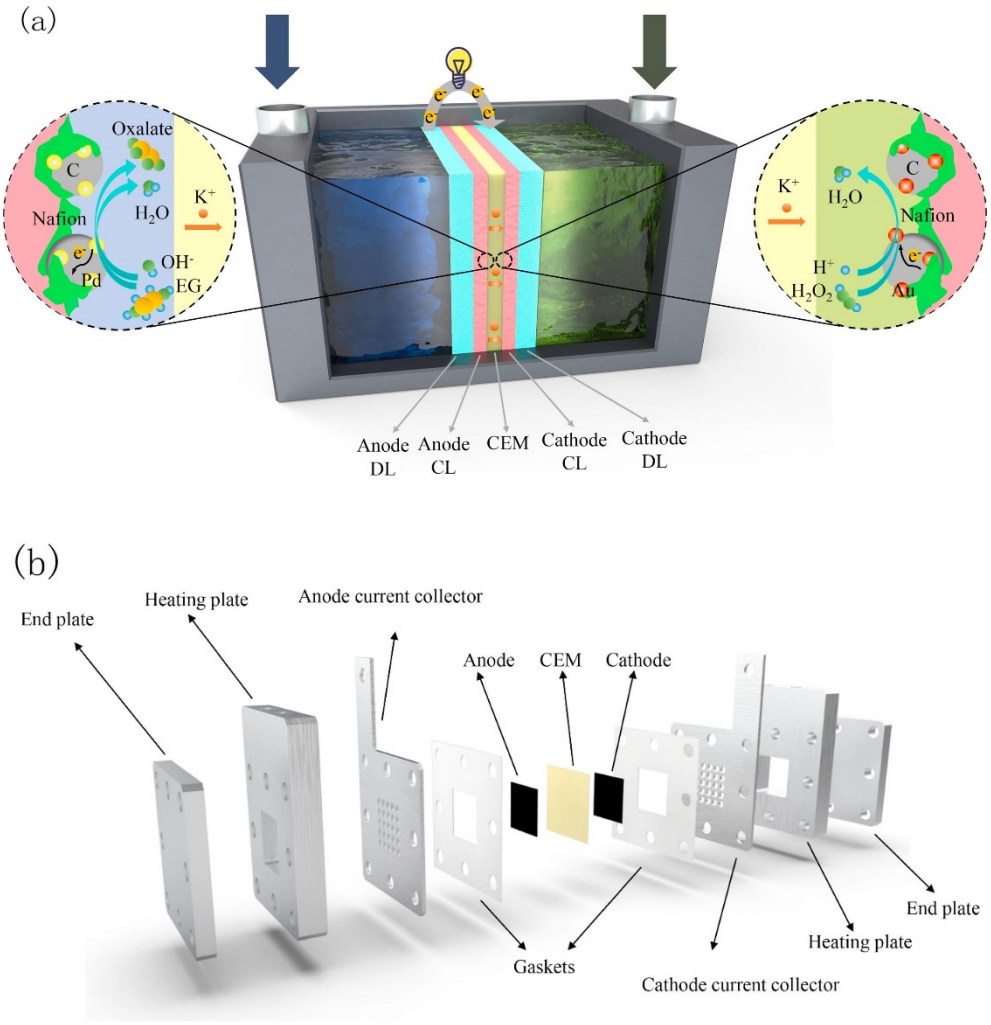

Figure 18. Schematic of AA-based PS-DEGFC: (**a**) working principle; (**b**) exploded view of the structure. Reproduced from [172] with permission from Elsevier 2019.

As the heating plates also served as solution reservoirs, two holes were drilled on the top surface of the heating plate. One was designed for injecting the anolyte or catholyte (electrolyte solution on the anode or cathode side, respectively), while the other was designed for placing the heating rod. Different operating conditions were tested to investigate their effects on the AA-PS-DEGFC performance. It was found that, although a thicker membrane reduced the alcohol crossover problem, a thinner one showed a significant reduction in the ohmic loss, resulting in a higher cell performance. Therefore, the performance of this fuel cell under the optimal operating conditions exhibited an OCV of 1.58 V (the theoretical voltage was 2.47 V) and a maximum PD of 65.8 $mW \cdot cm^{-2}$, with an aqueous anolyte (5.0 M EG and 9.0 M KOH) and catholyte (1.0 M H_2SO_4 and 4.0 M H_2O_2) at an operating temperature of 60 °C. Moreover, the results obtained indicated that the H_2O_2 self-decomposition reaction had a negligible effect on the total heat released over the discharging process, and electrochemical reactions on both the anode and the cathode played a dominant role. This work achieved values that were more than twofold the OCV and more than fivefold the maximum PD obtained using a PS-DEGFC with oxygen as the oxidant, which was mainly due to the simple and faster HPRR when compared to the ORR. Subsequently, motivated by the higher voltage requirements of most electronic devices, the researchers designed, fabricated, and tested an AA-PS-DEGFC stack composed of two

single cells similar to a previous study (unitary active area of 3.0 × 8.0 cm^2) connected in series (Figure 19) [174].

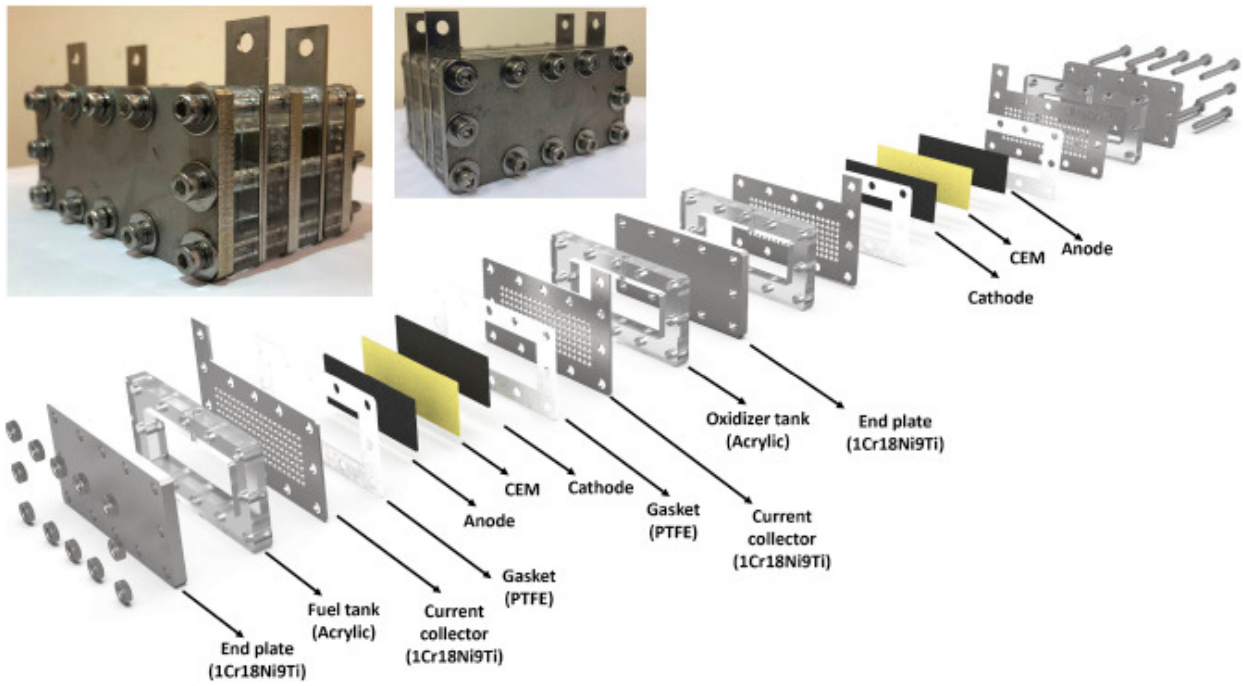

Figure 19. Schematic of the AA-based PS-DEGFC stack. Reproduced from [174] with permission from Elsevier 2019.

By using the optimal reactant-feeding concentrations of 5 M ethylene glycol and 9 M KOH as anolyte and 4 M H_2O_2 and 1.0 M H_2SO_4 as catholyte, an OCV of 3.0 V, a maximum current of 860 mA, and a maximum power of 1178 mW were achieved at room temperature, resulting in a twofold higher PD than the maximum PD (24.5 mW·cm^{-2}) of a passive stack using the same type of fuel, but air as the oxidant (12 mW·cm^{-2}). However, the OCV of the stack (3.0 V) was significantly lower than the theoretical one (4.94 V), due to the fact that H_2O_2 is not stable and can be decomposed to water during the HPRR occurring at the cathode, as well as during oxygen production in the H_2O_2 oxidation reaction (HPOR). This established an internal H_2O_2-based fuel cell and led to the formation of a mixed potential at the cathode, decreasing the expected OCV. This phenomenon was previously recognized and modeled [175]. Additionally, the oxygen produced could have covered the catalyst sites, reducing the electrochemical active surface area, whereby the presence of oxygen in the diffusion layer and CL pores blocked the pathways for the reactant transport, contributing to activation loss and a lower OCV. Nevertheless, the passive stack was applied to power an electric fan, and it was observed that, in ambient conditions, the fan only worked when the air was replaced by H_2O_2 and ethylene glycol was used as fuel, with a total running time of almost 3 h. Similar results were obtained when testing in a mimetic underwater environment, without air supply and using ethylene glycol as fuel, while H_2O_2 was used as the oxidant.

Another study that evaluated the performance of a direct ethylene glycol–hydrogen peroxide fuel cell (DEGHPFC) and direct glycerol–hydrogen peroxide fuel cell (DGHPFC) using pH split was reported by Kepenienė et al. [176]. The main goal was to provide a comprehensive study of the enhanced capability of $AuCeO_2$/C and Au/C catalysts (prepared using a microwave irradiation method) for AOR (methanol, ethanol, ethylene glycol, and glycerol) in alkaline medium. Thus, through electrochemical testing in a standard three-electrode conventional cell, it was shown that $AuCeO_2$/C had enhanced electrocatalytic activity toward the oxidation of the mentioned alcohols compared to Au/C, due to a strong synergistic effect between CeO_2 and Au in the catalyst composition and to

the fact that the $AuCeO_2$/C catalyst was more tolerant to surface poisoning than the Au/C catalyst. Therefore, the use of these catalysts in PS-DAFCs with alcohols that provided the best results (ethylene glycol and glycerol) was also evaluated. The cell had a $AuCeO_2$/C catalyst at the anode and a Pt sheet at the cathode, separated by a Nafion® 117 membrane, and it was filled with the corresponding aqueous electrolyte; the anolyte was composed of an alkaline mixture of 1 M glycerol or ethylene glycol and 4 M NaOH, while the catholyte was composed of 5 M H_2O_2 and 1.5 M HCl. The results showed that the maximum PD increased with temperature in both AA-PS-DAFCs, with DGHPFC presenting a better performance than DEGHPFC. However, as the temperature increased from 25 to 55 °C, the difference between both results decreased from 2.1 times to 1.3. Nevertheless, according to the authors, in general, the PDs obtained in this study were higher than those described in the literature. Another less disruptive approach can be found in the work reported by Lu et al. [177], which studied a passive DMFC using H_2O_2 as the oxidant, i.e., a passive direct methanol–hydrogen peroxide fuel cell (DMHPFC). This fuel cell had a theoretical voltage of 1.76 V (higher than 1.21 V for the traditional DMFC) and could be used in an oxygen-free environment. In this work, Prussian Blue (PB), a non-noble metal catalyst, was used, taking advantage of the excellent HPRR kinetics. This material, $Fe_4[Fe(CN)_6]_3$, is a well-known ancient pigment which can be used as the CCL, since it is unaffected by MOR and is a highly efficient catalyst for HPRR [82]. The PB was combined with a rGO support (through a low-temperature hydrothermal method) to obtain a low-cost rGO-coated nanocube PB composite that was used as the cathode catalyst. In addition, both the PB and the H_2O_2 solution could be kept stable in the acidic environment of the fuel cell. In this study, MEAs (with an effective area of 2 × 2 cm^2) were prepared and used, featuring a Nafion® 115 membrane and PB/rGO and PtRu catalysts at the CCL and ACL, respectively. The PS-DMHPFC tests, using a 6 M methanol solution at the anode and a mixture of 30% H_2O_2 and 2 M H_2SO_4 at the cathode, showed good performance with a maximum PD of 20.5mW·cm^{-2}, even at 85 °C. However, the OCV (0.6 V) was much lower than the theoretical value (1.76 V), due to the mixed potential at the cathode, as explained by the researchers using a mechanistic approach. Moreover, through the polarization and EIS tests performed, it was also demonstrated that the fuel cell had good dynamic and transient responses. Hence, the researchers concluded that, compared with the traditional PS-DMFC, the PS-DMHPFC using the non-noble metal catalyst PB/rGO instead of Pt/C at the cathode greatly reduced the cost while improving performance, due to the electrocatalyst's unique 3D structure. In addition, the device can be used not only in an oxygen-free environment but also in high-temperature conditions, highlighting the prospects of using the DMHPFC to power small devices in the near future.

Table 3. Best performance of PS-DAFCs devices (single or stack), along with the principal fuel and oxidant used.

Type	Fuel/Oxidant	Membrane	Anode	Cathode	Operating T	OCV (mV)	Max. P ($mW \cdot cm^{-2}$)	Refs.
Single	Ethanol 4 M/air	Nafion® 115	4 ($mg \cdot cm^{-2}$) PtRu/C, CC (w/MPL)	2.0 ($mg \cdot cm^{-2}$) Pt/C, CC (w/MPL)	60 °C	~480 *	1.124	[24]
Single	Ethanol 2 M and KOH 2 M/air	A201 Tokuyama	1.3 ($mg \cdot cm^{-2}$) Pd/C, CP	2 ($mg \cdot cm^{-2}$) FeCo/NC, CP	RT (n.d.)	860	28	[65]
Single	Methanol 10% and KOH 2 M/air	A201 Tokuyama	n.d. ($mg \cdot cm^{-2}$) FeCo@Fe@Pd/CNT-OH, NiF	n.d. ($mg \cdot cm^{-2}$) FeCo/C, CC	16 °C	763	21.63	[155]
Single	Methanol 10% and KOH 2 M/air	A201 Tokuyama	n.d. ($mg \cdot cm^{-2}$) Pd/CNT-OH, NiF	n.d. ($mg \cdot cm^{-2}$) FeCo/C, CC	16 °C	716	7.69	[155]
Single	Ethanol 10% and KOH 2 M/air	A201 Tokuyama	n.d. ($mg \cdot cm^{-2}$) FeCo@Fe@Pd/CNT-OH, NiF	n.d. ($mg \cdot cm^{-2}$) FeCo/C, CC	16 °C	741	23.26	[155]
Single	Ethanol 10% and KOH 2 M/air	A201 Tokuyama	n.d. ($mg \cdot cm^{-2}$) Pd/CNT-OH, NiF	n.d. ($mg \cdot cm^{-2}$) FeCo/C, CC	16 °C	611	5.12	[155]
Single	Ethanol 1 M and KOH 1 M/air	A201 Tokuyama	1.5 ($mg \cdot cm^{-2}$) Pd/C, NiF	n.d. ($mg \cdot cm^{-2}$) FeCo/C, CP	25 °C	470	18	[160]
Single	Ethanol 1 M and KOH 1 M/air	A201 Tokuyama	1.5 ($mg \cdot cm^{-2}$) Pd-NiO/C, NiF	n.d. ($mg \cdot cm^{-2}$) PdC/C, CP	25 °C	680	26	[160]
Stack (2 cells)	Ethanol 2 M/air	Nafion® 115	2.0 ($mg \cdot cm^{-2}$) Pt-Sn/C, CC	0.5 ($mg \cdot cm^{-2}$) Pt/C, CC	RT (n.d.)	1243	1.516	[162]
Single	Methanol 4 M and 2-propanol 2 M/air	Nafion® 115	4 ($mg \cdot cm^{-2}$) PtRu/C, CC (w/MPL)	2 ($mg \cdot cm^{-2}$) Pt/C, CC (w/MPL)	25–27 °C	~510 *	3.707	[164]
Single	Glycerol 2 M and NaOH 5 M/air	FAA-3 FumaTech	1.0 ($mg \cdot cm^{-2}$) PdAu/VGCNF, CC (w/MPL)	1.0 ($mg \cdot cm^{-2}$) Pt/C, CC (w/MPL)	25 °C	(n.d.)	3.9	[168]
Single	Glycerol 0.1 M and KOH 0.3 M/air	A201 Tokuyama	1 ($mg \cdot cm^{-2}$) PtRu/C, CC	1 ($mg \cdot cm^{-2}$) Pt/C, CC	RT (n.d.)	~600	1.008	[169]
Single	EG 5 M and KOH 9 M/H_2O_2 4 M and H_2SO_4 1 M	Nafion® 211	1.0 ($mg \cdot cm^{-2}$) Pd/C, CC	2.66 ($mg \cdot cm^{-2}$) Au/C, CC	60 °C	1580	65.8	[172]
Stack (2 cells)	EG 5 M and KOH 9 M/H_2O_2 4 M and H_2SO_4 1 M	Nafion® 211	1.0 ($mg \cdot cm^{-2}$) Pd/C, CC	2.75 ($mg \cdot cm^{-2}$) Au/C, CC	RT (n.d.)	3000	24.5	[174]
Single	Methanol 6 M/H_2O_2 30% and H_2SO_4 2 M	Nafion® 115	3 ($mg \cdot cm^{-2}$) PtRu, CC	6.7 ($mg \cdot cm^{-2}$) PB/rGO, CC	85 °C	600	20.5	[177]
Single	EG 1 M and NaOH 4 M/H_2O_2 5 M and HCl 1.5 M	Nafion® 117	(n.d.) ($mg \cdot cm^{-2}$) $AuCeO_2$/C	(n.d.) ($mg \cdot cm^{-2}$) Pt	60 °C	~800 *	17.30	[176]
Single	Glycerol 1 M and NaOH 4 M/H_2O_2 5 M and HCl 1.5 M	Nafion® 117	(n.d.) ($mg \cdot cm^{-2}$) $AuCeO_2$/C	(n.d.) ($mg \cdot cm^{-2}$) Pt	60 °C	~800 *	22.96	[176]

(RT = room temperature; n.d. = not disclosed; * value estimated from the plot; w/ = with; CP/CC/NiF = carbon paper/carbon cloth/nickel foam).

Table 4. Faradaic efficiency evaluation of the nanocatalysts, adapted from [155].

Catalyst	DAFC Type	Faradaic Efficiency (%)
FeCo@Fe@Pd/CNT-OH	AEM-PS-DMFC	40.48
Pd/CNT-OH	AEM-PS-DMFC	6.92
FeCo@Fe@Pd/CNT-OH	AEM-PS-DEFC	86.75
Pd/CNT-OH	AEM-PS-DEFC	15.65

4. Concluding Remarks

PS-DAFCs are considered promising alternatives to batteries as small power sources (milliwatts to watts), as they benefit from a high power density, long lifetime, and low cost. Thus, they are capable of ensuring an efficient and stable supply of inherent nonpolluting electricity for next-generation portable applications. However, there is still plenty room for research targeting the well-identified technology gaps of reliability and durability, which have hampered the commercialization of PS-DAFC systems and their widespread application. In this review, we summarized the recent progress and highlighted R&D innovations in PS-DAFC technology since 2018. The main developments targeted traditional PEM-based DMFCs; however, other alcohols and other oxidants, as well as AEM applications for both single cells and stacks, were also covered.

From this work, it is clear that new catalysts and membranes have played a key role in enhancing the performance of the devices, and they will be needed for future advances. However, the development of new materials is not the only issue to consider; researchers must also control the content and location of reactants and products when operating the devices. The ultimate goal is to support and facilitate the deployment of different configurations of PS-DAFCs into broad commercial markets. However, this is only achievable by translating the research discoveries into the scale-up and commercialization processes of the technology. The practical examples systematized and discussed in this review can provide guidance on how innovative increments in PS-DAFC systems can meet the energy needs to power small portable applications foreseen in the near future.

Author Contributions: Conceptualization, M.H.d.S.; resources, V.B.O. and A.M.F.R.P.; writing—original draft preparation, M.H.d.S.; writing—review and editing, M.H.d.S., V.B.O. and A.M.F.R.P.; supervision, V.B.O.; funding acquisition, V.B.O. All authors have read and agreed to the published version of the manuscript.

Funding: This work was financially supported by Project PTDC/NewPortCell-POCI-01-0145-FEDER-032116—funded by FEDER funds through COMPETE2020—Programa Operacional Competitividade e Internacionalização (POCI) and by national funds (PIDDAC) through FCT/MCTES. This work was financially supported by LA/P/0045/2020 (ALiCE), UIDB/00532/2020, and UIDP/00532/2020 (CEFT), funded by national funds through FCT/MCTES (PIDDAC).

Conflicts of Interest: The authors declare no conflict of interest. The funders had no role in the design of the study; in the collection, analyses, or interpretation of data; in the writing of the manuscript, or in the decision to publish the results.

Abbreviations

3D GF	Three-dimensional graphene frameworks
3DG	Three-dimensional graphene
AA	Alkaline–acid
ABS	Acrylonitrile butadiene styrene
ACL	Anode catalyst layer
ACR	Alcohol concentration ratio
ADL	Anode diffusion layer
AEMs	Anion-exchange membranes
AOR	Alcohol oxidation reaction
BPs	Bipolar plates

CB	Carbon black
CC	Carbon cloth
CCL	Cathode catalyst layer
CCs	Current collectors
CDL	Cathode diffusion layer
CFSF	Copper fiber sintered felt
CGCOB	Crude glycerol from cooking oil biodiesel
CGSOB	Crude glycerol from sunflower oil biodiesel
CH	Circular-hole array
CL	Catalyst layer
CNCs	Carbon nanocages
CNF	Carbon nanofiber
CNT-OH	Carboxylated multiwalled carbon nanotubes
CNTs	Carbon nanotubes
CNWs	Carbon nanofiber webs
CP	Carbon paper
CP	Circle pattern
CQDs	Carbon quantum dots
DAFCs	Direct alcohol fuel cells
DEFCs	Direct ethanol fuel cells
DEGHPFC	Direct ethylene glycol–hydrogen peroxide fuel cell
DFT	Density functional theory
DGHPFC	Direct glycerol–hydrogen peroxide fuel cell
DMFCs	Direct methanol fuel cells
DMHPFC	Direct methanol–hydrogen peroxide fuel cell
EEC	Equivalent electric circuit
EG	Ethylene glycol
EIS	Electrochemical impedance spectroscopy
EOR	Ethanol oxidation reaction
EtOH	Ethanol
G	Glycerol
GDL	Gas diffusion layer
GO	Graphene oxide
GOR	Glycerol oxidation reaction
GQDs	Graphene quantum dots
HLS	Hill-like structure
HPG	High-purity glycerol
HPOR	Hydrogen peroxide reduction reaction
HPRR	Hydrogen peroxide reduction reaction
HSP	Horizontal stripe pattern
KP	Karrapo
LE	Liquid electrolyte
MCDM	Multicriteria decision making
MEA	Membrane electrode assembly
MEMS	Microelectromechanical systems
MeOH	Methanol
MOC	Methanol crossover
MPC	Magnesia phosphate cement
MPL	Microporous layer
NiF	Nickel foam
NPs	Nanoparticles
NRGO	Nitrogen-doped reduced graphene oxide
OCV	Open-circuit voltage
ORR	Oxygen reduction reaction
PAN	Polyacrylonitrile
PB	Prussian Blue
PC	Polycarbonate

PCB	Printed circuit board
PD	Power density
PEG	Poly(ethylene glycol)
PEM	Polymer electrolyte membrane or proton exchange membrane
PEMFCs	Polymer electrolyte membrane fuel cells
PF	Parallel fence
PFr	Pore-former
PGM	Platinum group metal
PMG	Precious metal group
PMMA	Polymethylmethacrylate
PS-DAFCs	Passive small direct alcohol fuel cells
PS-DMFCs	Passive small direct methanol fuel cells
PSO	Particle swarm optimization
Pt	Platinum
PTFE	Polytetrafluoroethylene
rGO	reduced GO
RSM	Response surface methodology
RT	Room temperature
SAP	Super absorbent polymer
SCS	Silicone heating sheet
SDSS	Sodium dihexyl sulfosuccinate
SEM	Scanning electron microscopy
SPDG	Saponification process-derived glycerol
SS	Stainless steel
SSFF	Stainless-steel fiber felt
THS	Through-hole silicon
UAVs	Unmanned aerial vehicles
UAVs	Unmanned aerial vehicles
VGCNF	Vapor-grown carbon nanofiber
VSP	Vertical strip pattern
WML	Water management layer

References

1. IEA. World Energy Outlook 2019 Executive Summary, 2019. Available online: https://iea.blob.core.windows.net/assets/1f6bf453-3317-4799-ae7b-9cc6429c81d8/English-WEO-2019-ES.pdf (accessed on 3 January 2022).
2. FCH2JU. Hydrogen Roadmap Europe: A sustainable pathway for the European Energy Transition, 978-92-9246-332-8, 2019. Available online: https://www.fch.europa.eu/sites/default/files/Hydrogen%20Roadmap%20Europe_Report.pdf (accessed on 12 January 2022).
3. Krishan, O.; Suhag, S. An updated review of energy storage systems: Classification and applications in distributed generation power systems incorporating renewable energy resources. *Int. J. Energy Res.* **2019**, *43*, 6171–6210. [CrossRef]
4. Staffell, I.; Scamman, D.; Velazquez Abad, A.; Balcombe, P.; Dodds, P.E.; Ekins, P.; Shah, N.; Ward, K.R. The role of hydrogen and fuel cells in the global energy system. *Energy Environ. Sci.* **2019**, *12*, 463–491. [CrossRef]
5. Sazali, N.; Wan Salleh, W.N.; Jamaludin, A.S.; Mhd Razali, M.N. New Perspectives on Fuel Cell Technology: A Brief Review. *Membranes* **2020**, *10*, 99. [CrossRef] [PubMed]
6. Goor, M.; Menkin, S.; Peled, E. High power direct methanol fuel cell for mobility and portable applications. *Int. J. Hydrog. Energy* **2019**, *44*, 3138–3143. [CrossRef]
7. Mohammed, H.; Al-Othman, A.; Nancarrow, P.; Tawalbeh, M.; Assad, M.E.H. Direct hydrocarbon fuel cells: A promising technology for improving energy efficiency. *Energy* **2019**, *172*, 207–219. [CrossRef]
8. Bollella, P.; Lee, I.; Blaauw, D.; Katz, E. A Microelectronic Sensor Device Powered by a Small Implantable Biofuel Cell. *ChemPhysChem* **2020**, *21*, 120–128. [CrossRef]
9. Xiao, X.; Xia, H.-Q.; Wu, R.; Bai, L.; Yan, L.; Magner, E.; Cosnier, S.; Lojou, E.; Zhu, Z.; Liu, A. Tackling the Challenges of Enzymatic (Bio)Fuel. *Cells. Chem. Rev.* **2019**, *119*, 9509–9558. [CrossRef]
10. Sá, M.; Brandão, L. Non-enzymatic direct glucose fuel cells (DGFC): A novel principle towards autonomous electrochemical biosensors. *Int. J. Hydrogen Energy* **2019**, *45*, 29749–29762. [CrossRef]
11. Xu, Q.; Zhang, F.; Xu, L.; Leung, P.; Yang, C.; Li, H. The applications and prospect of fuel cells in medical field: A review. *Renew. Sustain. Energy Rev.* **2017**, *67*, 574–580. [CrossRef]
12. Da Silva, L.M.; Cesar, R.; Moreira, C.M.; Santos, J.H.; De Souza, L.G.; Pires, B.M.; Vicentini, R.; Nunes, W.; Zanin, H. Reviewing the fundamentals of supercapacitors and the difficulties involving the analysis of the electrochemical findings obtained for porous electrode materials. *Energy Storage Mater.* **2019**, *27*, 555–590. [CrossRef]

13. Shaari, N.; Kamarudin, S.K.; Bahru, R.; Osman, S.H.; Md Ishak, N.A.I. Progress and challenges: Review for direct liquid fuel cell. *Int. J. Energy Res.* **2021**, *45*, 6644–6688. [CrossRef]
14. Sharaf, O.Z.; Orhan, M.F. An overview of fuel cell technology: Fundamentals and applications. *Renew. Sustain. Energy Rev.* **2014**, *32*, 810–853. [CrossRef]
15. Alias, M.; Kamarudin, S.; Zainoodin, A.; Masdar, M. Active direct methanol fuel cell: An overview. *Int. J. Hydrogen Energy* **2020**, *45*, 19620–19641. [CrossRef]
16. Pinto, A.M.F.R.; Oliveira, V.B.; Falcão, D.S. *Direct Alcohol Fuel Cells for Portable Applications Fundamentals, Engineering and Advances*; Elsevier Science: Amsterdam, The Netherlands, 2018.
17. Falcão, D.; Silva, R.; Rangel, C.; Pinto, A. Performance of an Active Micro Direct Methanol Fuel Cell Using Reduced Catalyst Loading MEAs. *Energies* **2017**, *10*, 1683. [CrossRef]
18. Fadzillah, D.; Kamarudin, S.; Zainoodin, M.; Masdar, M. Critical challenges in the system development of direct alcohol fuel cells as portable power supplies: An overview. *Int. J. Hydrogen Energy* **2019**, *44*, 3031–3054. [CrossRef]
19. Xia, Z.; Zhang, X.; Sun, H.; Wang, S.; Sun, G. Recent advances in multi-scale design and construction of materials for direct methanol fuel cells. *Nano Energy* **2019**, *65*, 104048. [CrossRef]
20. Ong, B.; Kamarudin, S.; Basri, S. Direct liquid fuel cells: A review. *Int. J. Hydrogen Energy* **2017**, *42*, 10142–10157. [CrossRef]
21. Yahya, N.; Kamarudin, S.; Karim, N.; Masdar, M.S.; Loh, K.; Lim, K. Durability and performance of direct glycerol fuel cell with palladium-aurum/vapor grown carbon nanofiber support. *Energy Convers. Manag.* **2019**, *188*, 120–130. [CrossRef]
22. Azam, A.M.I.N.; Lee, S.H.; Masdar, M.S.; Zainoodin, A.M.; Kamarudin, S.K. Parametric study on direct ethanol fuel cell (DEFC) performance and fuel crossover. *Int. J. Hydrogen Energy* **2019**, *44*, 8566–8574. [CrossRef]
23. Yong, Y.; Azam, A.; Masdar, M.; Zainoodin, A.; Kamarudin, S. Anode structure with double-catalyst layers for improving the direct ethanol fuel cell performance. *Int. J. Hydrogen Energy* **2019**, *45*, 22302–22314. [CrossRef]
24. Shrivastava, N.K.; Chadge, R.B.; Ahire, P.; Giri, J.P. Experimental investigation of a passive direct ethanol fuel cell. *Ionics* **2019**, *25*, 719–726. [CrossRef]
25. Oliveira, V.; Pereira, J.; Pinto, A. Modeling of passive direct ethanol fuel cells. *Energy* **2017**, *133*, 652–665. [CrossRef]
26. An, L.; Zhao, T.; Li, Y. Carbon-neutral sustainable energy technology: Direct ethanol fuel cells. *Renew. Sustain. Energy Rev.* **2015**, *50*, 1462–1468. [CrossRef]
27. Kamarudin, M.Z.F.; Kamarudin, S.K.; Masdar, M.S.; Daud, W.R.W. Review: Direct ethanol fuel cells. *Int. J. Hydrog. Energy* **2013**, *38*, 9438–9453. [CrossRef]
28. de Sá, M.; Pinto, A.; Oliveira, V. Passive direct methanol fuel cells as a sustainable alternative to batteries in hearing aid devices–An overview. *Int. J. Hydrogen Energy* **2022**, *47*, 16552–16567. [CrossRef]
29. Carneiro, L.P.; Ferreira, N.S.; Tavares, A.P.; Pinto, A.M.; Mendes, A.; Sales, M.G.F. A passive direct methanol fuel cell as transducer of an electrochemical sensor, applied to the detection of carcinoembryonic antigen. *Biosens. Bioelectron.* **2020**, *175*, 112877. [CrossRef] [PubMed]
30. Larminie, J.; Dicks, A. *Fuel Cell Systems Explained*, 2nd ed.; John Wiley & Sons Ltd.: England, UK, 2003.
31. Zhao, T. *Micro Fuel Cells—Principles and Applications*; Elsevier Inc.: San Diego, CA, USA, 2009.
32. Kjeang, E.; Djilali, N.; Sinton, D. Chapter 3—Advances in Microfluidic Fuel Cells. In *Micro Fuel Cells, Principles and Applications*; Academic Press: Cambridge, MA, USA, 2009; pp. 99–139.
33. Falcão, D.; Oliveira, V.; Rangel, C.; Pinto, A. Review on micro-direct methanol fuel cells. *Renew. Sustain. Energy Rev.* **2014**, *34*, 58–70. [CrossRef]
34. Agnolucci, P. Economics and market prospects of portable fuel cells. *Int. J. Hydrogen Energy* **2007**, *32*, 4319–4328. [CrossRef]
35. Siwal, S.; Thakur, S.; Zhang, Q.; Thakur, V. Electrocatalysts for electrooxidation of direct alcohol fuel cell: Chemistry and applications. *Mater. Today Chem.* **2019**, *14*, 100182. [CrossRef]
36. Zheng, Y.; Wan, X.; Cheng, X.; Cheng, K.; Dai, Z.; Liu, Z. Advanced Catalytic Materials for Ethanol Oxidation in Direct Ethanol Fuel Cells. *Catalysts* **2020**, *10*, 166. [CrossRef]
37. Mansor, M.; Timmiati, S.N.; Lim, K.L.; Wong, W.Y.; Kamarudin, S.K.; Kamarudin, N.H.N. Recent progress of anode catalysts and their support materials for methanol electrooxidation reaction. *Int. J. Hydrogen Energy* **2019**, *44*, 14744–14769. [CrossRef]
38. Tong, Y.; Yan, X.; Liang, J.; Dou, S.X. Metal-Based Electrocatalysts for Methanol Electro-Oxidation: Progress, Opportunities, and Challenges. *Small* **2019**, *17*, e1904126. [CrossRef] [PubMed]
39. Zhao, X.; Liu, Q.; Li, Q.; Chen, L.; Mao, L.; Wang, H.; Chen, S. Two-dimensional electrocatalysts for alcohol oxidation: A critical review. *Chem. Eng. J.* **2020**, *400*, 125744. [CrossRef]
40. Wu, F.; Zhang, L.; Lai, J.; Luque, R.; Niu, W.; Xu, G. Modulating the oxophilic properties of inorganic nanomaterials for electrocatalysis of small carbonaceous molecules. *Nano Today* **2019**, *29*, 100802. [CrossRef]
41. Zhang, J.; Lu, S.; Xiang, Y.; Jiang, S.P. Intrinsic Effect of Carbon Supports on the Activity and Stability of Precious Metal Based Catalysts for Electrocatalytic Alcohol Oxidation in Fuel Cells: A Review. *ChemSusChem* **2020**, *13*, 2484–2502. [CrossRef]
42. Ren, X.; Lv, Q.; Liu, L.; Liu, B.; Wang, Y.; Liu, A.; Wu, G. Current progress of Pt and Pt-based electrocatalysts used for fuel cells. Sustain. *Energy Fuels* **2020**, *4*, 15–30. [CrossRef]
43. Hu, C.; Zhou, Y.; Xiao, M.; Yu, G. Precise size and dominant-facet control of ultra-small Pt nanoparticles for efficient ethylene glycol, methanol and ethanol oxidation electrocatalysts. *Int. J. Hydrogen Energy* **2020**, *45*, 4341–4354. [CrossRef]

44. Yao, D.; Zhang, W.; Ma, Q.; Xu, Q.; Pasupathi, S.; Su, H. Achieving high Pt utilization and superior performance of high temperature polymer electrolyte membrane fuel cell by employing low-Pt-content catalyst and microporous layer free electrode design. *J. Power Sources* **2019**, *426*, 124–133. [CrossRef]
45. Zhang, L.; Doyle-Davis, K.; Sun, X. Pt-Based electrocatalysts with high atom utilization efficiency: From nanostructures to single atoms. *Energy Environ. Sci.* **2019**, *12*, 492–517. [CrossRef]
46. Singh, K.; Tetteh, E.B.; Lee, H.-Y.; Kang, T.-H.; Yu, J.-S. Tailor-Made Pt Catalysts with Improved Oxygen Reduction Reaction Stability/Durability. *ACS Catal.* **2019**, *9*, 8622–8645. [CrossRef]
47. Ercolano, G.; Cavaliere, S.; Rozière, J.; Jones, D.J. Recent developments in electrocatalyst design thrifting noble metals in fuel cells. *Curr. Opin. Electrochem.* **2018**, *9*, 271–277. [CrossRef]
48. Du, L.; Prabhakaran, V.; Xie, X.; Park, S.; Wang, Y.; Shao, Y. Low-PGM and PGM-Free Catalysts for Proton Exchange Membrane Fuel Cells: Stability Challenges and Material Solutions. *Adv. Mater.* **2020**, *33*, 1908232. [CrossRef] [PubMed]
49. Kosmala, T.; Bibent, N.; Sougrati, M.T.; Dražić, G.; Agnoli, S.; Jaouen, F.; Granozzi, G. Stable, Active, and Methanol-Tolerant PGM-Free Surfaces in an Acidic Medium: Electron Tunneling at Play in Pt/FeNC Hybrid Catalysts for Direct Methanol Fuel Cell Cathodes. *ACS Catal.* **2020**, *10*, 7475–7485. [CrossRef]
50. Shi, Q.; He, Y.; Bai, X.; Wang, M.; Cullen, D.A.; Lucero, M.; Zhao, X.; More, K.L.; Zhou, H.; Feng, Z.; et al. Methanol tolerance of atomically dispersed single metal site catalysts: Mechanistic understanding and high-performance direct methanol fuel cells. *Energy Environ. Sci.* **2020**, *13*, 3544–3555. [CrossRef]
51. Baricci, A.; Bisello, A.; Serov, A.; Odgaard, M.; Atanassov, P.; Casalegno, A. Analysis of the effect of catalyst layer thickness on the performance and durability of platinum group metal-free catalysts for polymer electrolyte membrane fuel cells. *Sustain. Energy Fuels* **2019**, *3*, 3375–3386. [CrossRef]
52. Shao, Y.; Dodelet, J.; Wu, G.; Zelenay, P. PGM-Free Cathode Catalysts for PEM Fuel Cells: A Mini-Review on Stability Challenges. *Adv. Mater.* **2019**, *31*, e1807615. [CrossRef]
53. Xu, X.; Xia, Z.; Zhang, X.; Sun, R.; Sun, X.; Li, H.; Wu, C.; Wang, J.; Wang, S.; Sun, G. Atomically dispersed Fe-N-C derived from dual metal-organic frameworks as efficient oxygen reduction electrocatalysts in direct methanol fuel cells. *Appl. Catal. B Environ.* **2019**, *259*, 118042. [CrossRef]
54. Xia, Z.; Xu, X.; Zhang, X.; Li, H.; Wang, S.; Sun, G. Anodic engineering towards high-performance direct methanol fuel cells with non-precious-metal cathode catalysts. *J. Mater. Chem. A* **2020**, *8*, 1113–1119. [CrossRef]
55. Osmieri, L.; Pezzolato, L.; Specchia, S. Recent trends on the application of PGM-free catalysts at the cathode of anion exchange membrane fuel cells. *Curr. Opin. Electrochem.* **2018**, *9*, 240–256. [CrossRef]
56. Zhang, L.; Wilkinson, D.P.; Liu, Y.; Zhang, J. Progress in nanostructured (Fe or Co)/N/C non-noble metal electrocatalysts for fuel cell oxygen reduction reaction. *Electrochim. Acta* **2018**, *262*, 326–336. [CrossRef]
57. Vecchio, C.L.; Serov, A.; Romero, H.; Lubers, A.; Zulevi, B.; Aricò, A.; Baglio, V. Commercial platinum group metal-free cathodic electrocatalysts for highly performed direct methanol fuel cell applications. *J. Power Sources* **2019**, *437*, 226948. [CrossRef]
58. Abdelkareem, M.A.; Sayed, E.; Mohamed, H.O.; Obaid, M.; Rezk, H.; Chae, K.-J. Nonprecious anodic catalysts for low-molecular-hydrocarbon fuel cells: Theoretical consideration and current progress. *Prog. Energy Combust. Sci.* **2020**, *77*, 100805. [CrossRef]
59. de Sá, M.H.; Moreira, C.S.; Pinto, A.M.F.R.; Oliveira, V.B. Recent advances in nanocatalysts (NCs): Design development challenges for DMFC. *J. Energy Chem.* 2022; *Submitted*.
60. Sebastián, D.; Serov, A.; Matanovic, I.; Artyushkova, K.; Atanassov, P.; Arico', A.S.; Baglio, V. Insights on the extraordinary tolerance to alcohols of Fe-N-C cathode catalysts in highly performing direct alcohol fuel cells. *Nano Energy* **2017**, *34*, 195–204. [CrossRef]
61. Sebastián, D.; Serov, A.; Artyushkova, K.; Gordon, J.; Atanassov, P.; Aricò, A.S.; Baglio, V. High Performance and Cost-Effective Direct Methanol Fuel Cells: Fe-N-C Methanol-Tolerant Oxygen Reduction Reaction Catalysts. *ChemSusChem* **2016**, *9*, 1986–1995. [CrossRef]
62. Martinez, U.; Babu, S.K.; Holby, E.F.; Chung, H.T.; Yin, X.; Zelenay, P. Progress in the Development of Fe-Based PGM-Free Electrocatalysts for the Oxygen Reduction Reaction. *Adv. Mater.* **2019**, *31*, e1806545. [CrossRef]
63. Ehelebe, K.; Ashraf, T.; Hager, S.; Seeberger, D.; Thiele, S.; Cherevko, S. Fuel cell catalyst layer evaluation using a gas diffusion electrode half-cell: Oxygen reduction reaction on Fe-N-C in alkaline media. *Electrochem. Commun.* **2020**, *116*, 106761. [CrossRef]
64. Osmieri, L.; Escudero-Cid, R.; Armandi, M.; Videla, A.M.; Fierro, J.L.G.; Ocón, P.; Specchia, S. Fe-N/C catalysts for oxygen reduction reaction supported on different carbonaceous materials. Performance in acidic and alkaline direct alcohol fuel cells. *Appl. Catal. B Environ.* **2017**, *205*, 637–653. [CrossRef]
65. Osmieri, L.; Zafferoni, C.; Wang, L.; Videla, A.H.A.M.; Lavacchi, A.; Specchia, S. Polypyrrole-Derived Fe−Co−N−C Catalyst for the Oxygen Reduction Reaction: Performance in Alkaline Hydrogen and Ethanol Fuel Cells. *ChemElectroChem* **2018**, *5*, 1954–1965. [CrossRef]
66. Osmieri, L.; Escudero-Cid, R.; Videla, A.H.M.; Ocón, P.; Specchia, S. Application of a non-noble Fe-N-C catalyst for oxygen reduction reaction in an alkaline direct ethanol fuel cell. *Renew. Energy* **2018**, *115*, 226–237. [CrossRef]
67. Mustain, W.E.; Chatenet, M.; Page, M.; Kim, Y.S. Durability challenges of anion exchange membrane fuel cells. *Energy Environ. Sci.* **2020**, *13*, 2805–2838. [CrossRef]
68. Gottesfeld, S.; Dekel, D.R.; Page, M.; Bae, C.; Yan, Y.; Zelenay, P.; Kim, Y.S. Anion exchange membrane fuel cells: Current status and remaining challenges. *J. Power Sources* **2018**, *375*, 170–184. [CrossRef]

69. Krewer, U.; Weinzierl, C.; Ziv, N.; Dekel, D.R. Impact of carbonation processes in anion exchange membrane fuel cells. *Electrochim. Acta* **2018**, *263*, 433–446. [CrossRef]
70. Ziv, N.; Mustain, W.E.; Dekel, D.R. The Effect of Ambient Carbon Dioxide on Anion-Exchange Membrane Fuel Cells. *ChemSusChem* **2018**, *11*, 1136–1150. [CrossRef]
71. Mustain, W.E. Understanding how high-performance anion exchange membrane fuel cells were achieved: Component, interfacial, and cell-level factors. *Curr. Opin. Electrochem.* **2018**, *12*, 233–239. [CrossRef]
72. Pan, Z.; An, L.; Zhao, T.; Tang, Z. Advances and challenges in alkaline anion exchange membrane fuel cells. *Prog. Energy Combust. Sci.* **2018**, *66*, 141–175. [CrossRef]
73. Sarapuu, A.; Kibena-Põldsepp, E.; Borghei, M.; Tammeveski, K. Electrocatalysis of oxygen reduction on heteroatom-doped nanocarbons and transition metal–nitrogen–carbon catalysts for alkaline membrane fuel cells. *J. Mater. Chem. A* **2018**, *6*, 776–804. [CrossRef]
74. An, L.; Zhao, T. Transport phenomena in alkaline direct ethanol fuel cells for sustainable energy production. *J. Power Sources* **2017**, *341*, 199–211. [CrossRef]
75. Borghei, M.; Laocharoen, N.; Kibena-Põldsepp, E.; Johansson, L.-S.; Campbell, J.; Kauppinen, E.; Tammeveski, K.; Rojas, O.J. Porous N,P-doped carbon from coconut shells with high electrocatalytic activity for oxygen reduction: Alternative to Pt-C for alkaline fuel cells. *Appl. Catal. B Environ.* **2017**, *204*, 394–402. [CrossRef]
76. Kanninen, P.; Borghei, M.; Hakanpää, J.; Kauppinen, E.I.; Ruiz, V.; Kallio, T. Temperature dependent performance and catalyst layer properties of PtRu supported on modified few-walled carbon nanotubes for the alkaline direct ethanol fuel cell. *J. Electroanal. Chem.* **2017**, *793*, 48–57. [CrossRef]
77. Ozoemena, K.I. Nanostructured platinum-free electrocatalysts in alkaline direct alcohol fuel cells: Catalyst design, principles and applications. *RSC Adv.* **2016**, *6*, 89523–89550. [CrossRef]
78. Li, Y.; Zhao, T. A passive anion-exchange membrane direct ethanol fuel cell stack and its applications. *Int. J. Hydrogen Energy* **2016**, *41*, 20336–20342. [CrossRef]
79. Varcoe, J.R.; Atanassov, P.; Dekel, D.R.; Herring, A.M.; Hickner, M.A.; Kohl, P.A.; Kucernak, A.R.; Mustain, W.E.; Nijmeijer, K.; Scott, K.; et al. Anion-exchange membranes in electrochemical energy systems. *Energy Environ. Sci.* **2014**, *7*, 3135–3191. [CrossRef]
80. Ramaswamy, N.; Mukerjee, S. Alkaline Anion-Exchange Membrane Fuel Cells: Challenges in Electrocatalysis and Interfacial Charge Transfer. *Chem. Rev.* **2019**, *119*, 11945–11979. [CrossRef] [PubMed]
81. Zakaria, K.; McKay, M.J.; Thimmappa, R.; Hasan, M.; Mamlouk, M.; Scott, K. Direct Glycerol Fuel Cells: Comparison with Direct Methanol and Ethanol Fuel Cells. *ChemElectroChem* **2019**, *6*, 2578–2585. [CrossRef]
82. Yan, X.; Zhao, T.; An, L.; Zhao, G.; Shi, L. A direct methanol–hydrogen peroxide fuel cell with a Prussian Blue cathode. *Int. J. Hydrogen Energy* **2016**, *41*, 5135–5140. [CrossRef]
83. An, L.; Zhao, T.; Zeng, L.; Yan, X. Performance of an alkaline direct ethanol fuel cell with hydrogen peroxide as oxidant. *Int. J. Hydrogen Energy* **2014**, *39*, 2320–2324. [CrossRef]
84. Pan, Z.; An, L.; Wen, C. Recent advances in fuel cells based propulsion systems for unmanned aerial vehicles. *Appl. Energy* **2019**, *240*, 473–485. [CrossRef]
85. Wang, J.; Wang, H.; Fan, Y. Techno-Economic Challenges of Fuel Cell Commercialization. *Engineering* **2018**, *4*, 352–360. [CrossRef]
86. Wang, J. System integration, durability and reliability of fuel cells: Challenges and solutions. *Appl. Energy* **2017**, *189*, 460–479. [CrossRef]
87. Sgroi, M.F.; Zedde, F.; Barbera, O.; Stassi, A.; Sebastián, D.; Lufrano, F.; Baglio, V.; Aricò, A.S.; Bonde, J.L.; Schuster, M. Cost Analysis of Direct Methanol Fuel Cell Stacks for Mass Production. *Energies* **2016**, *9*, 1008. [CrossRef]
88. Dutta, K. *Direct Methanol Fuel Cell Technology*, 1st ed.; Elsevier: Amsterdam, The Netherlands, 2020; p. 564.
89. Yuda, A.; Ashok, A.; Kumar, A. A comprehensive and critical review on recent progress in anode catalyst for methanol oxidation reaction. *Catal. Rev.* **2020**, *64*, 126–228. [CrossRef]
90. Samimi, F.; Rahimpour, M.R. Chapter 14—Direct Methanol Fuel Cell. In *Methanol Science and Engineering*; Elsevier: Amsterdam, The Netherlands, 2018; pp. 381–397. [CrossRef]
91. Chen, X.; Li, T.; Shen, J.; Hu, Z. From structures, packaging to application: A system-level review for micro direct methanol fuel cell. *Renew. Sustain. Energy Rev.* **2017**, *80*, 669–678. [CrossRef]
92. Zhu, Y.; Gao, L.; Li, J. A Novel Button-Type Micro Direct Methanol Fuel Cell with Graphene Diffusion Layer. *Micromachines* **2019**, *10*, 658. [CrossRef]
93. Zhu, Y.; Zhang, X.; Li, J.; Qi, G. Three-dimensional graphene as gas diffusion layer for micro direct methanol fuel cell. *Int. J. Mod. Phys. B* **2018**, *32*, 1850145. [CrossRef]
94. Abdullah, F.A.; Kamarudin, S.K.; Zainoodina, A.M.; Masdar, M.S. Parametric Studies of Direct Methanol Fuel Cell under Different Modes of Operation. *J. Kejuruter.* **2020**, *32*, 159–164. [CrossRef]
95. Yuan, W.; Su, X.; Zhuang, Z.; Huang, S.; Wang, A.; Tang, Y. Forced under-rib water removal by using expanded metal mesh as flow fields for air-breathing direct methanol fuel cells. *Int. J. Hydrogen Energy* **2018**, *43*, 19711–19720. [CrossRef]
96. Wang, A.; Yuan, W.; Huang, S.; Tang, Y.; Chen, Y. Structural effects of expanded metal mesh used as a flow field for a passive direct methanol fuel cell. *Appl. Energy* **2017**, *208*, 184–194. [CrossRef]

97. Yuan, W.; Han, F.; Chen, Y.; Chen, W.; Hu, J.; Tang, Y. Enhanced Water Management and Fuel Efficiency of a Fully Passive Direct Methanol Fuel Cell with Super-Hydrophilic/-Hydrophobic Cathode Porous Flow-Field. *J. Electrochem. Energy Convers. Storage* **2018**, *15*, 031003. [CrossRef]
98. Hu, J.; Yuan, W.; Chen, W.; Xu, X.; Tang, Y. Fabrication and characterization of superhydrophobic copper fiber sintered felt with a 3D space network structure and their oil–water separation. *Appl. Surf. Sci.* **2016**, *389*, 1192–1201. [CrossRef]
99. Yuan, W.; Fang, G.; Li, Z.; Chen, Y.; Tang, Y. Using Electrospinning-Based Carbon Nanofiber Webs for Methanol Crossover Control in Passive Direct Methanol Fuel Cells. *Materials* **2018**, *11*, 71. [CrossRef] [PubMed]
100. Li, Y.; Zhang, X.; Yuan, W.; Zhang, Y.; Liu, X. A novel CO_2 gas removal design for a micro passive direct methanol fuel cell. *Energy* **2018**, *157*, 599–607. [CrossRef]
101. Wang, Y.; Liu, X.W.; Zhang, H.F.; Zhou, Z.P. Fabrication of self-healing super-hydrophobic surfaces on aluminium alloy substrates. *AIP Adv.* **2015**, *5*, 041314. [CrossRef]
102. Xue, R.; Zhang, Y.; Zhong, S.; Liu, X. A hydrophobic layer-based water feedback structure for passive μ-DMFC. *Microelectron. Eng.* **2018**, *190*, 57–62. [CrossRef]
103. Yuan, W.; Zhang, X.; Hou, C.; Zhang, Y.; Wang, H.; Liu, X. Enhanced water management via the optimization of cathode microporous layer using 3D graphene frameworks for direct methanol fuel cell. *J. Power Sources* **2020**, *451*, 227800. [CrossRef]
104. Deng, H.; Zhou, J.; Zhang, Y. A Trilaminar-Catalytic Layered MEA Structure for a Passive Micro-Direct Methanol Fuel Cell. *Micromachines* **2021**, *12*, 381. [CrossRef] [PubMed]
105. Braz, B.; Oliveira, V.; Pinto, A. Optimization of a passive direct methanol fuel cell with different current collector materials. *Energy* **2020**, *208*, 118394. [CrossRef]
106. Braz, B.; Moreira, C.; Oliveira, V.; Pinto, A. Effect of the current collector design on the performance of a passive direct methanol fuel cell. *Electrochim. Acta* **2019**, *300*, 306–315. [CrossRef]
107. Braz, B.; Oliveira, V.; Pinto, A. Experimental studies of the effect of cathode diffusion layer properties on a passive direct methanol fuel cell power output. *Int. J. Hydrogen Energy* **2019**, *44*, 19334–19343. [CrossRef]
108. Braz, B.A.; Oliveira, V.B.; Pinto, A.M.F.R. Experimental Evaluation of the Effect of the Anode Diffusion Layer Properties on the Performance of a Passive Direct Methanol Fuel Cell. *Energies* **2020**, *13*, 5198. [CrossRef]
109. Munjewar, S.S.; Thombre, S.B. Effect of current collector roughness on performance of passive direct methanol fuel cell. *Renew. Energy* **2019**, *138*, 272–283. [CrossRef]
110. Zuo, K.; Yuan, Z.; Cao, C.; Hao, Y. The mass transport based on convection effects in a passive DMFC under open-circuit conditions. *Int. J. Hydrogen Energy* **2018**, *43*, 23463–23474. [CrossRef]
111. Yuan, Z.; Zhang, M.; Zuo, K.; Ren, Y. The effect of gravity on inner transport and cell performance in passive micro direct methanol fuel cell. *Energy* **2018**, *150*, 28–37. [CrossRef]
112. Yuan, Z.; Zuo, K.; Cao, C.; Chen, S.; Chuai, W.; Guo, Z. The whole process, bubble dynamic analysis in two-phase transport of the passive miniature direct methanol fuel cells. *J. Power Sources* **2019**, *416*, 9–20. [CrossRef]
113. Yuan, Z.; Chuai, W.; Guo, Z.; Tu, Z.; Kong, F. The Self-Adaptive Fuel Supply Mechanism in Micro DMFC Based on the Microvalve. *Micromachines* **2019**, *10*, 353. [CrossRef]
114. Yuan, Z.; Chuai, W.; Guo, Z.; Tu, Z.; Kong, F. Investigation of self-adaptive thermal control design in passive direct methanol fuel cell. *Energy Storage* **2019**, *1*, 64. [CrossRef]
115. Yuan, Z.; Chuai, W.; Guo, Z.; Tu, Z.; Kong, F. Thermal Layout Analysis and Design of Direct Methanol Fuel Cells on PCB Based on Novel Particle Swarm Optimization. *Micromachines* **2019**, *10*, 641. [CrossRef]
116. Wang, L.; Yin, L.; Yang, W.; Cheng, Y.; Wen, F.; Liu, C.; Dong, L.; Wang, M. Evaluation of structural aspects and operation environments on the performance of passive micro direct methanol fuel cell. *Int. J. Hydrogen Energy* **2021**, *46*, 2594–2605. [CrossRef]
117. Wang, L.; Zhang, Y.; An, Z.; Huang, S.; Zhou, Z.; Liu, X. Non-isothermal modeling of a small passive direct methanol fuel cell in vertical operation with anode natural convection effect. *Energy* **2013**, *58*, 283–295. [CrossRef]
118. Rao, A.S.; Rashmi, K.R.; Manjunatha, D.V.; Jayarama, A.; Pinto, R. Enhancement of power output in passive micro-direct methanol fuel cells with optimized methanol concentration and trapezoidal flow channels—IOPscience. *J. Micromech. Microeng.* **2019**, *29*, 075006. [CrossRef]
119. Yang, C.-R.; Lu, C.-W.; Fu, P.-C.; Cheng, C.; Chiou, Y.-C.; Lee, R.-T.; Tseng, S.-F. Performance evaluation of μDMFCs based on porous-silicon electrodes and methanol modification. *Energy* **2020**, *192*, 116666. [CrossRef]
120. Abdelkareem, M.A.; Allagui, A.; Sayed, E.; Assad, M.E.H.; Said, Z.; Elsaid, K. Comparative analysis of liquid versus vapor-feed passive direct methanol fuel cells. *Renew. Energy* **2018**, *131*, 563–584. [CrossRef]
121. Abdelkareem, M.A.; Sayed, E.T.; Nakagawa, N. Significance of diffusion layers on the performance of liquid and vapor feed passive direct methanol fuel cells. *Energy* **2020**, *209*, 118492. [CrossRef]
122. Oliveira, V.; Pereira, J.; Pinto, A. Effect of anode diffusion layer (GDL) on the performance of a passive direct methanol fuel cell (DMFC). *Int. J. Hydrogen Energy* **2016**, *41*, 19455–19462. [CrossRef]
123. Nakajima, A. Design of hydrophobic surfaces for liquid droplet control. *NPG Asia Mater.* **2011**, *3*, 49–56. [CrossRef]
124. Zuo, K.; Yuan, Z. Design and experimental analysis of a dual-cavity high-concentration adaptive passive micro direct methanol fuel cell. *Int. J. Energy Res.* **2021**, *45*, 5359–5368. [CrossRef]

125. Lu, G.; Ning, F.; Wei, J.; Li, Y.; Bai, C.; Shen, Y.; Li, Y.; Zhou, X. All-solid-state passive direct methanol fuel cells with great orientation stability and high energy density based on solid methanol fuels. *J. Power Sources* **2020**, *450*, 227669. [CrossRef]
126. Boni, M.; Surapaneni, S.R.; Golagani, N.S.; Manupati, S.K. Experimental investigations on the effect of current collector open ratio on the performance of a passive direct methanol fuel cell with liquid electrolyte layer. *Chem. Pap.* **2021**, *75*, 27–38. [CrossRef]
127. Boni, M.; Rao, S.S.; Srinivasulu, G.N. Influence of intermediate liquid electrolyte layer on the performance of passive direct methanol fuel cell. *Int. J. Green Energy* **2019**, *16*, 1475–1484. [CrossRef]
128. Ramli, Z.A.C.; Kamarudin, S.K. Platinum-Based Catalysts on Various Carbon Supports and Conducting Polymers for Direct Methanol Fuel Cell Applications: A Review. *Nanoscale Res. Lett.* **2018**, *13*, 1–25. [CrossRef]
129. Ishak, N.; Kamarudin, S.; Timmiati, S.; Karim, N.; Basri, S. Biogenic platinum from agricultural wastes extract for improved methanol oxidation reaction in direct methanol fuel cell. *J. Adv. Res.* **2020**, *28*, 63–75. [CrossRef] [PubMed]
130. Shaari, N.; Kamarudin, S.K. Current status, opportunities, and challenges in fuel cell catalytic application of aerogels. *Int. J. Energy Res.* **2019**, *43*, 2447–2467. [CrossRef]
131. Shaari, N.; Kamarudin, S.K.; Bahru, R. Carbon and graphene quantum dots in fuel cell application: An overview. *Int. J. Energy Res.* **2021**, *45*, 1396–1424. [CrossRef]
132. Jeong, W.; Chang, I.; Ryu, S.; Zheng, C.; Cha, S.W.; Park, T. Cost-effective and durable Ru-sputtered Pt/C-based membrane–electrode assembly for passive direct methanol fuel cells. *AIP Adv.* **2019**, *9*, 095016. [CrossRef]
133. Jeong, W.; Cho, G.Y.; Cha, S.W.; Park, T. Surface Roughening of Electrolyte Membrane for Pt- and Ru-Sputtered Passive Direct Methanol Fuel Cells. *Materials* **2019**, *12*, 3969. [CrossRef]
134. Fard, H.F.; Khodaverdi, M.; Pourfayaz, F.; Ahmadi, M.H. Application of N-doped carbon nanotube-supported Pt-Ru as electrocatalyst layer in passive direct methanol fuel cell. *Int. J. Hydrogen Energy* **2020**, *45*, 25307–25316. [CrossRef]
135. Abdullah, N.; Kamarudin, S.K.; Shyuan, L.K. Novel Anodic Catalyst Support for Direct Methanol Fuel Cell: Characterizations and Single-Cell Performances. *Nanoscale Res. Lett.* **2018**, *13*, 1–13. [CrossRef]
136. Abdullah, N.; Kamarudin, S.; Shyuan, L.; Karim, N. Synthesis and optimization of PtRu/TiO2-CNF anodic catalyst for direct methanol fuel cell. *Int. J. Hydrogen Energy* **2019**, *44*, 30543–30552. [CrossRef]
137. Alias, M.; Kamarudin, S.; Zainoodin, A.; Masdar, M. Structural mechanism investigation on methanol crossover and stability of a passive direct methanol fuel cell performance via modified micro-porous layer. *Int. J. Energy Res.* **2021**, *45*, 12928–12943. [CrossRef]
138. Ramli, Z.A.C.; Kamarudin, S.K.; Basri, S.; Zainoodin, A.M. The potential of novel carbon nanocages as a carbon support for an enhanced methanol electro-oxidation reaction in a direct methanol fuel cell. *Int. J. Energy Res.* **2020**, *44*, 10071–10086. [CrossRef]
139. Golmohammadi, F.; Amiri, M. Fabrication of MEA from Biomass-Based Carbon Nanofibers Composited with Nickel-Cobalt Oxides as a New Electrocatalyst for Oxygen Reduction Reaction in Passive Direct Methanol Fuel Cells. *Electrocatalysis* **2020**, *11*, 485–496. [CrossRef]
140. Amiri, M.; Golmohammadi, F. Biomass derived hierarchical 3D graphene framework for high performance energy storage devices. *J. Electroanal. Chem.* **2019**, *849*, 113388. [CrossRef]
141. Farzaneh, A.; Goharshadi, E.K.; Gharibi, H.; Saghatoleslami, N.; Ahmadzadeh, H. Insights on the superior performance of nanostructured nitrogen-doped reduced graphene oxide in comparison with commercial Pt/C as cathode electrocatalyst layer of passive direct methanol fuel cell. *Electrochim. Acta* **2019**, *306*, 220–228. [CrossRef]
142. Farzaneh, A.; Saghatoleslami, N.; Goharshadi, E.K.; Gharibi, H.; Ahmadzadeh, H. 3-D mesoporous nitrogen-doped reduced graphene oxide as an efficient metal-free electrocatalyst for oxygen reduction reaction in alkaline fuel cells: Role of π and lone pair electrons. *Electrochim. Acta* **2016**, *222*, 608–618. [CrossRef]
143. Ismail, A.; Kamarudin, S.K.; Daud, W.R.W.; Masdar, S.; Hasran, U.A. Development of optimisation model for direct methanol fuel cells via cell integrated network. *Int. J. Hydrog. Energy* **2019**, *44*, 30606–30617. [CrossRef]
144. Fang, S.; Liu, Y.; Zhao, C.; Huang, L.; Zhong, Z.; Wang, Y. Polarization analysis of a micro direct methanol fuel cell stack based on Debye-Hückel ionic atmosphere theory. *Energy* **2021**, *222*, 119907. [CrossRef]
145. Abraham, B.G.; Chetty, R. Design and fabrication of a quick-fit architecture air breathing direct methanol fuel cell. *Int. J. Hydrogen Energy* **2021**, *46*, 6845–6856. [CrossRef]
146. Abraham, B.G.; Bhaskaran, R.; Chetty, R. Electrodeposited Bimetallic (PtPd, PtRu, PtSn) Catalysts on Titanium Support for Methanol Oxidation in Direct Methanol Fuel Cells. *J. Electrochem. Soc.* **2020**, *167*, 024512. [CrossRef]
147. Wang, L.; Yuan, Z.; Wen, F.; Cheng, Y.; Zhang, Y.; Wang, G. A bipolar passive DMFC stack for portable applications. *Energy* **2017**, *144*, 587–593. [CrossRef]
148. Hao, W.; Ma, H.; Sun, G.; Li, Z. Magnesia phosphate cement composite bipolar plates for passive type direct methanol fuel cells. *Energy* **2019**, *168*, 80–87. [CrossRef]
149. Hao, W.; Ma, H.; Lu, Z.; Sun, G.; Li, Z. Design of magnesium phosphate cement based composite for high performance bipolar plate of fuel cells. *RSC Adv.* **2016**, *6*, 56711–56720. [CrossRef]
150. Ma, H.; Xu, B. Potential to design magnesium potassium phosphate cement paste based on an optimal magnesia-to-phosphate ratio. *Mater. Des.* **2017**, *118*, 81–88. [CrossRef]
151. Raso, O.S.M.A.; Navarro, E.; Leo, T.J. Selection of thermoplastic polymers for use as bipolar plates in direct methanol fuel cell applications. *Mater. Des.* **2019**, *183*, 108148. [CrossRef]

152. Abdelkareem, M.A.; Elsaid, K.; Wilberforce, T.; Kamil, M.; Sayed, E.T.; Olabi, A. Environmental aspects of fuel cells: A review. *Sci. Total Environ.* **2021**, *752*, 141803. [CrossRef]
153. Elsaid, K.; Abdelfatah, S.; Elabsir, A.M.A.; Hassiba, R.J.; Ghouri, Z.K.; Vechot, L. Direct alcohol fuel cells: Assessment of the fuel's safety and health aspects. *Int. J. Hydrogen Energy* **2021**, *46*, 30658–30668. [CrossRef]
154. Pereira, J.; Falcão, D.; Oliveira, V.; Pinto, A. Performance of a passive direct ethanol fuel cell. *J. Power Sources* **2014**, *256*, 14–19. [CrossRef]
155. Fashedemi, O.O.; Mwonga, P.V.; Miller, H.A.; Maphanga, R.R.; Vizza, F.; Ozoemena, K.I. Performance of Pd@FeCo Catalyst in Anion Exchange Membrane Alcohol Fuel Cells. *Electrocatalysis* **2021**, *12*, 295–309. [CrossRef]
156. Fashedemi, O.O.; Julies, B.; Ozoemena, K.I. Synthesis of Pd-coated FeCo@Fe/C core–shell nanoparticles: Microwave-induced 'top-down' nanostructuring and decoration. *Chem. Commun.* **2013**, *49*, 2034–2036. [CrossRef]
157. Fashedemi, O.O.; Ozoemena, K.I. Enhanced methanol oxidation and oxygen reduction reactions on palladium-decorated FeCo@Fe/C core–shell nanocatalysts in alkaline medium. *Phys. Chem. Chem. Phys.* **2013**, *15*, 20982–20991. [CrossRef]
158. Fashedemi, O.O.; Ozoemena, K.I. Comparative electrocatalytic oxidation of ethanol, ethylene glycol and glycerol in alkaline medium at Pd-decorated FeCo@Fe/C core-shell nanocatalysts. *Electrochim. Acta* **2014**, *128*, 279–286. [CrossRef]
159. Fashedemi, O.O.; Miller, H.A.; Marchionni, A.; Vizza, F.; Ozoemena, K.I. Electro-oxidation of ethylene glycol and glycerol at palladium-decorated FeCo@Fe core–shell nanocatalysts for alkaline direct alcohol fuel cells: Functionalized MWCNT supports and impact on product selectivity. *J. Mater. Chem. A* **2015**, *3*, 7145–7156. [CrossRef]
160. Fuku, X.; Modibedi, M.; Matinise, N.; Mokoena, P.; Xaba, N.; Mathe, M. Single step synthesis of bio-inspired NiO/C as Pd support catalyst for dual application: Alkaline direct ethanol fuel cell and CO_2 electro-reduction. *J. Colloid Interface Sci.* **2019**, *545*, 138–152. [CrossRef] [PubMed]
161. Khalil, M.; Kadja, G.T.; Ilmi, M.M. Advanced nanomaterials for catalysis: Current progress in fine chemical synthesis, hydrocarbon processing, and renewable energy. *J. Ind. Eng. Chem.* **2020**, *93*, 78–100. [CrossRef]
162. Ekdharmasuit, P. Performance and Ethanol Crossover of Passive Direct Ethanol Fuel Cell Stack. *E3S Web Conf.* **2020**, *141*, 01008. [CrossRef]
163. Gojkovic, S.; Tripkovic, A.; Stevanovic, R. Mixtures of methanol and 2-propanol as a potential fuel for direct alcohol fuel cells. *J. Serbian Chem. Soc.* **2007**, *72*, 1419–1425. [CrossRef]
164. Munjewar, S.S.; Thombre, S.B.; Patil, A.P. Passive direct alcohol fuel cell using methanol and 2-propanol mixture as a fuel. *Ionics* **2019**, *25*, 2231–2241. [CrossRef]
165. Coutanceau, C.; Baranton, S.; Kouamé, R.S.B. Selective Electrooxidation of Glycerol into Value-Added Chemicals: A Short Overview. *Front. Chem.* **2019**, *7*, 100. [CrossRef]
166. Antolini, E. Glycerol Electro-Oxidation in Alkaline Media and Alkaline Direct Glycerol Fuel Cells. *Catalysts* **2019**, *9*, 980. [CrossRef]
167. Othman, P.N.A.M.; Karim, N.A.; Kamarudin, S.K. Research and innovation in the electrocatalyst development toward glycerol oxidation reaction. *Int. J. Energy Res.* **2021**, *45*, 12693–12727. [CrossRef]
168. Yahya, N.; Kamarudin, S.K.; Karim, N.A.; Basri, S.; Zanoodin, A.M. Nanostructured Pd-Based Electrocatalyst and Membrane Electrode Assembly Behavior in a Passive Direct Glycerol Fuel Cell. *Nanoscale Res. Lett.* **2019**, *14*, 1–17. [CrossRef]
169. Olivares-Ramírez, J.M.; Dector, A.; Bañuelos-Días, J.A.; Amaya-Cruz, D.M.; Ortiz-Verdín, A.; Jiménez-Sandoval, O.; Sabaté, N.; Esquivel, J.P. Evaluation of a Passive Anion-Exchange Membrane Micro Fuel Cell Using Glycerol from Several Sources. *Fuel Cells* **2019**, *19*, 10–18. [CrossRef]
170. Pan, Z.; Huang, B.; An, L. Performance of a hybrid direct ethylene glycol fuel cell. *Int. J. Energy Res.* **2019**, *43*, 2583–2591. [CrossRef]
171. Pan, Z.; Bi, Y.; An, L. A cost-effective and chemically stable electrode binder for alkaline-acid direct ethylene glycol fuel cells. *Appl. Energy* **2020**, *258*, 114060. [CrossRef]
172. Pan, Z.; Bi, Y.; An, L. Performance characteristics of a passive direct ethylene glycol fuel cell with hydrogen peroxide as oxidant. *Appl. Energy* **2019**, *250*, 846–854. [CrossRef]
173. Pan, Z.; Bi, Y.; An, L. Mathematical modeling of direct ethylene glycol fuel cells incorporating the effect of the competitive adsorption. *Appl. Therm. Eng.* **2019**, *147*, 1115–1124. [CrossRef]
174. Pan, Z.; Zhuang, H.; Bi, Y.; An, L. A direct ethylene glycol fuel cell stack as air-independent power sources for underwater and outer space applications. *J. Power Sources* **2019**, *437*, 226944. [CrossRef]
175. An, L.; Zhao, T.; Chai, Z.; Zeng, L.; Tan, P. Modeling of the mixed potential in hydrogen peroxide-based fuel cells. *Int. J. Hydrogen Energy* **2014**, *39*, 7407–7416. [CrossRef]
176. Kepenienė, V.; Stagniūnaitė, R.; Balčiūnaitė, A.; Tamašauskaitė-Tamašiūnaitė, L.; Norkus, E. Microwave-assisted synthesis of a AuCeO2/C catalyst and its application for the oxidation of alcohols in an alkaline medium. *New J. Chem.* **2020**, *44*, 18308–18318. [CrossRef]
177. Lu, B.; Yuan, W.; Su, X.; Zhuang, Z.; Ke, Y.; Tang, Y. Passive Direct Methanol–Hydrogen Peroxide Fuel Cell with Reduced Graphene Oxide–Supported Prussian Blue as Catalyst. *Energy Technol.* **2020**, *8*, 1901360. [CrossRef]